

Reconstruction of neuronal activity and connectivity patterns in the zebrafish olfactory bulb

Inauguraldissertation

zur

Erlangung der Würde eines Doktors der Philosophie

vorgelegt der

Philosophisch-Naturwissenschaftlichen Fakultät

der Universität Basel

von

Adrian A. Wanner

aus Buchrain, Schweiz

Basel, 2016

Originaldokument gespeichert auf dem Dokumentenserver der Universität Basel (edoc.unibas.ch)



Dieses Werk ist lizenziert unter einer Creative Commons Namensnennung 4.0 International Lizenz.

Genehmigt von der Philosophisch-Naturwissenschaftlichen Fakultät
auf Antrag von:

Prof. Dr. Rainer W. Friedrich
(Dissertationsleiter und Fakultätsverantwortlicher)

Prof. Dr. Richard Hahnloser
(Korreferent)

Basel, den 22.03.2016

Prof. Dr. Jörg Schibler
(Dekan der Philosophisch-
Naturwissenschaftlichen Fakultät)

The work presented in this thesis was carried out at the Friedrich Miescher Institute for Biomedical Research, Basel, Switzerland, under the supervision of Prof. Dr. Rainer W. Friedrich. All experiments, software development and data analysis of this work were performed by Adrian A. Wanner. The first part of Chapter 1 is partially based on (Wanner et al. 2015) and the second part of Chapter 1 is partially based on (Friedrich et al. 2013). Both review papers were written with participation of Adrian A. Wanner. Chapter 2 is based on a manuscript written by Adrian A. Wanner and Rainer W. Friedrich that has been published in Nature Neuroscience (Wanner et al. 2016). Chapter 3 is based on a manuscript written by Adrian A. Wanner that is currently in preparation.

*Die Entwicklung der Physik, die Entwicklung der Biologie,
das sind die Abenteuer, die es heute gibt.*

Friedrich Dürrenmatt im Gespräch mit Gerhard Vollmer,
Neuchâtel, October 1990

Acknowledgement

Rainer Friedrich, thank you very much for the great support throughout the past six years. It was a great pleasure to work under your guidance. This work would not have been possible without your optimism, creativity, scientific excellence and critical thinking.

Christel Genoud, I am very grateful for teaching me all the electron microscopy and sample preparation voodoo. Without your dedication, knowledge and support, the electron microscopy data presented in this work could not have been recorded. I would also like to thank Bill Anderson for excellent engineering support at all the occasions the microscope was not behaving well.

I would like to thank the whole Friedrich group for many very interesting discussions, critical input at lab meetings, entertaining lunch breaks and a very pleasant working atmosphere. In particular, I would like to thank Gilad Jaccobson for mentoring and many inspiring discussions on theoretical and computational neuroscience, statistics, politics, music and art. Many thanks to Peixin Zhu and Yan-Ping Zhang Schaerer for teaching me two-photon microscopy and to Iori Namekawa for sharing his experience in imaging of larval zebrafish and for the help with getting started with Python-programming. I am also grateful to Martin Nägeli, who helped me with sample preparation in the early phase of this project and who made sure, together with Estelle Arn, that the lab and fish facility was always clean, tidy, fully equipped and functional.

Many thanks to the FMI facility, in particular to Moritz Kirschmann, Aaron Ponti and Raphael Thierry from the imaging facility for their advice with image processing and to Dean Flanders, Stefan Grzybek, Risto Milani and Sjoerd Van Eeden for excellent IT-support.

I would also like to thank Lisa, Rose and Willie Ong for the help with hiring, training and managing the tracers in Hongkong. Not to forget the excellent tracing work done by Liao Xue Ping (廖雪平), Wang Xiao Mei (王晓梅), Deng Jian Ling (邓健灵), Hu Qiong Yue (胡琼月), Du Xuan Zhu (杜旋珠), Li Zhao Qiong (李兆琼), Ge Hai Yan (葛海燕), Huang Yan (黄艳), Chen Jian Qin (陈建勤), Chen Mei Fung (陈美凤), Cheung Mei Ming (张美明), Wang Jin Peng (王金鹏), Chen Zhi Min (陈植民), Zhuo Yuan Feng (卓远锋), Ma Ling (马玲), Chen Jia Ling (陈佳玲), Chen Kai Yin (陈凯茵), Chen Jie Yi (陈洁仪), Ge Xiao Long (葛小龙), Chen Jing Wen (陈静雯), Xian Ming Fang (洗明芳), Shen Yan Hong (沈燕红), Chen Min Zhuang (陈敏庄), Peng Tian Li (彭天丽), Yang Xiao Yuan (杨少娟), He Qing Qing (何清清), Xia Zhen (夏珍), Yan Ping (闫萍),

Zeng Wei Chan (曾维婵), Xu Bo (徐波), An Xiu Zhen (安秀真), hu Xiao Qian (胡小倩), Huang Xiao Peng (黄晓鹏) and Zheng Xiao Yan (郑小燕).

Last but not least, I would like to thank my family and friends for the great support and for keeping me grounded. Especially I would like to thank my parents for stimulating my interest in science from early childhood, for all encouragement, financial and emotional support and for helping me setting up ariadne-service gmbh. I would like to thank Eliane, my sister and editor of the probably most fantastic birthday gift ever, for her interest, support and many enduring discussions in various shades of gray.

I would like to thank Alexander Attinger, Marco Bieri, Nicole Birrer, Tanja Grossrieder, Alain Kamm, Markus Kunz, Frank Leonhardt, Philipp Odermatt, Emanuel Thaler and Lena Zumsteg for a lot of fun with hiking, skitouring, playing music and partying.

The last words of this acknowledgement belong to Barbara, the love of my life, who is always with me, supports me and gives me a home wherever we are.

Content

Abbreviations.....	10
Preface	11
Chapter 1 Introduction	13
1.1 Sparse versus dense sampling of neuronal connectivity and activity	13
1.2 Neuronal circuit reconstruction by volume electron microscopy	15
1.2.1 Volume electron microscopy techniques	15
1.2.2 Tissue preparation for 3D electron microscopy.....	16
1.2.3 Size limitations	17
1.2.4 Image analysis, annotation and segmentation.....	17
1.3 Sensory information processing in the olfactory bulb.....	19
1.3.1 Functional organization of the olfactory bulb	19
1.3.2 Neuronal computations in the olfactory bulb	21
1.4 Zebrafish as a model system in neuroscience: size matters.....	22
1.4.1 The olfactory system of zebrafish	24
1.5 Summary and thesis objectives	25
Chapter 2 Dense EM-based reconstruction of the interglomerular projectome in the zebrafish olfactory bulb.....	27
2.1 Abstract.....	27
2.2 Introduction	28
2.3 Results.....	29
2.3.1 Conductive embedding of tissue samples for SBEM.....	29
2.3.2 Neuron reconstruction.....	33
2.3.3 Identification and correction of reconstruction errors.....	34
2.3.4 Quantitative analysis of reconstruction errors	37
2.3.5 Completeness of neuron reconstruction and synapse annotation	38

2.3.6	The neuronal repertoire of the olfactory bulb.....	41
2.3.7	Neuronal organization of the olfactory bulb	45
2.4	Discussion.....	50
2.5	Methods.....	53
2.5.1	Reagents for EM.....	53
2.5.2	En bloc sample preparation for SBEM	53
2.5.3	SBEM	54
2.5.4	Image processing	55
2.5.5	Software: PyKNOSSOS.....	55
2.5.6	Tracing of neurons in the larval OB.....	56
2.5.7	Consolidation of skeletons.....	57
2.5.8	Synapse annotation	59
2.5.9	Morphological analysis	59
2.5.10	Acknowledgements.....	60
2.5.11	Author contributions.....	60
2.5.12	Competing financial interests	60
2.6	Supplementary Information.....	61
Chapter 3 Network topology supports pattern decorrelation in the olfactory bulb.....		74
3.1	Abstract.....	74
3.2	Introduction	75
3.3	Results.....	80
3.3.1	Probing IN and MC odor responses in the larval OB.....	80
3.3.2	Correlation and decorrelation of activity patterns	85
3.3.3	Transformation of odor information	86
3.4	Discussion.....	91
3.5	Materials and Methods.....	94

3.5.1	Animals and preparation.....	94
3.5.2	Odor stimulation	94
3.5.3	Multiphoton calcium imaging	95
3.5.4	Two-photon to EM correlation	96
3.5.5	Reconstruction of somatic firing rate changes	97
3.5.6	Population activity and correlation.....	98
3.5.7	Glomerular activity and structure to function relationship.....	98
Chapter 4	Discussion and outlook	101
References	104
Appendix A	Nature Neuroscience article on <i>Dense EM-based reconstruction of the interglomerular projectome in the zebrafish olfactory bulb</i>	117
Appendix B	PyKNOSSOS manual	131
Appendix C	Review article on <i>Challenges of microtome-based serial block-face scanning electron microscopy in neuroscience</i>	149
Appendix D	Review article on <i>Analyzing the structure and function of neuronal circuits in zebrafish</i>	156
Appendix E	Review article on <i>Functional development of the olfactory system in zebrafish</i>	165
Appendix F	Curriculum vitae.....	177

Abbreviations

AA	Amino acid
APN	Atypical projection neuron
ATUM	Automated tape-collecting ultra-microtome
BA	Bile acid
cOB	contra-lateral OB
dF/F	Percentage of change in raw fluorescence
dpf	days post fertilization
E3	Standard embryo medium
EM	Electron microscopy/ microscope
FIB-SEM	Focused-ion beam SEM
GABA	gamma-Aminobutyric acid
GC	Granule cell
GCA	Glycocholic acid
GCDCA	Glycochenodeoxycholic acid
IN	Interneuron
LOC	Large olfactory cell
lvSEM	low-voltage SEM
Lys	Lysine
MC	Mitral cell
NoS	No stimulus
OB	Olfactory bulb
OE	Olfactory epithelium
OR	Odorant receptor
OSN	Olfactory sensory neuron
PCA	Principal component analysis
PGC	Periglomerular cell
Phe	Phenylalanine
ROI	Region of interest
RT	Room temperature
SAC	Short-axon cell
SBEM	Serial block-face SEM
SEM	Scanning electron microscopy/ microscope
SNR	Signal to noise ratio
ssTEM	serial section TEM
TCA	Taurocholic acid
TCH	Thiocarbohydrazide
TDCA	Taurodeoxycholic acid
TDCaS	Temporally deconvolved calcium signal
Tel	Telencephalon
TEM	Transmission electron microscopy/ microscope
TEMCA	TEM with camera array imaging
Trp	Tryptophan
UA	Uranyl acetate
Val	Valine
vpSEM	variable pressure SEM
VR	Vomer nasal receptor

Preface

Ever since the early days of mankind, philosophers and scientists have been fascinated by the computational power and the functional variety of the brain. It is the brain that equips us with emotions, creativity, critical reasoning and abstract thinking. Consequently the brain determines our personality and to a large degree who we are. However, despite these obvious metaphysical aspects, the brain is a biophysical system and it should be possible to disentangle the underlying working principles using thorough scientific examination. At its core, we need to understand information flow and information processing in neuronal circuits in order to devise a mechanistic description of brain function. In particular we need to understand how neurons, the building blocks of neuronal circuits, are connected to each other and how they communicate.

Neuronal circuits typically consist of hundreds or thousands of interconnected neurons that communicate with each other via electrical and chemical signals. These signals are transmitted along axons and dendrites, cable-like processes that can extend up to several millimeters away from the cell's nucleus. At distinct sites, the processes of different neurons meet and form synaptic connections. Each neuronal circuit consists of various specialized neuron types, including broad classes of excitatory and inhibitory neurons. The biophysical properties, morphology and as well as the number, location and strengths of the synaptic connections of each neuron determines how information is integrated and how signals propagate in the network. Observing and measuring any of these properties and interactions in densely packed neuronal tissue poses extraordinary challenges to the experimenter, because it usually involves dense sampling in space and time. Measuring neuronal signals such as action potentials requires millisecond temporal resolution. Imaging of the complete dendritic and axonal arbor of even only a few neurons requires fields of view $> 100 \mu\text{m}$, while at the same time the unambiguous identification of synaptic connections requires isotropic spatial resolution of $< 20 \text{ nm}$.

Even for small neuronal circuits, the current technical limitations usually result in incomplete sampling and analysis both in space and time (Lichtman et al. 2011). This dissertation addresses several of these bottlenecks and describes new approaches to overcome many of these limitations. These new developments have been used successfully to combine *in vivo* two-photon calcium imaging with subsequent dense reconstruction of neuronal circuits from complete 3D electron microscopy stacks of the larval zebrafish olfactory bulb in the same specimen.

The first part of Chapter 1 explains why dense sampling of activity and connectivity is important for a mechanistic understanding of neuronal circuits. The second part gives an overview of current volume EM techniques suited for circuit reconstruction. The last two parts introduce circuit neuroscience with focus on circuit structure and function of the olfactory bulb of zebrafish.

Chapter 2 describes a new, improved toolbox for dense neuronal circuit reconstruction by serial block face electron microscopy. This toolbox was successfully used to reconstruct the entire olfactory bulb of the larval zebrafish and in particular revealed the inter-glomerular network organization at this early developmental stage. This chapter is based on a manuscript that has been published in Nature Neuroscience (Wanner et al. 2016).

Chapter 3 introduces a novel workflow for combining *in vivo* two-photon calcium imaging with subsequent dense circuit reconstruction from 3D EM stacks. We performed near exhaustive sampling of neuronal activity in the larval bulb and developed methods to map the activity patterns onto the reconstructed neurons. This revealed a fundamental structural substrate that supports the decorrelation of activity pattern elicited by similar odors in the larval OB. This chapter is based on a manuscript in preparation.

Chapter 4 summarizes the results of the foregoing chapters and discusses potential future directions, both experimentally but also in terms of analysis.

Chapter 1 Introduction

1.1 Sparse versus dense sampling of neuronal connectivity and activity

The idea of reconstructing neuronal circuits to understand information flow in the brain dates back to the seminal work of Santiago Felipe Ramón y Cajal (1852 - 1934) who inferred signal flow from neuronal morphology (Figure 1). To visualize neurons under a microscope, he used a silver staining technique developed by his colleague Camillo Golgi (1843 - 1926) that sparsely labels subsets of neurons in brain tissue. In the meantime, many new histological staining techniques have been developed to sparsely stain neurons and its sub-cellular structure including immuno-histological techniques and the expression of transgenic fluorescent markers (Bancroft et al. 2008). In parallel, new microscopy techniques have been developed that greatly facilitate the observation, visualization and reconstruction of neurons and their sub-cellular components, such as optical super-resolution microscopy (e.g., STED, PALM), multiphoton microscopy, electron microscopy and others (Helmchen et al. 2011).

Detailed observations of neurons by light microscopy usually require sparse labeling and therefore provide information only about a very small fraction of the neurons contained in a sample. However, neuronal tissue is densely packed. A cubic millimeter of mouse cortex contains about 9×10^4 neurons, 7×10^8 synapses and 4 km of neurites (Braitenberg et al. 1998). Repeated sparse sampling can provide first order statistical knowledge of circuit organization, such as the probability of connections between certain cell types, but higher-order statistical features or even a complete description of a circuit cannot be obtained. This is an important limitation particularly when the exact neuron-to-neuron connectivity matters for circuit function. Pair-wise connectivity can be studied using sparse sampling techniques such as multineuron patch-clamp recordings, forward optical probing, and trans-synaptic viral tracing (Luo et al. 2008, Wiechert et al. 2010, Perin et al. 2011), but higher order connectivity can only be analyzed by dense sampling. To date, electron microscopy (EM) is the only technique that provides sufficient resolution (<20 nm) to unambiguously identify each synapse and at the same time provides sufficiently large fields of view (>100 μm) to cover entire neuronal circuits in a piece of brain tissue.

Similar considerations apply to measurements of neuronal activity. Intra-cellular and single unit recordings have been used extensively to study the biophysical and electrophysiological properties of single neurons and neuronal compartments, and their responses to stimuli (Hodgkin et al. 1952, Hubel et al. 1962). However, in order to understand computation at the level of neuronal circuits it is necessary to record from more than one neuron simultaneously. With multi-electrode systems it is

possible to record action potentials from hundreds of units simultaneously with high temporal but limited spatial resolution (Bakkum et al. 2013). Moreover, high-density recordings are often difficult to achieve, particularly in the intact brain. An alternative, often less invasive approach is optical imaging, particularly multi-photon microscopy (Denk et al. 1990, Denk et al. 1997, Kerr et al. 2008), which has revolutionized the field of neuroscience. Together with voltage or calcium sensitive reporters it is now possible to record the activity of thousands of neurons simultaneously at high density (Deisseroth et al. 2013). New microscopy techniques such as light-sheet imaging made it possible to record even brain-wide activity of small transparent organisms (Keller et al. 2011, Ahrens et al. 2013). The most widely used reporters of neuronal activity are fluorescent calcium indicators. Synthetic and genetically encoded calcium-sensitive probes have improved both in terms of signal-to-noise (SNR) as well as in terms of temporal resolution and linearity (Akerboom et al. 2012, Knopfel 2012). Linearity is important because it permits to infer spike rates from calcium transients by deconvolution (Yaksi et al. 2006).

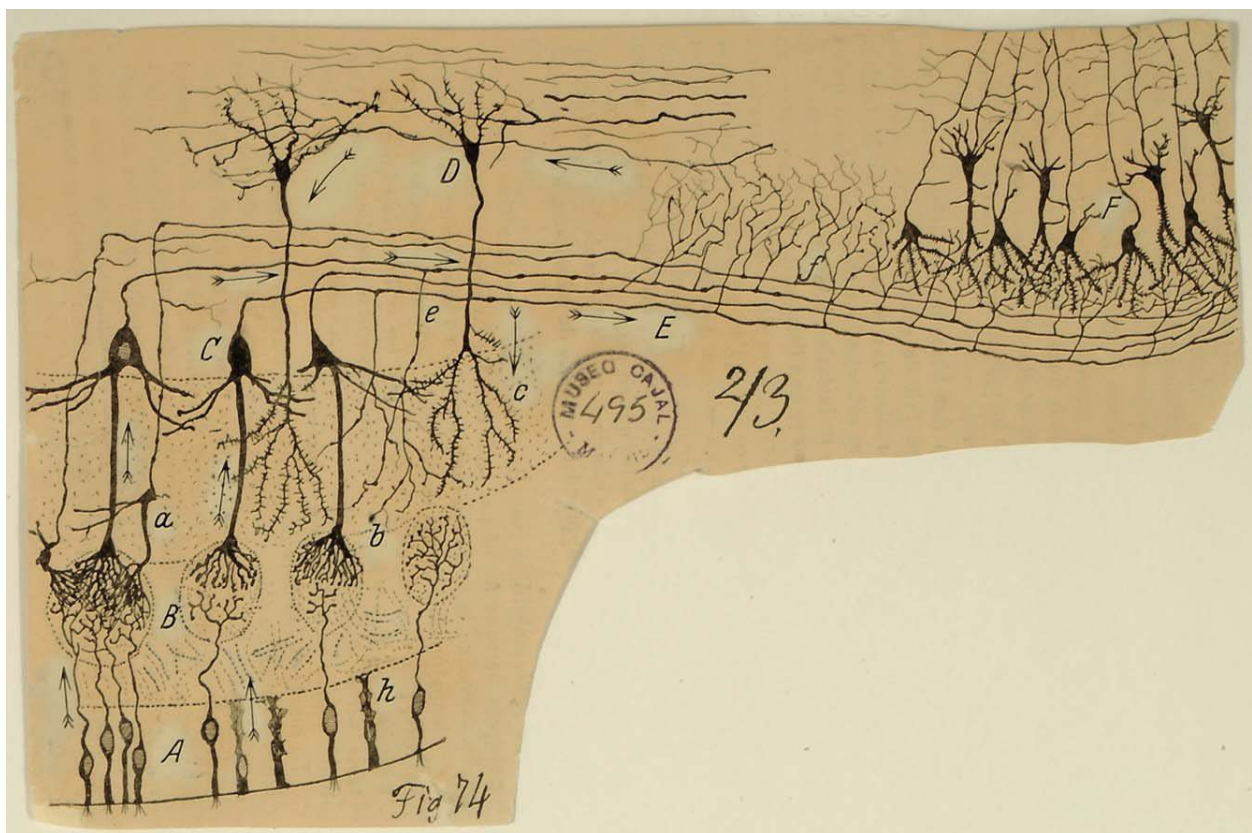


Figure 1 Drawing of neurons in the olfactory system from the olfactory epithelium to the olfactory cortex by Ramón y Cajal. (A) olfactory sensory neurons, (h) sustentacular cells in the olfactory epithelium; (B) glomeruli, (C) mitral cells, (a) tufted cells, (D) granule cells, (E) the lateral olfactory tract in the olfactory bulb; (F) the olfactory cortex. The arrows show the flow of information through the circuit according to Cajal, who inferred the direction of information flow from anatomical features of neurons. From the Cajal Legacy, Instituto Cajal, CSIC, Madrid, Spain.

1.2 Neuronal circuit reconstruction by volume electron microscopy

Volumetric EM is currently the only approach that provides sufficient resolution to resolve ultrastructural details such as synapses throughout a sufficiently large volume to allow for dense and complete reconstruction of neuronal circuits. Stacks of EM images covering a volume can be obtained by different techniques such as serial section transmission electron microscopy (ssTEM) (Harris et al. 2006), sectioning with an automated tape-collecting ultra-microtome (ATUM) (Hayworth et al. 2006), focused ion-beam scanning electron microscopy (FIB-SEM) (Knott et al. 2008) and microtome-based serial block-face scanning electron microscopy (SBEM) (Denk et al. 2004).

In the 1980s, ssTEM was used to map all 7000 synapses between the 302 neurons of the nematode *Caenorhabditis elegans* (White et al. 1986). This tremendous achievement involved about 10 years of painstaking manual neurite tracing and synapse annotation from EM micrographs. Still, this effort has not been matched since and it is to date the only complete connectome of an entire organism.

However, more recently partial connectomes have been obtained from the mouse retina by SBEM (Briggman et al. 2011, Helmstaedter et al. 2013), from mouse primary visual cortex using ssTEM with a custom CCD camera array (Bock et al. 2011) and from the *Drosophila* visual motion detection circuit using ssTEM (Takemura et al. 2013).

1.2.1 Volume electron microscopy techniques

ssTEM and ATUM use nondestructive manual (ssTEM) or automated (ATUM) ultrathin sectioning and slice collection with subsequent imaging, while SBEM and FIB-SEM use in situ destructive on-block sectioning inside the vacuum chamber of an SEM either by a diamond knife (SBEM) or with a focused ion beam (FIB-SEM) (Briggman et al. 2012). In ssTEM, sections are cut by hand using an ultra-microtome, collected onto grids and imaged in a TEM. Imaging approaches such as camera array imaging (TEMCA) with typically 2 - 4 nm lateral resolution can acquire images at a rate of 5 - 8 megapixels per second (Bock et al. 2011, Takemura et al. 2013). However, the manual sectioning process is labor-intensive and error-prone, limiting the number of consecutive sections typically to a few thousands. In addition, the typical section thickness is limited to 40 - 50 nm. Furthermore, the subsequent registration step is delicate due to distortions of sections occurring during cutting, handling and imaging (Kaynig et al. 2010, Saalfeld et al. 2010). ATUM-SEM overcomes these problems partially by automated cutting and collection of sections on an electrically opaque tape. This allows for reliable cutting of thousands of consecutive sections as thin as 30 nm. The on-tape sections are further processed for storage on silicon wafers and subsequent imaging in an SEM (Hayworth et al. 2014).

In SBEM, the recording chamber of a scanning electron microscope is equipped with an automated ultramicrotome. After each cut, the block-face is imaged with the scanning beam before the next section is shaved off. SBEM achieves fields of view of $>0.5 \times 0.5 \text{ mm}^2$ at a lateral resolution on the order of 6 - 10 nm. It allows for reliable cutting of thousands of sections from neural tissue with a thickness of 20 - 30 nm at an acquisition rate of 0.5 - 2 megapixels per second (Figure 2).

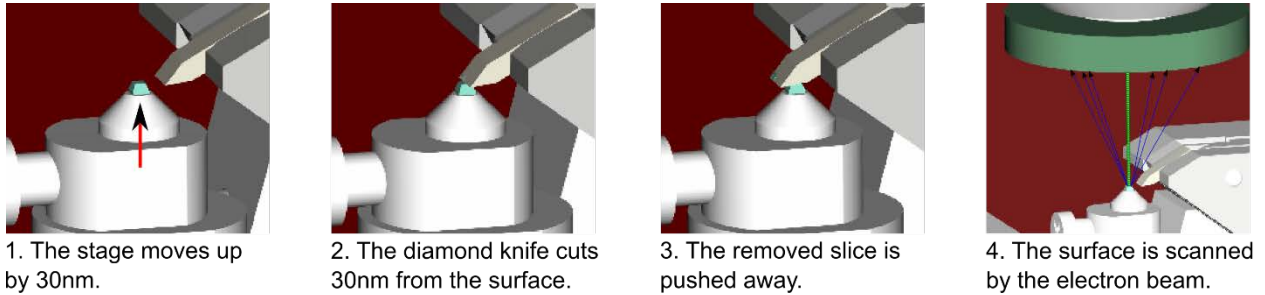


Figure 2 The working principle of serial block-face scanning electron microscopy Modified from Gatan Inc.

In FIB-SEM, slices are cut using a gallium-ion beam. This permits to cut sections as thin as 5 nm with a lateral resolution $<5 \text{ nm}$ and an acquisition rate of 0.1 - 0.5 megapixel per second (Boergens et al. 2013). However, the field of view is limited to $<0.1 \times 0.1 \text{ mm}^2$.

The major advantage of the destructive on-block methods is that they do not suffer from warping problems and section loss that can affect significantly the data quality and the subsequent data analysis. The advantages of the nondestructive methods are that sections can be imaged multiple times (e.g. at different magnifications) and in parallel on multiple microscopes, which can reduce the acquisition time significantly. Currently, these techniques are to a large degree complementary because they cover different ranges of resolution, fields of view and automation strategies (Lichtman et al. 2011).

1.2.2 Tissue preparation for 3D electron microscopy

In order to preserve and visualize the ultrastructure of biological tissue in electron microscopes, the tissue has to be processed by a series of chemical fixation, staining, dehydration and embedding steps. Chemical fixation immobilizes the macromolecules in the tissue by crosslinking proteins and lipids with aldehydes and osmium tetroxide, respectively. Electrons of an incident electron beam get scattered at electron dense material. This scattering process creates high energy back-scattered electrons and low-energy secondary electrons which are used in SEM to form an image. TEM, in contrast, detects the electrons that transmit the sample for image formation. In both methods, however, image contrast is generated by variations in electron-density in the sample. Therefore electron-dense heavy metals such

as osmium tetroxide and uranyl acetate are used to stain different parts of the tissue such as cell membranes, chromatin and synapses. In the final processing step, any remaining water is replaced by organic solvents such as ethanol and the sample is infiltrated with an epoxy resin. After polymerization of the epoxy resin, the sample resides in a hard epoxy block that allows stable, ultra-thin sectioning. Several staining protocols have recently been developed for volume EM to achieve various goals including the preservation of extracellular space and the ability to sustain the acceleration voltage and beam current necessary for high-speed acquisition while keeping signal-to-noise ratio sufficient for subsequent neuron reconstruction (Deerinck et al. 2010, Mikula et al. 2012, Tapia et al. 2012, Hua et al. 2015, Mikula et al. 2015, Pallotto et al. 2015).

1.2.3 Size limitations

The maximum size of volume EM datasets is usually limited by practical considerations, rather than by principal technical constraints. Consider, for example, the goal of acquiring an EM image stack covering one cubic millimeter, a benchmark that has not yet been achieved. For the dense reconstruction of all neurites and the unambiguous identification of chemical synapses in this volume, a voxel size of about $10 \times 10 \times 30$ nm is necessary. This volume corresponds to an image dataset requiring >300 TB of storage space. Due to lack of automation, neither FIB-SEM nor manual ssTEM could be used to acquire such a volume. ATUM-SEM can section such a volume but at the moment no automated imaging pipeline exists that can cope with the required number of sections (>30000). Using a commercially available SBEM with a typical acquisition speed of 1–4 $\mu\text{s}/\text{px}$ the acquisition of a cubic millimeter would take more than 18 years. However, due to the need for service, these commercial microscopes do usually not run continuously for more than 4-8 weeks. I therefore focused in this work on the acquisition of a complete larval zebrafish olfactory bulb (OB), whose volume ($120 \times 100 \times 70 \mu\text{m}^3$) is small enough to be acquired within 4-8 weeks using the commercial SBEM system (FEI Quanta 200 with Gatan 3View SBEM).

1.2.4 Image analysis, annotation and segmentation

Major challenges in the analysis of large volume EM datasets include viewing and annotating the massive image data sets. The large size of the image data makes it impossible to load the full data set for analysis into the RAM of even a powerful desktop computer. I therefore developed PyKNOSSOS, a Python-based software package designed for efficient visualization, tracing and labeling of large image datasets. Other software packages developed for similar purposes include KNOSSOS (Helmstaedter et al. 2011), TrakEM2 (Cardona et al. 2012) and CATMAID (Saalfeld et al. 2009). Like PyKNOSSOS, these programs use demand-driven dynamic data loading procedures, in which only the currently viewed

subvolume is loaded into memory. As the user browses through the data, the corresponding subvolumes are continuously loaded in the background for seamless navigation with minimal memory requirements. For very large datasets, CATMAID and KNOSSOS feature online streaming of the data from external servers. All programs feature a wide range of manual annotation tools, including feature labelling (e.g. mitochondria, synapses, etc.), skeleton tracing of neurites and volume segmentation. The manual annotation and segmentation of large image data sets is tedious, error-prone and can be very time-consuming. For example, the dense skeleton reconstruction and analysis of 950 neurons in the inner plexiform layer of a mouse retina required almost 30,000 human working hours (Perkel 2014), even though a skeletonization approach was used that achieved a 50-fold speed-up compared to volume contouring (Helmstaedter et al. 2011). The development of computer-assisted segmentation methods is underway but the reliability is not sufficient for fully automated analyses of volume EM data (Lowe 2004, Jain 2007, Chklovskii et al. 2010, Kaynig et al. 2010, Kim et al. 2014, Berning et al. 2015). Most previous and many ongoing project therefore rely mainly on manual tracing. Generally, multiple independent tracings of each neuron are required to identify errors, correct them, and form a consensus. Hence, the annotation and segmentation of EM data relies heavily on human input.

In a pioneering reconstruction project, hundreds of external helpers were recruited from local student populations for skeleton tracing of neurons using KNOSSOS (Helmstaedter et al. 2013). Other projects use CATMAID and distribute annotation tasks over multiple research groups (Saalfeld et al. 2009). Yet other projects recruited thousands of volunteers over the internet who were complemented by professional proof-readers (Kim et al. 2014), or used a small team of professional proofreaders (Takemura et al. 2013). About 20-40 hours of training are required for an untrained person to become familiar with the task of neuron tracing, and performance increases with further experience. Hence, training tracers requires a substantial initial investment. In the study of (Helmstaedter et al. 2013), tracers worked on average about 30 hours of work per month and about 90 hours in total. As a consequence the initial investment was not exploited with high efficiency. I therefore decided to implement a different approach and founded ariadne-service gmbh, a tracing company that trains and manages professional image annotators and organizes workflows. After the initial training, most of these annotators performed hundreds of annotation hours with high quality. Currently, the company maintains 30 annotators, most of them with more than 1000 hours of experience. This company allowed me to outsource stereotyped tracing work and now offers this service to the scientific community.

1.3 Sensory information processing in the olfactory bulb

Sensory systems such as the visual, auditory, somatosensory or the olfactory system inform the brain about its outside world and are well suited to study neuronal computation. Naturally, these systems have to deal with a continuous stream of a large amount of information. For example it has been estimated that a guinea pig retina transmits about 875 Kbits/s to its target in the thalamus, the lateral geniculate nucleus, which transmits information further to visual cortex (Koch et al. 2006). Sensory systems are commonly confronted with a high-dimensional stimulus space from which they have to extract relevant features and information on several levels of abstraction. This process requires computational procedures such as noise reduction, adaptation, equalization, scaling, decorrelation of input signals, dimensionality reduction, feature classification, pattern completion and others (Lewicki 2002, Friedrich et al. 2004, Sharpee et al. 2004, Yaksi et al. 2007, Niessing et al. 2010, Sharpee 2013, Zhu et al. 2013). Various forms of these types of computations have most likely evolved in parallel in different brain regions and sensory systems but it is still largely unknown how these computations are implemented in neural circuitry.

1.3.1 Functional organization of the olfactory bulb

The olfactory system is phylogenetically one of the oldest sensory systems, suggesting that functional principles are preserved across species. Odors are mainly detected by different G-protein coupled odorant receptors (ORs) on olfactory sensory neurons (OSNs) in the nose. While rodents have >1000 OR genes, humans have about 400 and zebrafish have only about 200-300 (Firestein 2001, Niimura 2009, Shi et al. 2009). Binding of odors to ORs activates second messenger cascades that ultimately generate action potentials. Axons of OSNs project to the olfactory bulb (OB) where they terminate in discrete neuropil structures, the glomeruli. Each glomerulus receives convergent input from OSNs expressing the same odorant receptor (Axel 1995, Buck 2000). Each OR can bind different chemicals and each odorant therefore activates a specific combination of ORs. Consequently, each odor elicits a specific activity pattern across the glomeruli (Friedrich et al. 1997). While the responses in the OB to odor stimulation are usually highly dynamic, prolonged odor stimulation induces partial adaptation of OSN responses. However, the relative activation levels of glomeruli remain almost unchanged during stimulus presentation.

Within glomeruli, OSNs make excitatory glutamatergic synapses onto mitral cells (MCs), the principal output neurons of the OB, and interneurons such as short axon cells (SACs) and periglomerular cells (PGCs) (Figure 3). MCs extend an apical dendrite into the glomerular layer that ramifies within one to a

few glomeruli. PGCs are a heterogeneous class of GABAergic interneurons that reside in the glomerular layer and interact with MCs and interneurons. Some PGC subtypes are monoglomerular while others can interact with neurons in multiple glomeruli within a restricted volume. SACs are usually larger than PGCs and innervate multiple glomeruli, including combinations of distant glomeruli. SACs are GABAergic, with a subpopulation being also dopaminergic (Bundschuh et al. 2012, Zhu et al. 2013). The largest subpopulation of neurons in the OB comprise the granule cells (GCs) located in the deep granule cell layer. In the adult OB, GCs outnumber MCs by a factor 10-200, depending on the species. They do not project into glomeruli but form synapses with dendrites of mitral cells mostly in a subglomerular, plexiform layer (Satou 1990). Synapses between GCs and MCs, but also between other interneurons and MCs, can be reciprocal (Pinching et al. 1971, Pinching et al. 1971, Satou 1990). Reciprocal synaptic connections are considered a hallmark of the OB and appear to be abundant but the exact degree of reciprocity has not been quantified. In addition to sensory input from the nose, the adult OB also receives massive top-down input from higher brain regions that terminates on interneurons, particularly granule cells.

The basic synaptic circuitry described above is largely conserved throughout all vertebrate classes including fish (Satou 1990, Taniguchi et al. 2014). In insects, the equivalent of the OB is thought to be the antennal lobe. As the OB, the antennal lobe features a glomerular organization with reciprocal synaptic connectivity and dynamic odor responses. Like MCs in the OB, projection neurons of the antennal lobe interact mainly via inhibitory pathways, mediated by various types of interneurons with different physiological properties and covering different spatial scales. However, there are much fewer interneurons and no prominent top-down projections in the antennal lobe.

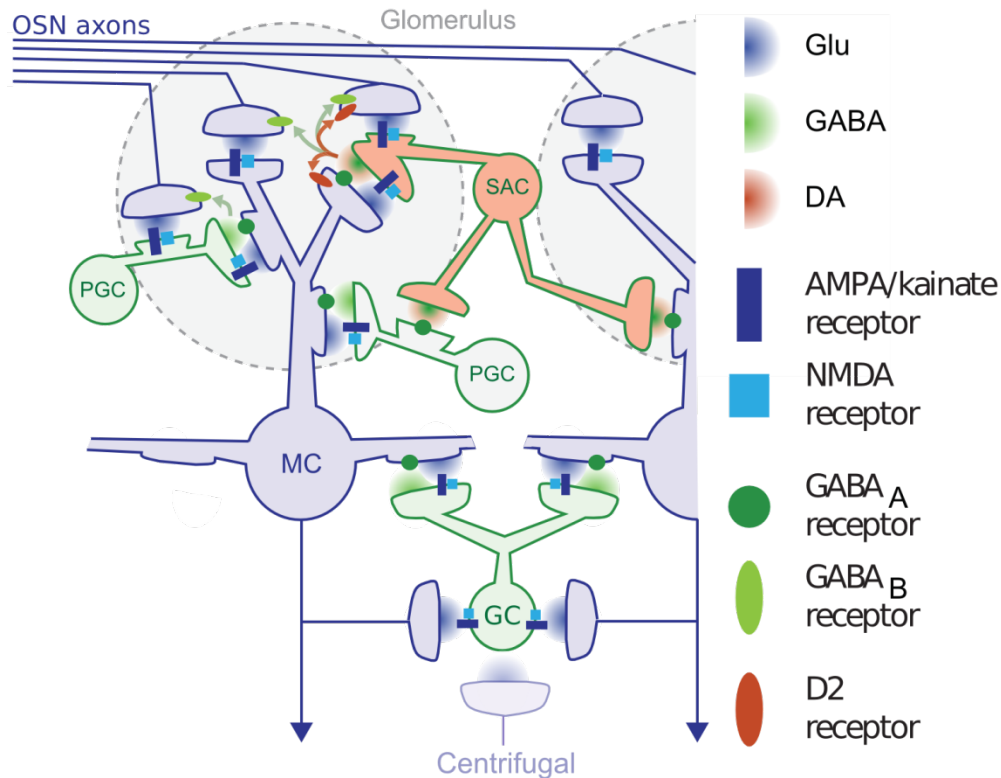


Figure 3 Simplified schematic of OB circuit. In the glomerular layer, olfactory sensor neurons (OSNs) form excitatory glutamatergic synapses onto mitral cells (MC), periglomerular cells (PGC) and short axon cells (SAC). PGCs and SACs receive excitatory glutamatergic input from MCs and provide GABAergic inhibition to MCs and neighboring PGCs and SACs. GABA spillover from PGCs can have an inhibitory effect onto OSN axon terminals. In the deeper granule cell layer, MC provide excitatory glutamatergic input onto granule cells (GC) by reciprocal dendro-dendritic synapses and axon collaterals. Centrifugal (mostly glutamatergic) inputs from higher brain areas onto GCs and other interneurons are not shown in detail (Figure modified from (Tabor et al. 2008)).

1.3.2 Neuronal computations in the olfactory bulb

Neuronal circuits in the OB perform multiple computations. One such computation is referred to as equalization, which is closely related to normalization (Carandini et al. 2012). Increasing the concentration of an odor results in (1) stronger activation of OSNs, and (2) activation of more OSNs. As a consequence, activity patterns across glomeruli change substantially with odor concentration (Friedrich et al. 1997). Equalization compensates for these effects and thereby stabilizes activity patterns across MCs against variations in odor concentration (Zhu et al. 2013). It is assumed that equalization helps to establish concentration-invariant odor representations that allow for the identification and discrimination of odors at different concentrations (Friedrich et al. 1997). Another computation related to normalization is contrast-enhancement, which increases the differences between strongly and weakly active neurons by boosting the former and attenuating the later (Cleland et al. 2006, Bundschuh et al. 2012). Attenuation of weakly active neurons can result in decorrelation of activity patterns that share

sets of weakly active neurons. However, boosting of strongly active neurons increases the correlation between activity patterns with common sets of strongly active neurons. Chemically similar odors usually activate overlapping sets of glomeruli, i.e. the input patterns to the OB are correlated. Often, input correlations are not favorable because, despite chemical similarity, odors can have different meaning, valence and importance. Therefore decorrelation of input patterns is an important computation in the OB (Yaksi et al. 2007, Niessing et al. 2010). In addition, pattern decorrelation can facilitate pattern discrimination and subsequent pattern storage, for example in auto-associative memory networks (Kohonen 1989, French 1999). Pattern decorrelation in the OB is a discrete process because odor representations change abruptly when odors the concentration ratio of components in binary mixtures are varied systematically (Niessing et al. 2010). Computational modeling and theoretical analyses revealed that pattern decorrelation can emerge from thresholding, a generic operation performed by spiking neurons, together with sparse recurrent connectivity (Wiechert et al. 2010). However, these theoretical studies assumed random connectivity between MCs and interneurons, which cannot explain abrupt transitions in odor representations. Abrupt transitions could arise from connectivity among specific ensembles of neurons, although other mechanisms are possible as well. Unless ensembles are highly stereotyped between individuals, connectivity among specific ensembles cannot be analyzed by sparse anatomical approaches. Hence, a dense reconstruction of the wiring diagram is required to test the hypothesis that pattern decorrelation is supported by specific connectivity in OB circuits.

1.4 Zebrafish as a model system in neuroscience: size matters

The zebrafish was first introduced as a model system for studying genetics and development (Streisinger et al. 1981), mainly because of its rapid development, small size and transparency at embryonic and larval stage, but also because of the relatively low maintenance costs. These are important advantages for systems neuroscience as well, but the field of zebrafish neurophysiology received an additional boost from the development of functional imaging and optogenetics techniques. The transparent early larval stage facilitates calcium imaging of neuronal activity patterns and optogenetic manipulations of neurons because no surgical procedures are required (O'Malley et al. 1996, Scott et al. 2009, Del Bene et al. 2012, Ahrens et al. 2013, Portugues et al. 2013). However, even more important is the small size of the larval zebrafish brain which permits exhaustive sampling of neuronal activity patterns by multiphoton calcium imaging and dramatically facilitates the reconstruction of wiring diagrams by 3D EM (Friedrich et al. 2013, Wanner et al. 2016).

The zebrafish brain is only about 0.5 mm thick and 1.5 mm long at early larval stages, and about 0.4 - 2 mm thick and 4.5 mm long in adults (Rupp et al. 1996). The total number of neurons is on the order of 10^5 in larvae and 10^7 in adults (Hill et al. 2003, Hinsch et al. 2007). The zebrafish OB contains only about 1000 neurons in the larva and 20000 - 30000 neurons in adults (Wiechert et al. 2010), while the OB of adult mice contains about 10^6 - 10^7 neurons. These size differences have dramatic consequences for the ability to reconstruct neuronal circuitry. Assuming that volumetric EM imaging is performed with a relatively high acquisition rate of 2 MHz, the resulting effective acquisition speed is 1.15 MHz, including overhead due to tiling of the field of view, stage movements and cutting. With a voxel size of $10 \times 10 \times 25 \text{ nm}^3$, this corresponds to an acquisition rate of $2.88 \mu\text{m}^3/\text{s}$. Consequently, it would take about 1200 days to acquire an adult zebrafish OB with a volume of about 0.3 mm^3 . However, to acquire a complete adult mouse OB with a volume of about 8 mm^3 (Pomeroy et al. 1990) it would take at least 88 years of continuous acquisition.

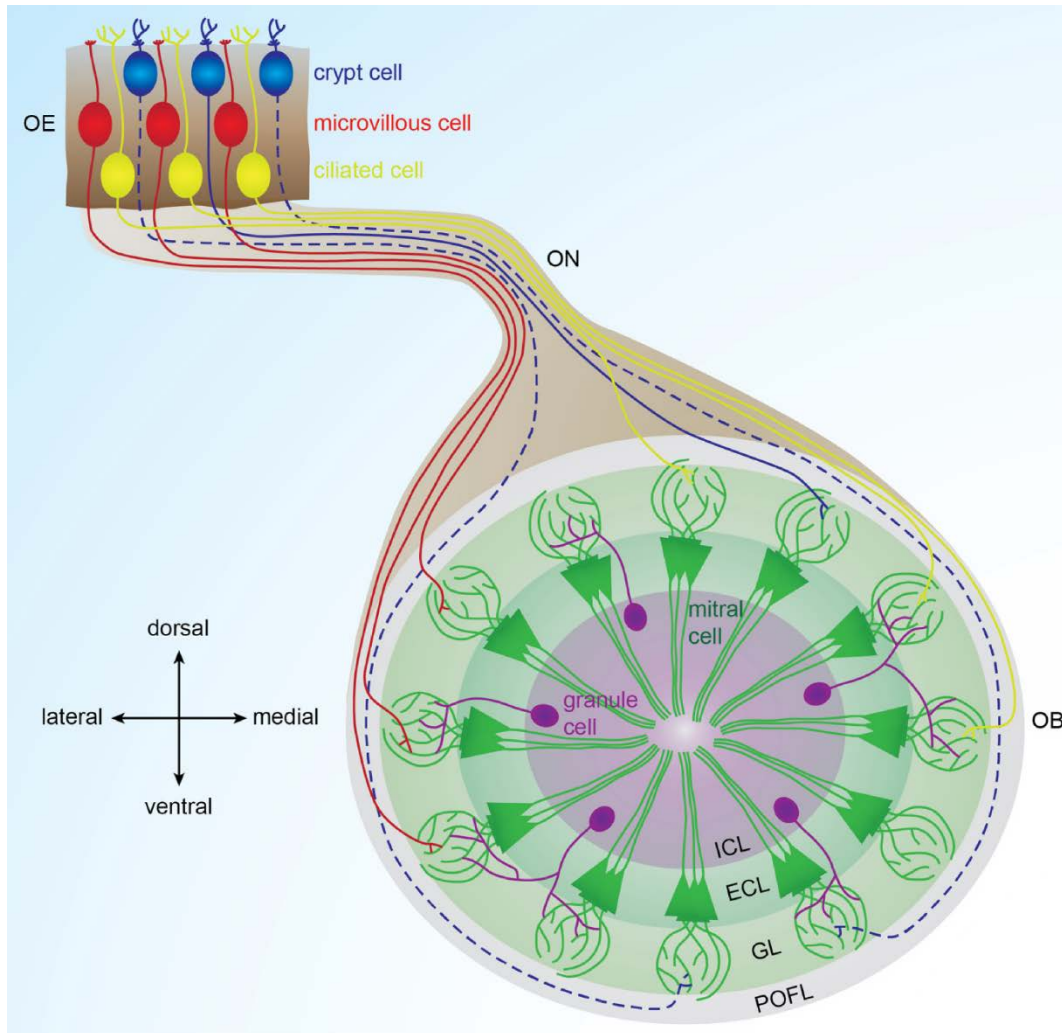


Figure 4 Organization of the zebrafish olfactory bulb. Odors are detected by three types of olfactory receptor neurons in the olfactory epithelium (OE) that project via the olfactory nerve (ON) into distinct glomeruli: Ciliated cells mainly project to the dorsal and medial OB, microvillous cells project to the lateral OB and crypt cells project to the dorsomedial OB. The adult zebrafish olfactory bulb is divided into four layers: POFL: primary olfactory fiber layer, GL: glomerular layer, ECL: external cell layer, ICL: internal cell layer. Solid lines represent connections described in zebrafish. Dotted lines represent connections described in other fish species. Adapted from (Kermen et al. 2013)

1.4.1 The olfactory system of zebrafish

The olfactory system of zebrafish is significantly smaller and has a less diverse OSN and glomerular repertoire than mammals (Korsching et al. 1997). The zebrafish genome contains 143 OR genes, 56 vomeronasal receptor (VR) genes, and 109 trace amine-associated receptor (TAAR) genes (Kermen et al. 2013), that are expressed by three different types of OSNs (Figure 4). Ciliated OSNs express ORs, respond to amino acids, bile acids and pheromones and project to the dorsal and medial OB (Sato et al. 2001, Hansen et al. 2003, Doving et al. 2009, Doving et al. 2011). Microvillous OSNs express VRs (Yoshihara 2009), respond mainly to amino acids and nucleotides (Lipschitz et al. 2002, Hansen et al.

2003) and innervate the lateral OB. Correspondingly, the lateral glomeruli respond to amino acid odors both in adult zebrafish (Friedrich et al. 1997, Friedrich et al. 1998, Fuss et al. 2001) as well as in larva (Li et al. 2005). The third OSN type, crypt cells, appears to be unique to fish (Hansen et al. 2000, Hansen et al. 2005). In zebrafish, crypt cells express a member of the VR family (Oka et al. 2012), are involved in detecting pheromones and project to the dorsomedial OB (Hamdani et al. 2007, Hamdani et al. 2008, Bazaes et al. 2012). Other subsets of zebrafish OSNs express members of the TAAR gene family (Hussain et al. 2009).

The adult zebrafish olfactory bulb comprises about 20000 - 30000 neurons (Wiechert et al. 2010) organized in four concentric layers (Figure 4). From superficial to deep, these are:

1. the primary olfactory fiber layer, formed by olfactory sensory neuron axons (Sato et al. 2007);
2. the glomerular layer, containing approximately 140 glomeruli, numerous smaller glomerular units, and somata of mitral cells, ruffed cells, PGCs and SACs (Braubach et al. 2012)
3. the external cell layer, consisting mainly of neuropil but also containing some somata (Fuller et al. 2005, Fuller et al. 2006);
4. the internal cell layer, containing cell bodies of different INs, predominantly GCs (Edwards et al. 2002, Bundschuh et al. 2012, Zhu et al. 2013).

Glutamatergic MC and ruffed cells are the principal neurons of the olfactory bulb in fish. Apical dendrites of mitral cells receive direct synaptic inputs from olfactory sensory neurons in glomeruli and project to the telencephalon and diencephalon (Fuller et al. 2006, Miyasaka et al. 2009). In the adult zebrafish, the IN : MC ratio is about 15 : 1 (Wiechert et al. 2010) whereas in the larval zebrafish we found an IN : MC ratio of 1 : 3 (Wanner et al. 2016). While the number of glomeruli in larval zebrafish is substantially lower than in adults (14-17 in 4-5 days old larvae), the coarse chemotopic map is already present (Li et al. 2005).

1.5 Summary and thesis objectives

By directly linking circuit structure to function, dense reconstruction of activity and connectivity patterns in neuronal circuits of the same specimen has the potential to unravel fundamental mechanistic principles of neuronal computation. *In vivo* multiphoton calcium imaging is the method of choice for observing population-wide neuronal activity at a spatial resolution sufficient to resolve individual neurons. Furthermore it has sufficient temporal resolution for following neuronal computations such as pattern decorrelation with a time course of a few hundreds of milliseconds. Only 3D electron

microscopy techniques such as serial block-face scanning electron microscopy (SBEM) permit the acquisition of fields of view large enough to cover entire neuronal microcircuits with a spatial resolution sufficient to unambiguously identify and reconstruct individual neuronal processes and synapses. Combining these two techniques for dense reconstruction of activity and connectivity is a major challenge even for small sample volumes such as the larval olfactory bulb of zebrafish.

The goal of this thesis was to move this endeavor into the realm of the feasible. First, I implemented a pipeline for ultra-resolution, high contrast SBEM in zebrafish by developing a novel conductive staining and embedding procedure for SBEM that improved the signal-to-noise power ratio of the relevant ultra-structural features by an order of magnitude and increased the acquisition speed by at least a factor 10 (Section 2.3.1). Second, I set up a high-throughput reconstruction and annotation pipeline (Section 2.3.2) that was used for dense reconstruction of all neurons in the larval OB (Section 2.3.5). From this I established a complete library of all MCs and INs, including rare cell types (Section 2.3.6) and analyzed the inter-glomerular connectivity (Section 2.3.7). In addition, I developed PyKNOSSOS, a software tool for efficient visualization, annotation and skeleton tracing of neurons and synapses in terabyte-sized image datasets (Section 2.5.5). In order to investigate if pattern decorrelation can already be found in the developing OB, I measured activity patterns in the larval OB upon odor stimulation (Section 3.3.1). The same specimen was subsequently used for dense SBEM reconstruction. In order to map activity onto connectivity, I developed a workflow for light microscopy to EM correlation (Section 3.5.4). Finally, I used the correlated imaging data and the reconstructed neurons to analyze the structure to function relationship in the larval OB. I found that activity patterns elicited by similar odors are decorrelated in the OB already at larval stage and I discovered a fundamental structure to function relationship that might serve, at least in parts, as a topological substrate for decorrelation in the OB (Section 3.3.2 - 3.3.3).

Chapter 2 Dense EM-based reconstruction of the interglomerular projectome in the zebrafish olfactory bulb

This chapter is based on a manuscript that has been published in Nature Neuroscience (Wanner et al. 2016), which can be found in Appendix A. The text and figures of this chapter corresponds largely to the submitted version of the manuscript, with minor formatting modifications in order to maintain coherent formatting in the presented work. Figures have been renumbered to maintain consistent numbering of figures across chapters in this work. Figure 7 and Figure 12 have been rearranged without changing content for more aesthetical page-filling. References from all chapters including this manuscript are collectively listed after Chapter 4. The PyKNOSSOS manual has been moved from Supplementary Methods (see section 2.6) to Appendix B.

Adrian A. Wanner^{1,2}, Christel Genoud¹, Tafheem Masudi^{1,2}, Léa Siksou¹, Rainer W. Friedrich^{1,2*}

¹ Friedrich Miescher Institute for Biomedical Research
Maulbeerstrasse 66
4058 Basel
Switzerland

² University of Basel
4003 Basel
Switzerland

* Correspondence:
Dr. Rainer Friedrich
Phone: +41 61 697 8614
Email: Rainer.Friedrich@fmi.ch

2.1 Abstract

The dense reconstruction of neuronal circuits from volumetric electron microscopy data has the potential to uncover fundamental structure-function relationships in the brain. To address bottlenecks in the workflow of this emerging methodology we developed a procedure for conductive sample embedding and a pipeline for neuron reconstruction. We reconstructed ~98 % of all neurons in the olfactory bulb of a zebrafish larva with high accuracy and annotated synapses of different neuron types. The organization of the larval olfactory bulb showed marked differences to the adult but similarities to the insect antennal lobe. Interneurons comprised multiple types but granule cells were rare, indicating that different sub-circuits develop sequentially. Inter-glomerular projections of interneurons were complex and bidirectional. Projections were not random but biased towards glomerular groups receiving input from common types of sensory neurons. Hence, the interneuron network in the olfactory bulb exhibits a topological organization that is governed by glomerular identity.

2.2 Introduction

Imaging methods for dense reconstructions of neuronal circuits need to provide nanometer resolution throughout large volumes which can be achieved by volumetric electron microscopy (EM) approaches (Lichtman et al. 2011, Denk et al. 2012) based on automated sectioning (Denk et al. 2004, Hayworth et al. 2006, Briggman et al. 2012, Hayworth et al. 2014). However, EM-based circuit reconstruction remains a major challenge because the full potential of the imaging methods has not yet been exploited and because the reconstruction of neurons and synapses from EM data requires enormous efforts (Denk et al. 2012, Helmstaedter 2013).

Volumetric EM data can be obtained by serial block-face EM (SBEM), a technique that automatically sections a sample inside a scanning electron microscope (SEM) and images the block face (Denk et al. 2004). SBEM can provide large fields of view ($>1 \text{ mm}^2$), thin sectioning ($<30 \text{ nm}$), and excellent image registration (Denk et al. 2012). However, sample charging or related interactions of the electron beam with the sample can reduce contrast, distort images and complicate thin sectioning (Robinson 1975, Mathieu 1999, Denk et al. 2004, Egerton et al. 2004, Titze et al. 2013). As a consequence, it is often necessary to use low vacuum and suboptimal imaging parameters which severely limits the potential of SBEM.

In order to reconstruct wiring diagrams of neuronal circuits from stacks of EM images it is necessary to trace individual neurons and identify their synaptic contacts. Considering that a cubic millimeter of cortical tissue contains $\sim 4.5 \text{ km}$ of neurites (Braitenberg et al. 1998), even small circuits present enormous challenges (White et al. 1986, Helmstaedter et al. 2013, Kim et al. 2014). Reconstruction accuracy has to be high because local reconstruction errors can have catastrophic effects on the wiring diagram. These demands cannot be fulfilled by automated approaches alone but require substantial human input for neuron tracing and error correction (White et al. 1986, Helmstaedter et al. 2011, Varshney et al. 2011, Helmstaedter et al. 2013, Takemura et al. 2013, Kim et al. 2014). To resolve this problem, large numbers of tracers have been recruited from local student populations or through the internet (Helmstaedter et al. 2011, Helmstaedter 2013, Helmstaedter et al. 2013, Kim et al. 2014) but the management of tracers can become rate-limiting even for circuits of moderate size. Hence, the scientific community would benefit from an infrastructure that provides circuit reconstruction as a service.

Precise analyses of circuit structure are important to understand the function of the olfactory bulb (OB) where connectivity cannot be predicted by topographic relationships (Fantana et al. 2008). The

organization of the OB is governed by discrete glomeruli, each of which receives input from sensory neurons expressing a defined odorant receptor (Axel 1995). Odor-evoked patterns of sensory input across these glomeruli are processed by principal neurons, the mitral/tufted cells (MCs), that interact via different types of interneurons (INs) (Wilson et al. 2006). The organization of these networks is, however, poorly understood. For example, it remains unclear whether inter-glomerular projections of interneurons are random, or whether these projections establish specific interactions between defined subsets of glomeruli. Insights into these questions are important to unravel the circuit mechanisms underlying olfactory computations such as the equalization and decorrelation of odor-evoked activity patterns (Wilson et al. 2006, Friedrich 2013).

We developed a method for conductive embedding of tissue samples that greatly reduces charging effects and thereby improves SBEM. In addition, we created ergonomic software for neuron tracing, visualization and synapse annotation, we developed new strategies to correct and quantify tracing errors, and we established a professional service to outsource stereotyped tasks. Using this toolbox we reconstructed >1,000 neurons in the OB of a zebrafish larva (~98 %) and found that the organization of the larval OB exhibits similarities to the insect antennal lobe. Moreover, we found that defined groups of glomeruli share specific patterns of IN innervation, demonstrating that inter-glomerular connectivity is organized by glomerular identity.

2.3 Results

2.3.1 Conductive embedding of tissue samples for SBEM

Because samples for SBEM are usually not conductive, scanning the block face with an electron beam leads to the accumulation of surface charges that cause multiple adverse effects including image distortions and irregular signal amplitude (Robinson 1975, Mathieu 1999, Titze et al. 2013). In principle, charging can be prevented by coating the sample with a thin metal film (Titze et al. 2013). However, this approach is demanding because the block face needs to be re-coated inside the vacuum chamber before each image. Most studies have therefore used low vacuum (10 – 50 Pa) to combat charging, which requires a variable-pressure SEM (vpSEM). Under these conditions, collisions of electrons with the gas generate ions that can neutralize surface charges but the scattering process severely compromises image quality (Robinson 1975, Mathieu 1999, Titze et al. 2013) (Figure 5a). We therefore explored alternative procedures to alleviate charging effects.

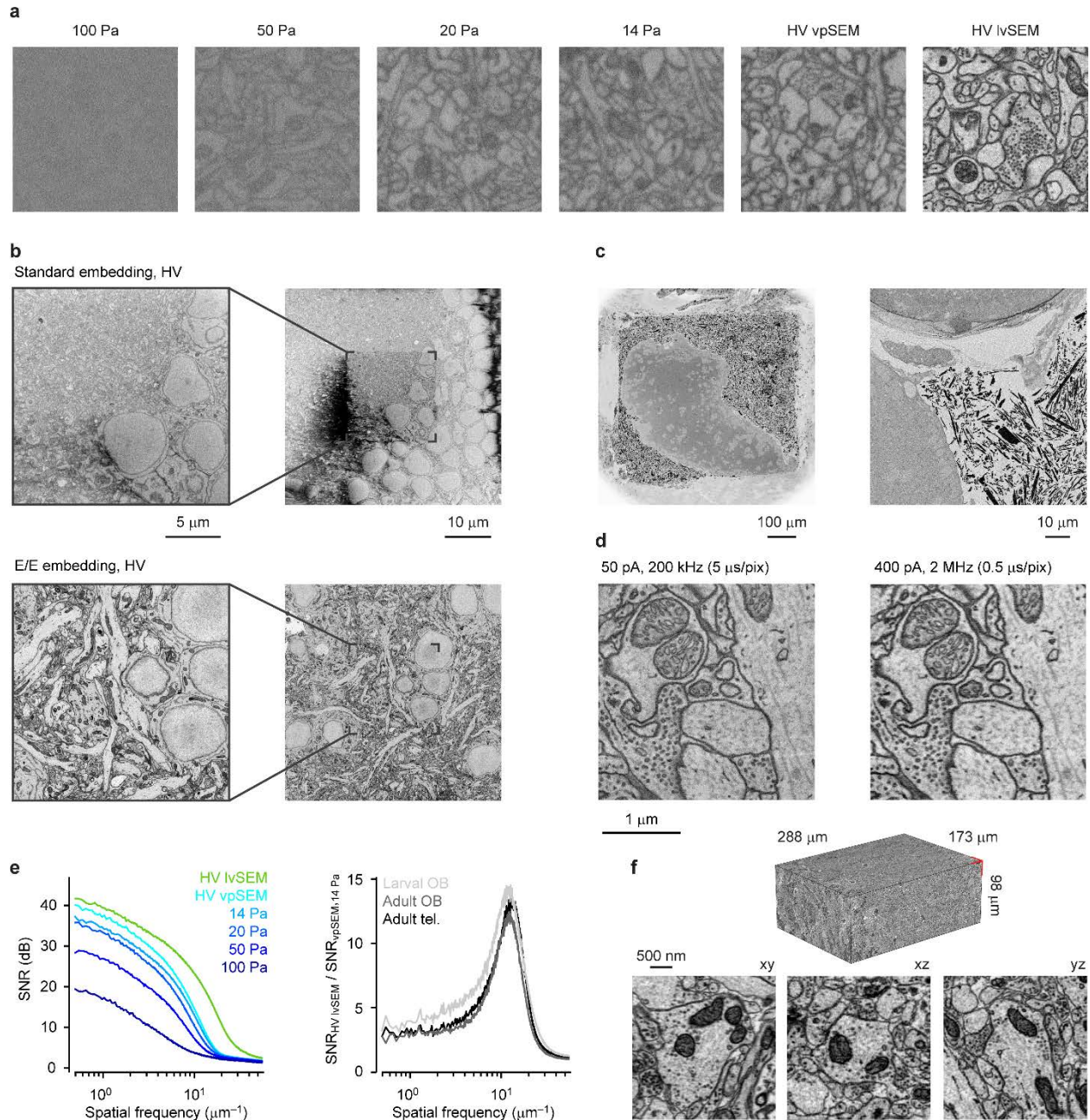


Figure 5 E/E embedding. (a) Images in the same region of interest from the same sample (adult zebrafish telencephalon; E/E-embedded) taken at different pressures in a vpSEM and in high vacuum (HV) in an lvSEM. Other imaging parameters were kept constant (Supplementary Figure 1). Scaling was adjusted for the image with the highest contrast (HV lvSEM). (b) Images of ROTO-stained samples (adult zebrafish forebrain) embedded in conventional EPON (top) and in E/E (bottom) acquired using the same settings ($E_L = 2$ keV; 200 kHz; beam current ~ 50 pA). After acquisition of the images on the left, images on the right were acquired at lower magnification to visualize charging effects. In all images, the grayscale spans -2.5 to $+2.15$ standard deviations around the mean. (c) ROTO-stained samples embedded in E/E. Left: overview of sample block (telencephalon of adult zebrafish). Right: close-up on the edge of the tissue (zebrafish larva). Silver particles (black) are visible outside the tissue. (d) Images of the same sample (adult zebrafish telencephalon) acquired at 200 kHz and 2 MHz ($E_L = 1.5$ keV; 4 nm/pixel; beam current adjusted as shown). (e) Left: SNR as a function of spatial frequency and imaging condition for images of the same sample (adult telencephalon, E/E). Right: The benefit of E/E embedding was assessed for the three E/E-embedded samples by the ratio of the SNR obtained with the lvSEM and the SNR obtained with the vpSEM at 14 Pa. See Supplementary Figure 1 for additional information. (f) Large image stack acquired at high speed (adult zebrafish OB; E/E-embedding; $E_L = 1.5$ keV;

$D_e = 15.9 - 17.3 \text{ e}^-/\text{nm}^2$; 2 MHz; $9 \times 9 \times 25 \text{ nm}^3$ voxels; high vacuum). Individual images consisted of 40 tiles, each with 4096×4096 pixels. Right: reslices through a subvolume.

We fixed and stained brain tissue of larval or adult zebrafish using the ROTO (reduced OsO_4 – thiocarbohydrazide – OsO_4) method with uranyl acetate and lead aspartate to contrast membranes (Deerinck et al. 2010, Tapia et al. 2012) and embedded samples in EPON. The block face was imaged by detecting backscattered electrons in a vpSEM with an automated ultramicrotome in the vacuum chamber. Beam current, pixel rates and landing energies (E_L) were $\sim 50 \text{ pA}$, $180 - 250 \text{ kHz}$, and $\sim 2 \text{ keV}$, respectively. In low vacuum ($10 - 20 \text{ Pa}$ water pressure), charging artifacts were mild or absent and sections could be cut at $<30 \text{ nm}$ thickness, consistent with previous studies (Briggman et al. 2011, Helmstaedter et al. 2013). In high vacuum, however, severe charging artifacts were observed (Figure 5b, top) that often obscured entire images. Moreover, it was often impossible to cut sections at $<50 \text{ nm}$. Hence, efficient charge removal is essential for image acquisition in high vacuum.

In low vacuum, mild charging artifacts were occasionally observed in areas of low heavy metal content whereas densely stained areas showed no charging artifacts, consistent with previous results (Briggman et al. 2011, Titze et al. 2013). Because weakly stained regions are found mainly outside the tissue we introduced conductive material into this space. The sample was removed from the EPON resin before it hardened and transferred into a two-component epoxy glue (Epo-Tek EE129-4) with silver particles. Systematic tests identified a ratio of the two Epo-Tek components A and B (1.25/1.00) that resulted in highly conductive sample blocks (resistance $<1 \text{ Ohm}$) while retaining the ability to reliably cut thin sections (see below). We refer to this approach as Epo-Tek/EPON (E/E) embedding. In SBEM images of E/E-embedded samples, silver particles were found outside the tissue but not inside, as expected from their size (up to $45 \text{ }\mu\text{m}$; Figure 5c). Nevertheless, images could be acquired in high vacuum without obvious charging artifacts (Figure 5b, bottom) and sections could be cut routinely at 25 nm (Supplementary Movie 1). Hence, E/E embedding resolved problems arising from sample charging.

High vacuum provides the opportunity to use a broader class of microscopes including specialized low-voltage SEMs (lvSEMs) that provide high beam quality at very low E_L ($<2 \text{ keV}$). Because the penetration depth of electrons increases with E_L , low E_L ($<2 \text{ keV}$) is desired to avoid damage and cross-talk between images when sections are thin (e.g., 25 nm). We found that high-quality images could be obtained with a lvSEM at E_L as low as 1.5 keV (Figure 5a,d; Supplementary Figure 1) whereas $E_L \geq 2 \text{ keV}$ was usually required using a vpSEM. As expected, images acquired with an lvSEM ($E_L = 1.5 \text{ keV}$) were sharper and more contrasted than images acquired with a vpSEM ($E_L = 2 \text{ keV}$; Supplementary Figure 1). Many lvSEMs also offer high beam currents at low E_L , providing the opportunity to maintain a constant electron dose

D_e throughout a wide range of acquisition speeds. We found that high image quality could indeed be maintained when the acquisition rate was varied from 200 kHz, a typical rate used previously (Briggman et al. 2011), to 2 MHz in an lvSEM (Figure 5d; Supplementary Figure 1). Hence, the use of lvSEMs can substantially increase the resolution and speed of SBEM imaging.

To quantify benefits of E/E embedding we imaged the same brain samples in a vpSEM under different pressures and in an lvSEM (Figure 5a; Supplementary Figure 1). In each sample, stacks of images (2048 x 2048 pixels, 9 x 9 nm², 30 nm section thickness, 50 images) were acquired in each of five regions of interest containing neuropil and somata. E_L (2 kV), beam current (60 pA) and acquisition rate (200 kHz) were kept constant. Three E/E-embedded samples (adult zebrafish telencephalon, adult zebrafish OB, larval zebrafish OB) and one sample embedded in standard EPON (larval zebrafish OB) were analyzed. To assess image quality we computed the signal power-to-noise power ratio (SNR) as a function of spatial frequency. The SNR systematically increased with decreasing pressure in the vpSEM (Figure 5e). Images acquired with the lvSEM had the highest SNR and their spectra extended further into the high frequency range, indicating higher resolution. As expected, no obvious effects of E/E embedding on SNR were observed for pressures between 100 Pa and 20 Pa (Supplementary Figure 1). At lower pressures, however, charging artifacts precluded stable image acquisition without E/E embedding. To conservatively assess the benefits of E/E embedding we quantified the ratio between the SNR obtained with the lvSEM and the SNR obtained with the vpSEM at 14 Pa for the same samples (Figure 5e). At high spatial frequencies, which are particularly important for neurite tracing and synapse annotation, the SNR obtained in the lvSEM was >10-fold higher. We therefore conclude that E/E embedding enables an increase in SNR of the most relevant image features by approximately an order of magnitude.

To assess SBEM of E/E-embedded samples for large volumes we acquired a large image stack from the olfactory bulb of an adult zebrafish at high speed (2 MHz) with a resolution desired for neuronal circuit reconstruction (9 x 9 x 25 nm³ voxels; high vacuum; 173 x 288 x 98 μm³; 3918 sections; 32 days imaging time including overhead; 6.4 TB unstitched at 16 bit/voxel; final size 2.2 TB stitched at 8 bit/voxel; lvSEM). To cover a large area we acquired 40 overlapping image tiles per plane, each consisting of 4,096 x 4,096 pixels. Tiling further complicates thin sectioning, presumably because overlapping areas are exposed multiple times to the electron beam. Nevertheless, 25 nm section thickness and high image quality could be maintained throughout the stack (Figure 5f; Supplementary Figure 2; Supplementary

Movies 2,3). E/E-embedding therefore alleviates technical problems that complicate the acquisition of large ultrastructural image stacks.

2.3.2 Neuron reconstruction

A critical problem in large reconstruction tasks is the overhead for the recruitment, training, and management of human tracers (Helmstaedter 2013). For example, >200 tracers were recruited from local student populations or >100,000 volunteers were recruited via the internet to reconstruct local circuits of up to 950 neurons in the retina (Helmstaedter et al. 2013, Kim et al. 2014). In order to alleviate this problem we outsourced stereotyped tracing tasks to a professional service (www.ariadne-service.ch).

We trained >30 tracers of the service to perform skeleton tracing using the open-source tracing applications KNOSSOS (Helmstaedter et al. 2011) (www.knossostool.org) or PyKNOSSOS, a new Python-based software package with additional functions for neuron tracing, synapse annotation and visualization (Supplementary Figure 3; Supplementary Methods). Each tracer completed an initial training program (~20 h) that included regular feedback from an expert scientist. After training, tailored feedback was directed to individual tracers to further optimize their performance. The service handled the recruitment of tracers, the implementation of the training program, the supervision of tracers after training, and administration. Tasks for expert scientists therefore reduced to the design of the training program, the supervision during training, and data analysis.

Reconstruction performance was quantified in an SBEM image stack from the brain of a zebrafish larva (4.5 days post fertilization [dpf]). The sample was embedded in E/E and imaged in high vacuum using a vpSEM ($E_L = 2 \text{ keV}$; $D_e = 17.5 \text{ e}^-/\text{nm}^2$; $9.25 \times 9.25 \times 25 \text{ nm}^3$ voxels; 4,750 sections; Supplementary Figure 3; Supplementary Movies 4,5). The stack contained one full OB and parts of the adjacent telencephalon ($72.2 \times 107.8 \times 118.6 \text{ }\mu\text{m}^3$). Reconstructions were initiated from all somata within the presumptive boundary of the OB and completed for all cells with neuron-like morphology. Initially, 1,001 cells were reconstructed using the following workflow:

1. Expert scientists registered and stitched SBEM image stacks, divided them into cubes for dynamic data loading by KNOSSOS (Helmstaedter et al. 2011) or PyKNOSSOS, and defined seedpoints to start skeleton tracing (usually somata).
2. Skeletons were traced from each seed using KNOSSOS or PyKNOSSOS.

3. Consolidated reconstructions of each neuron were generated from multiple independent tracings by the reannotation procedure described below. This process involved the identification of mismatch points and the local re-tracing around mismatch points (“focal reannotation”).

2.3.3 Identification and correction of reconstruction errors

The accurate reconstruction of neuronal circuits critically depends on the identification and correction of tracing errors. For skeleton reconstructions, this problem has been addressed by the “redundant-skeleton consensus procedure” (RESCOP) (Helmstaedter et al. 2011), a systematic approach that selects a consensus from multiple independent tracings based on statistical models of tracing errors (Helmstaedter et al. 2011). Previous studies used RESCOP based on 4 – 6 independent reconstructions (Helmstaedter et al. 2013). Because reconstructions are costly we explored whether accurate reconstructions can be achieved with lower initial redundancy (fewer independent tracings) when targeted expert input is included in the reannotation process.

In the sample of the larval zebrafish OB, each of the 1,001 cells was initially traced 3 times using KNOSSOS or PyKNOSSOS. Each tracing yields a skeleton that is defined by points in 3D space (nodes) and edges connecting nodes. A consolidated skeleton was then computed for each neuron by the following procedure (“COvergence by Redundancy and Experts” [CORE]; Figure 6):

1. Node density was resampled to one node per 100 nm and nodes from redundant skeletons were combined into “primary cliques” when they were within 100 nm of each other.
2. Starting at these cliques, nodes of at least two tracers were combined into additional cliques when they were connected to the same previously defined clique (see Methods for details).
3. The consolidated skeleton was computed by averaging the coordinates of nodes within the same clique and a subsequent morphology and topology optimization procedure (Methods).

Consolidated skeletons thus include segments that were recognized by at least two tracers. The remaining “uncertain segments” were further analyzed by the following reannotation procedure:

4. Consolidated nodes connected to “uncertain segments” were defined as “mismatch points” and inspected by a scientific expert. Unlike tracers, the expert had access to all available tracings to identify potential discrepancies. The expert was allowed to delete segments, to add new segments, and to override tracers but usually intervened only when a mistake such as a wrong branch was immediately obvious.

5. Local segments ($\sim 2 \mu\text{m}$ length) around the remaining mismatch points were traced by two additional tracers. Unlike experts, tracers had access to the preliminary consolidated skeleton but not to the raw tracings. If a tracer confirmed an associated uncertain segment, the tracer followed the segment and all its branches to the end.
6. The consolidated skeleton was computed again as above.
7. The procedure was repeated until all mismatch points were resolved.

The total length of the 1,001 consolidated skeletons was 492 mm while the total length of neurites traced was 1,981 mm. Even though the redundancy was 3, the total process length was >3-fold the length of consolidated skeletons because precision errors (tracing into incorrect neurons) added neurite length. Moreover, additional neurite length was generated by revisions, which locally increase redundancy. The fraction of expert time in the total tracing time (25,478 h) was only 3.0 %. The probability of missing segments was low because even those segments that were initially annotated by only one tracer were subsequently re-evaluated by other tracers or an expert. Many tracers had long-term experience (>1,000 h), which appears to increase tracing accuracy (Supplementary Figure 5).

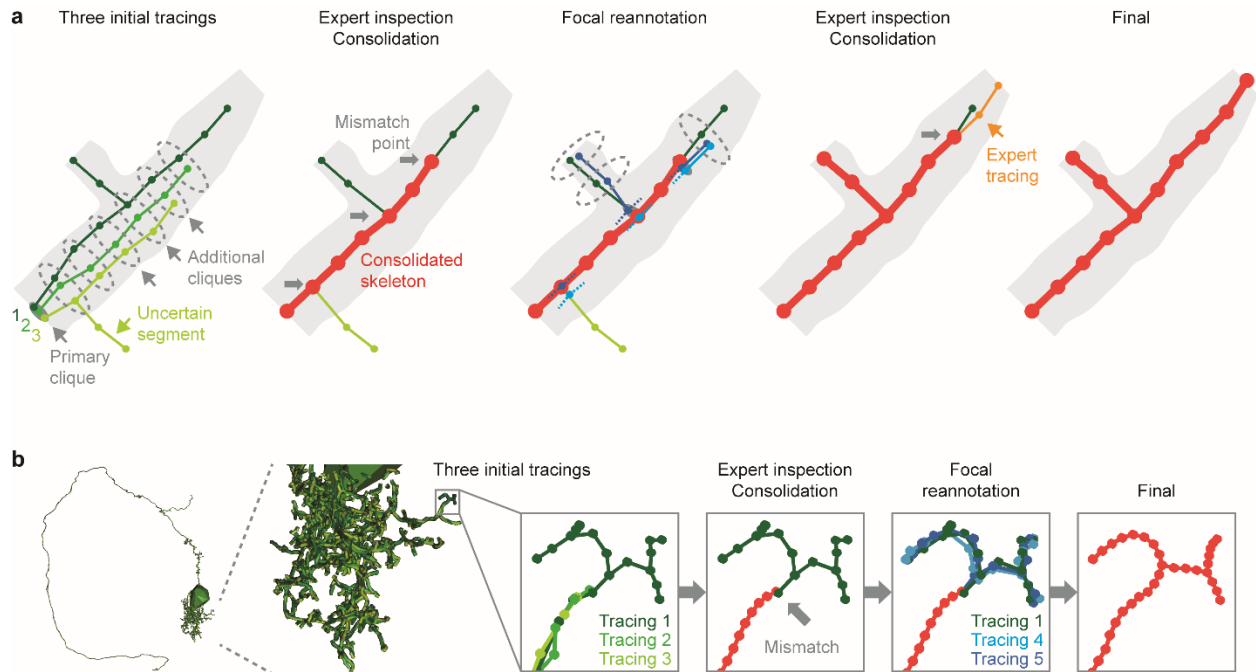


Figure 6 Reconstruction of neurons by CORE. (a) Schematic illustration of CORE based on three initial tracings. Starting from a primary clique of tightly associated nodes (<100 nm apart; e.g., at a seed point), additional cliques are established when multiple nodes are connected to the same previous clique. A consolidated skeleton is generated by connecting centroids of cliques. Nodes connecting the consolidated skeleton to segments identified by only one tracer (uncertain segments) are mismatch points. An expert inspects each mismatch point but usually interferes only when obvious mistakes are detected or when tracing is particularly difficult. Unlike tracers, the expert has access to all tracings. Segments around mismatch points are resolved by the expert or re-annotated by two additional tracers and the consolidated skeleton is updated. The process is repeated until all mismatch points are resolved. (b) Example of error correction in a MC of the larval zebrafish (no expert intervention).

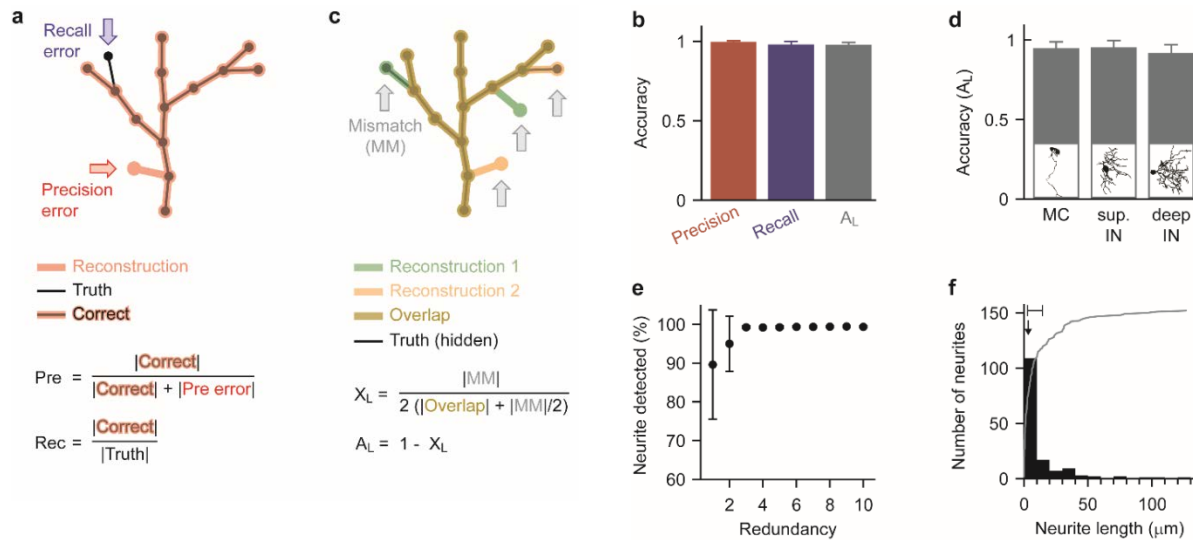


Figure 7 Quantification of reconstruction accuracy. **(a)** Schematic illustration of precision and recall. **(b)** Accuracy of reconstructions by CORE (mean \pm s.d.). Precision and recall were measured for $n = 8$ independent reconstructions of the same mitral cell against a ground truth generated from 26 individual reconstructions by expert correction. A_L was quantified by pairwise comparisons between the 8 independent reconstructions. **(c)** Schematic illustration of A_L . **(d)** Reconstruction accuracy (A_L) for three different types of neurons in the larval zebrafish OB (mean \pm s.d.; $n = 3$ neurons for each type). Insets show examples of each neuron type. **(e)** Fraction of ground truth neurite length detected by at least one tracer as a function of redundancy (mean \pm s.d.; same neuron as in **(a)**; n is given by rounding $26/\text{redundancy}$ down to the next integer). **(f)** Length distribution of missed branches, determined by tracing of orphan neurites. Gray curve shows cumulative distribution. Arrow and horizontal bar show median and inter-quartile range, respectively.

2.3.4 Quantitative analysis of reconstruction errors

Reconstruction accuracy was first quantified by precision, a measure of errors due to wrongly traced processes), and recall, a measure of errors due to missing processes (Figure 7a). To establish the ground truth required for these measures, a mitral cell was traced by 26 tracers and an expert corrected all mismatches. We then drew eight non-overlapping subsets of three tracings from the pool of 26 to generate eight consolidated skeletons through CORE. Precision and recall relative to ground truth were 1.00 ± 0.01 and 0.98 ± 0.02 , respectively (mean \pm s.d.; $n = 8$; Figure 7b).

Because accurate ground truth is expensive and usually not available we also devised another procedure to estimate accuracy (Figure 7c). The procedure requires only two independent reconstructions and is based on two simplifying assumptions: (1) independent errors do not overlap, and (2) precision and recall errors are approximately equal. We first determined the length of the mismatch between the two reconstructions and the length of their overlap. The true process length was then estimated as the overlap plus half the mismatch length because the mismatch is assumed to include correct and incorrect branches. Mismatch length was normalized by the estimated true length to obtain a measure of the relative deviation between both reconstructions and the truth. Because both reconstructions should, on

average, be equidistant from the truth, this value was divided by two to obtain a “relative length error”, X_L , and a corresponding accuracy measure, $A_L = 1 - X_L$. For the eight independent reconstructions of the mitral cell, A_L was slightly lower than precision or recall (0.98 ± 0.01 ; Figure 7b; mean \pm s.d.) because X_L combines precision and recall errors.

We used A_L to estimate reconstruction accuracy for three morphologically different types of neurons: mitral cells, superficial INs, and deep INs (Figure 7d; $n = 3$ neurons for each type). Mitral cells and superficial INs were of similar length (average length: $502 \pm 51 \mu\text{m}$ and $447 \pm 176 \mu\text{m}$, respectively; mean \pm s.d.) but INs lacked a projecting axon. Deep INs were substantially larger ($1098 \pm 416 \mu\text{m}$; mean \pm s.d.). For MCs, A_L was not significantly different from the value obtained by comparison against ground truth (0.95 ± 0.04 ; $p = 0.11$; Wilcoxon rank-sum test). For superficial and deep interneurons, A_L was 0.95 ± 0.04 and 0.92 ± 0.05 , respectively (Figure 7d). These results confirm that CORE with redundancy 3 can achieve high accuracy.

The design of efficient reconstruction procedures depends on the tradeoff between the number of initial tracings (redundancy), which accounts for much of the workload, and the resulting accuracy. Using CORE, redundancy should have only minor effects on the final precision error because wrong branches are efficiently corrected during reannotation. Recall errors (missed processes), in contrast, may increase with decreasing redundancy because undetected branches cannot be repaired. The final accuracy of CORE should therefore depend primarily on the fraction of the ground truth that is present in at least one of the initial reconstructions. For the neuron used to construct ground truth, we found that this fraction saturated near 100% when redundancy was ≥ 3 (Figure 7e). Hence, CORE with redundancy 3 is an efficient procedure to generate accurate reconstructions.

2.3.5 Completeness of neuron reconstruction and synapse annotation

To further assess consequences of recall errors we took advantage of the high density of our tracings. In order to identify missing processes of previously traced neurons we initiated additional reconstructions at cross-sections through previously untraced neurites. These “orphan” neurites are expected to comprise not only missed processes but also processes of previously untraced neurons, in particular centrifugal inputs to the OB. By tracing 339 orphan neurites, we identified 152 “missed neurites” that connected to neurons reconstructed previously. Most of these missed neurites were very short (median: $3.4 \mu\text{m}$; interquartile range: $0.6 - 11.0 \mu\text{m}$; Figure 7f). Hence, recall errors affected primarily short terminal branches.

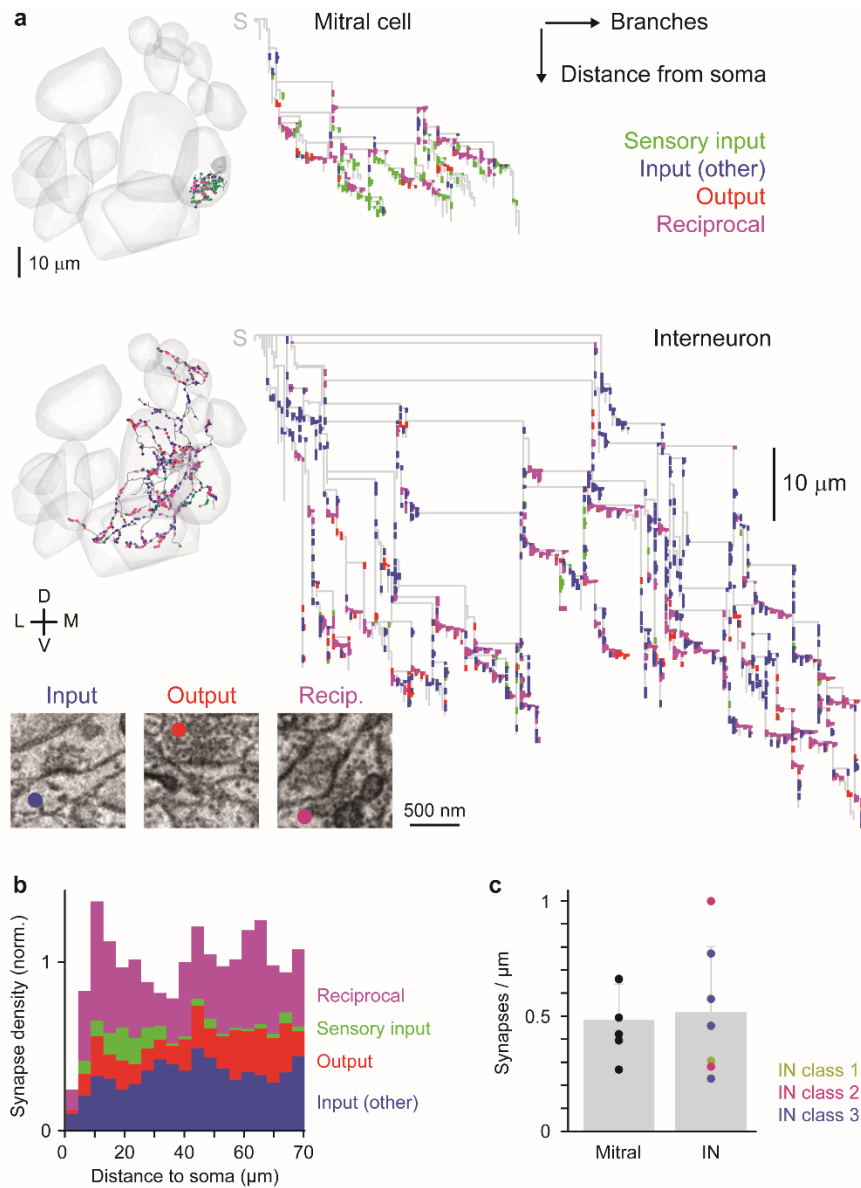


Figure 8 Subcellular distribution of synapses. **(a)** Annotation of synapses in a MC (top; $n = 153$ synapses; axon excluded) and in an IN (bottom; $n = 845$ synapses). Left: morphological reconstruction; right: 2D graphs representing morphological distance from soma (S; y-axis) and branch identity (x-axis). Four classes of synapses are depicted by colors. Reciprocal synapses consist of an input and an output synapse between the same partners within $2.5 \mu\text{m}$. Inset shows examples of synapses made by the interneuron. Colored dots mark profile of the interneuron neurite. **(b)** Synapse density, normalized to the mean, as a function of morphological distance from the soma, averaged over all annotated neurons ($n = 6$ MCs and $n = 7$ INs). **(c)** Mean synapse density (\pm s.d.) of MCs and INs. Each plot symbol represents one neuron. IN classes correspond to Figure 9c.

The omission of small terminal branches may have severe consequences if these branches carry a large number of synapses. To address this possibility we annotated the synapses of six MCs and seven INs with diverse morphologies and soma locations (4,657 synapses in total). Each synapse was assigned to one of three classes: sensory input, non-sensory input, and output. Synapses of olfactory sensory neurons (OSNs) were distinguished from other inputs by their dark cytoplasmic staining (Pinching et al. 1971). The subcellular organization of synapses was analyzed by visualizing individual neurons in 3D and by 2D-graphs (Figure 8a; mitral cell axon excluded). Inputs from sensory neurons were frequently observed in MCs but rare in INs. Some INs contained long neurite segments with few branches and synapses. In general, however, no strong compartmentalization of synapses or synapse types was observed. On average, the density of synapses did not vary substantially with the distance from the soma (Figure 8b) or between neuron types (Figure 8c). Synapses can therefore exhibit complex subcellular distributions in individual neurons but are not highly concentrated near endpoints. Hence, small recall errors affecting terminal branches are unlikely to have catastrophic effects on the reconstruction of OB circuitry.

A characteristic feature of the adult OB are reciprocal synapses, which were defined as adjacent synapses (distance < 2.5 μm) in opposite directions between the same pair of neurons. We found a substantial number of reciprocal synapses in all examined MCs and INs (Figure 8a,b).

In order to estimate the total number of OB neurons we focused on the presumptive boundary of the OB where somata of OB neurons are directly adjacent to, and partially intermingled with, a large number of telencephalic somata (Supplementary Figure 6; Supplementary Movie 6). 95 additional candidate cells near the presumptive boundary were reconstructed with redundancy 3. Among these, 21 cells had neurites in the OB and were fully reconstructed using CORE. The remaining cells did not project into the OB or were non-neuronal cells. We observed that primary neurites of OB neurons were always directed towards the OB whereas primary neurites of other neurons pointed in other directions. Using this criterion, we screened additional somata and estimated the number of remaining OB neurons to be 25 (Supplementary Figure 6; Supplementary Movie 6). The total number of OB neurons was therefore estimated to be 1,047 (1,001 + 21 + 25). Out of these, 1,022 (98 %) were reconstructed by CORE (Supplementary Movie 7).

2.3.6 The neuronal repertoire of the olfactory bulb

The OB receives input from OSNs in the nose that converge onto olfactory glomeruli and make synaptic connections with MCs and INs (Pinching et al. 1971, Axel 1995, Wilson et al. 2006). MCs are glutamatergic, receive input from one or a few glomeruli, and project to multiple target areas (Li et al. 2005, Fuller et al. 2006, Miyasaka et al. 2009, Miyasaka et al. 2014). MCs associated with different glomeruli do not appear to make direct synaptic contacts (Wilson et al. 2006) but communicate via INs. Most INs are GABAergic and fall into three broad categories (periglomerular cells, short-axon cells and granule cells) but the precise organization of IN networks is poorly understood.

In the adult OB, the number of INs, particularly granule cells, greatly exceeds the number of MCs (zebrafish: ~25,000 INs and ~1,500 MCs; rodents: $\sim 5 \times 10^6$ INs and ~50,000 MCs) (Rosselli-Austin et al. 1979, Yaksi et al. 2007, Wiechert et al. 2010). This excess of INs contrasts with other brain areas such as cortex and with the insect equivalent of the OB, the antennal lobe. The majority of INs in the OB arises at late developmental stages (Rosselli-Austin et al. 1979, Li et al. 2005, Mack-Bucher et al. 2007), suggesting that IN networks change substantially during early life. However, it remains unclear whether all IN networks are present already at early stages and grow in number, or whether different IN networks develop sequentially.

We analyzed the organization of the OB at 4.5 dpf when the olfactory system is already functional but the majority of INs is not yet present (Lindsay et al. 2004, Li et al. 2005, Mack-Bucher et al. 2007). Reconstructed OB neurons were initially classified into projection neurons, INs and unclassified cells (Figure 9a). Projection neurons were distinguished from INs by an axon projecting out of the OB. Unclassified cells had glia-like morphology or other properties that distinguished them from mature neurons. The majority of unclassified cells had few processes, suggesting that they were immature neurons or glia. In total, we found 749 projection neurons, 254 INs and 19 unclassified cells. The majority of neurons in the larval OB are therefore projection neurons, contrary to the excess of INs in the adult OB.

Cell types were further analyzed using principal component analysis (PCA) and agglomerative hierarchical clustering based on morphological parameters (Figure 9b; $n = 1,003$ neurons; unclassified cells were excluded). These procedures distinguished two well-separated groups of neurons. Group 1 ($n = 745$ neurons) contained exclusively projection neurons that usually had a compact dendritic tuft. We therefore defined this group as MCs (Li et al. 2005, Fuller et al. 2006, Miyasaka et al. 2009). Group 2 comprised all 254 INs and four additional projection neurons.

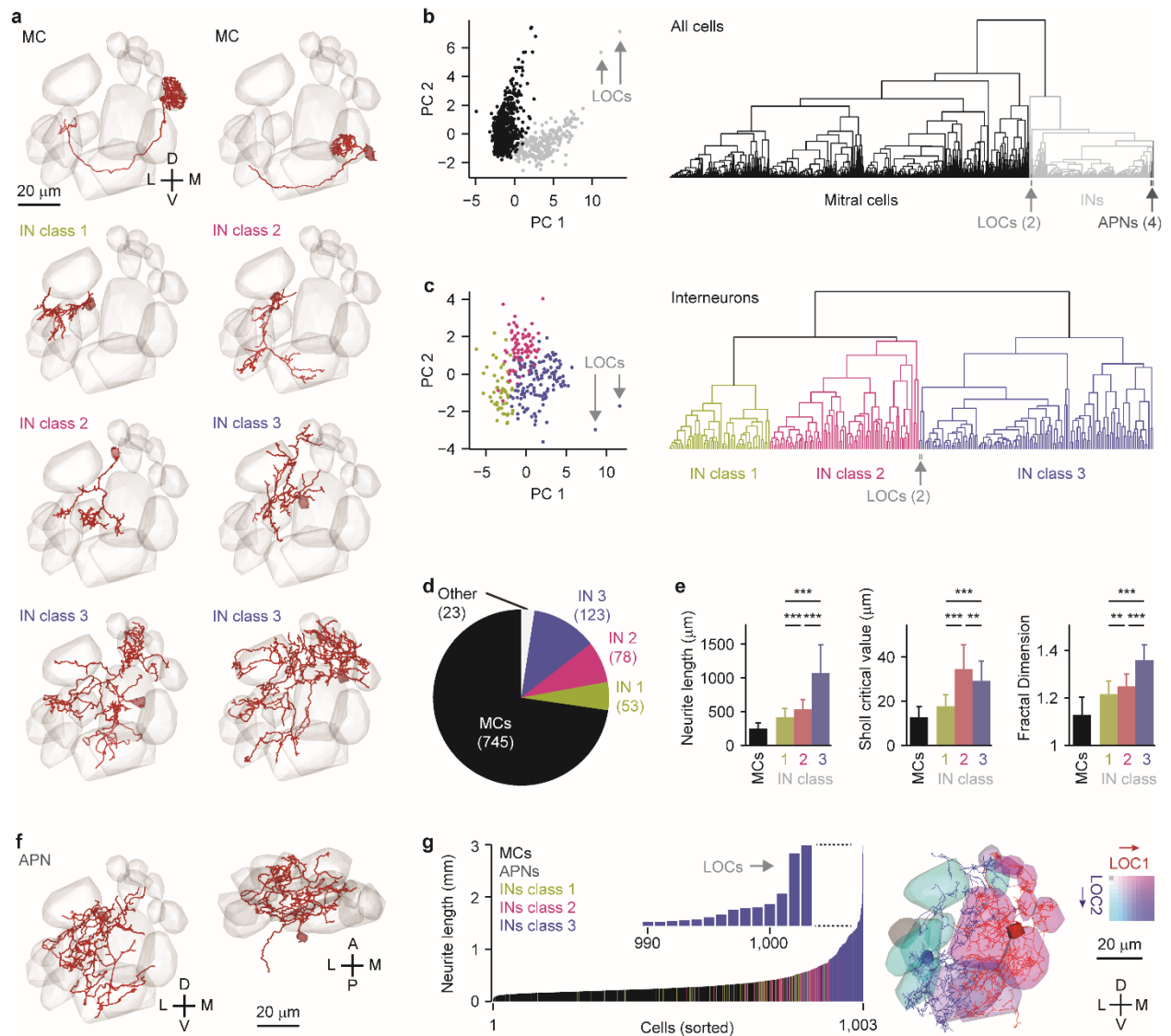
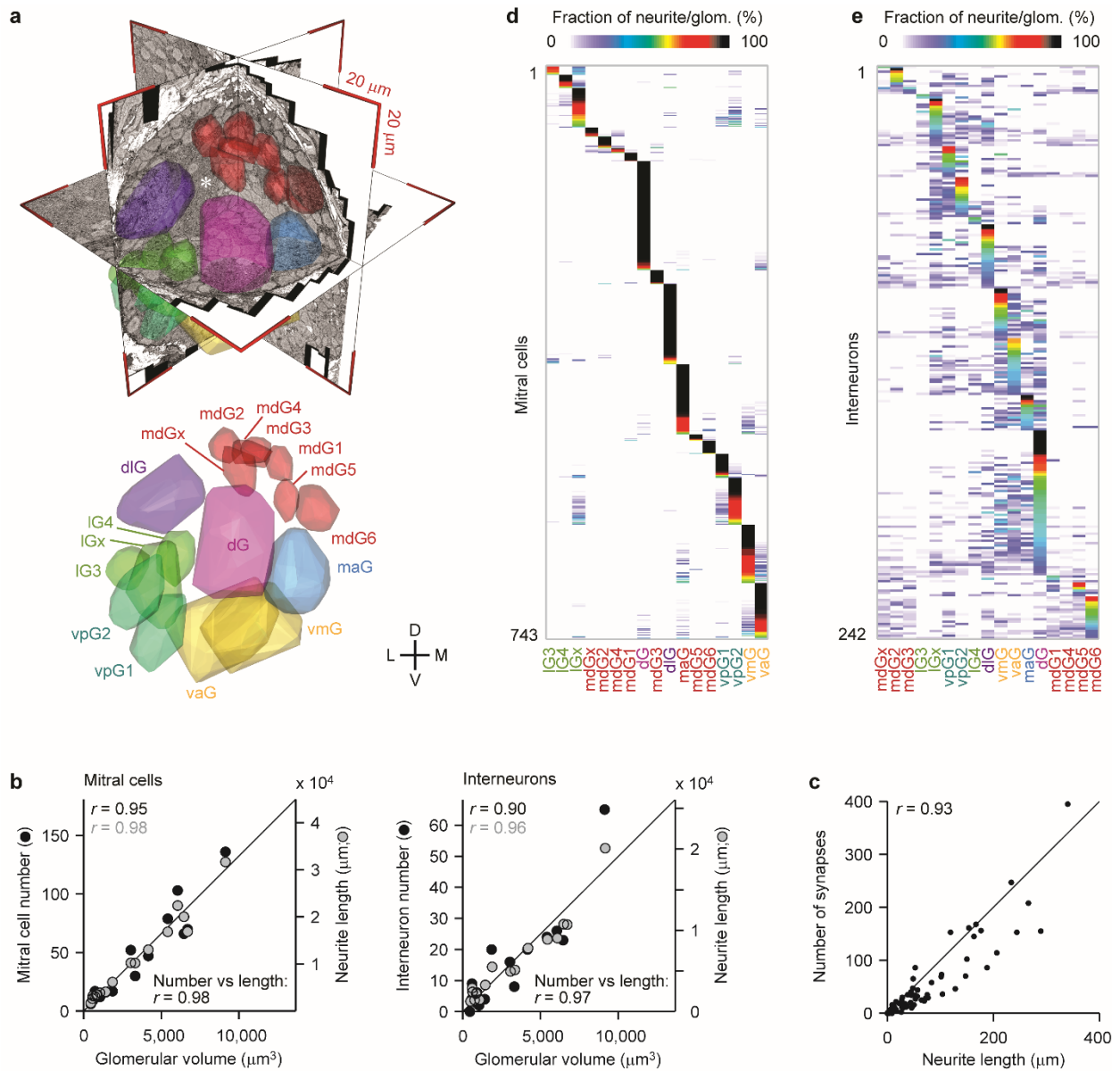


Figure 9 Neurons of the larval zebrafish OB. **(a)** Examples of neurons classified as MCs and INs. Gray volumes show glomeruli. **(b)** Separation of all neurons into two classes by PCA (left) and agglomerative hierarchical clustering (right) based on morphological parameters. All neurons shown in black have an axon and are classified as mitral cells. Neurons shown in gray, except for APNs, are classified as INs and lack an axon. **(c)** Subdivision of INs into 3 classes by PCA and agglomerative hierarchical clustering. **(d)** Numbers of neurons in each class. “Other” cells include APNs and unclassified cells. **(e)** Quantification of morphological properties of INs. Statistical comparisons (Wilcoxon rank-sum test) were performed between IN classes. ***, $p < 0.001$. **(f)** Example of an APN. **(g)** Left: sorted total neurite lengths of all reconstructed OB neurons (unclassified cells excluded). Colors depict classes. Inset: expansion; arrows depict LOCs. Right: LOCs and glomeruli. Color indicates relative innervation of each glomerulus by each LOC. Gray indicates no innervation.

INs were morphologically diverse and often had extensive neurites. Using PCA and agglomerative hierarchical clustering, INs were further subdivided into 3 classes (Figure 9c-e). Class 1 INs were small and located mainly in the glomerular layer, suggesting that class 1 includes primarily periglomerular cells. Class 2 INs were larger, and often contained a long process carrying distal ramifications. Class 3 INs were even larger and often extended neurites in multiple tangential directions. Many INs, particularly from class 3, resembled a superficial IN type in the adult OB that corresponds to short-axon cells in the rodent OB (Kiyokage et al. 2010, Zhu et al. 2013). Consistent with this observation, a transgenic marker for this IN type (*dlx4/6-GFP*) (Zhu et al. 2013) is expressed by >150 neurons of the larval OB (Mack-Bucher et al. 2007). Few INs had the typical morphology of granule cells. Hence, the majority of INs in the larval OB appear to be periglomerular and short axon-like cells while granule cells are rare.

The four projection neurons contained in group 2 did not exhibit the typical morphology of MCs but had widespread neurites, resembling INs of class 2 or 3, and somata in deep layers (Figure 9f). We therefore name these neurons “atypical projection neurons” (APNs). Two other unusual cells were discovered because their total process length (mean \pm s.d.: $2,918 \pm 106 \mu\text{m}$) exceeded that of most other cells (mean \pm s.d.: $373 \pm 302 \mu\text{m}$; Figure 9g) and because they were separated from all other neurons by PCA (Figure 9b,c). The somata of these cells were large, rich in mitochondria, and located in different positions (Figure 9g; Supplementary Movies 8,9). Both cells extended processes into multiple glomeruli but the overlap was low. Processes were thin and did not exhibit the typical sheet-like morphology of glial processes but we failed to detect typical synaptic structures. To our knowledge, such cells have not been described previously in the OB. We therefore name these cells “large olfactory bulb cells” (LOCs).



2.3.7 Neuronal organization of the olfactory bulb

In order to analyze the anatomical basis for inter-glomerular interactions in the OB we determined associations between OB neurons and glomeruli. In zebrafish, glomeruli form a stereotyped pattern that is conserved between individuals (Baier et al. 1994, Dynes et al. 1998, Li et al. 2005, Braubach et al. 2012, Braubach et al. 2013, Miyasaka et al. 2014). During development, the number of identifiable glomerular neuropil volumes increases from ~15 at early larval stages to ~140 in the adult (Braubach et al. 2012, Braubach et al. 2013). We manually delineated neuropil volumes innervated by axons of OSNs, which can be identified by their dark cytoplasmic staining (Pinching et al. 1971). Based on position, morphology and cellular boundaries, we distinguished 17 neuropil regions that are referred to as glomeruli hereafter (Figure 10a; Supplementary Movie 10). 16 glomeruli corresponded to those described previously at a similar developmental stage (Braubach et al. 2012, Braubach et al. 2013). These glomeruli have been divided into seven groups (dG, dlG, vmG/vaG, vpG, lG, mdG, maG) based on the expression of molecular markers for different types of OSNs and other features (Braubach et al. 2012, Braubach et al. 2013). We refer to these glomerular groups as “OSN-defined” groups. The remaining glomerulus was named mdG_x and assigned to the mdG group based on its position (Figure 10a). An additional neuropil volume was found in the central OB but not classified as a glomerulus because it was not innervated by OSNs. This region may therefore be the equivalent of the plexiform layer in the adult OB.

Glomeruli varied substantially in size (Figure 10a) (Braubach et al. 2012, Braubach et al. 2013), which may be due to differences in the number of neurons associated with each glomerulus. Alternatively, larger glomeruli may be innervated by neurons with more extensive neurites. We found that glomerular volume was highly correlated with the number of neurons and with the total intraglomerular neurite length (Figure 10b). The mean neurite length per neuron and per volume was therefore almost identical across glomeruli. This relationship was found for both MCs and INs. Hence, larger glomeruli are innervated by more neurons but the average contribution of each neuron is almost constant. The number of synapses per glomerulus scaled nearly linearly with intraglomerular neurite length (Figure 10c), implying that number of intraglomerular synapses also scales with glomerular volume.

MCs had compact dendritic tufts, usually within a single glomerulus near the soma (Figure 9a; Supplementary Figure 7, Supplementary Figure 8; Supplementary Movies 11,12). No MCs with multiple dendritic tufts in distant glomeruli were observed. Many INs, in contrast, visited multiple glomeruli that were often remote from the soma (Figure 9a; Supplementary Movies 13,14). In order to quantify the

association between neurons and glomeruli we determined the relative innervation of each glomerulus by each neuron. Relative innervation of a glomerulus was defined as the neurite length of a neuron within that glomerulus normalized to the neurite length of the neuron within all glomeruli. The innervation of all glomeruli by all neurons was then represented by an “innervation matrix” (Figure 10d,e). In order to facilitate analysis, neurons (rows) were sorted by their associations with glomeruli: each neuron was assigned to a primary glomerulus based on the maximum innervation length, and neurons assigned to the same glomerulus were further sorted by their relative innervations of this glomerulus. Glomeruli (columns) were sorted by k-means clustering. The number of clusters was set to seven, corresponding to the number of OSN-defined glomerular groups (Braubach et al. 2012, Braubach et al. 2013). Sorted innervation matrices confirmed that MCs were closely associated with single glomeruli whereas INs were often multiglomerular (Figure 10d,e). Hence, inter-glomerular projections are established primarily by INs.

INs may mediate directional inter-glomerular interactions if their input glomeruli are distinct from their output glomeruli. In the OB, however, many neuronal processes are both presynaptic and postsynaptic to other neurons, raising the possibility that interactions are non-directional. Mixed directionality may arise when INs make bidirectional synaptic connections in some glomeruli but unidirectional connections in others. We mapped synapses of individual INs across glomeruli and found that all INs made input and output synapses, including reciprocal synapses, in all innervated glomeruli (Figure 11). The number of synapses varied between glomeruli but the ratio of input-to-output synapses was similar across glomeruli. Hence, the number, but not the direction, of synaptic connections depended on glomerular identity. These results indicate that inter-glomerular interactions have a strong non-directional component.

The innervation matrix of INs exhibited a distinct structure, indicating that inter-glomerular projections of INs are not random (Figure 10e). To further examine this structure we determined the Pearson product-moment correlations between glomerular innervation patterns among INs (rows of the innervation matrix). Projection patterns of INs associated with the same primary glomerulus were highly correlated (Figure 12a; blocks along the diagonal). In addition, correlated projection patterns were found among subsets of INs associated with specific combinations of glomeruli. For example, similar innervation patterns were found among subsets of INs from dG and vaG but not among INs from dG and mdG6. Hence, subsets of INs innervate specific combinations of glomeruli. Innervation patterns of MCs

were highly correlated within but not across glomeruli (Supplementary Figure 5) because MCs were typically associated with single glomeruli (Figure 10d).

We next analyzed relationships between the innervation patterns of different glomeruli (columns of the innervation matrix). All correlations between innervation patterns of glomeruli from the same k-means cluster were positive (maG/dG; Figure 12b), indicating that glomeruli of the same cluster are innervated by similar subsets of INs. Positive correlations were also observed between some glomeruli assigned to different clusters but most correlations across clusters were near zero or negative, indicating dissimilar IN innervation patterns (Figure 12b). This correlation structure cannot be explained by chance effects because it disappeared when relative innervations of INs were shuffled across glomeruli (Supplementary Figure 10). Hence, subsets of glomeruli share similar IN innervation patterns, demonstrating that inter-glomerular projections exhibit a specific structure. Inter-glomerular correlations of MCs innervation patterns were low (Supplementary Figure 9) because most MCs were uniglomerular (Figure 10d; Supplementary Figure 7).

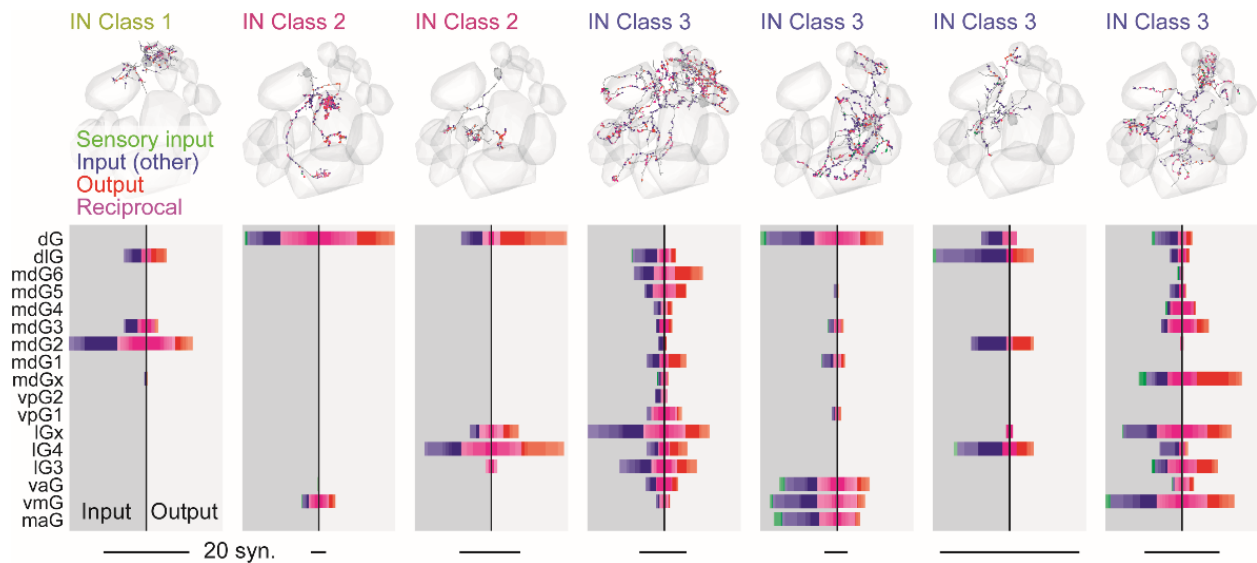


Figure 11 Synaptic innervation of glomeruli by INs. Each panel shows the number of synapses made by one IN in all 17 glomeruli. Colors depict synapse type, shading depicts confidence level between 50% (light) and 100% (strong). Input and output synapses are shown by bars in opposite direction. Reciprocal synapses (pink) are counted as one input and one output synapse. Scale bars show 20 synapses.

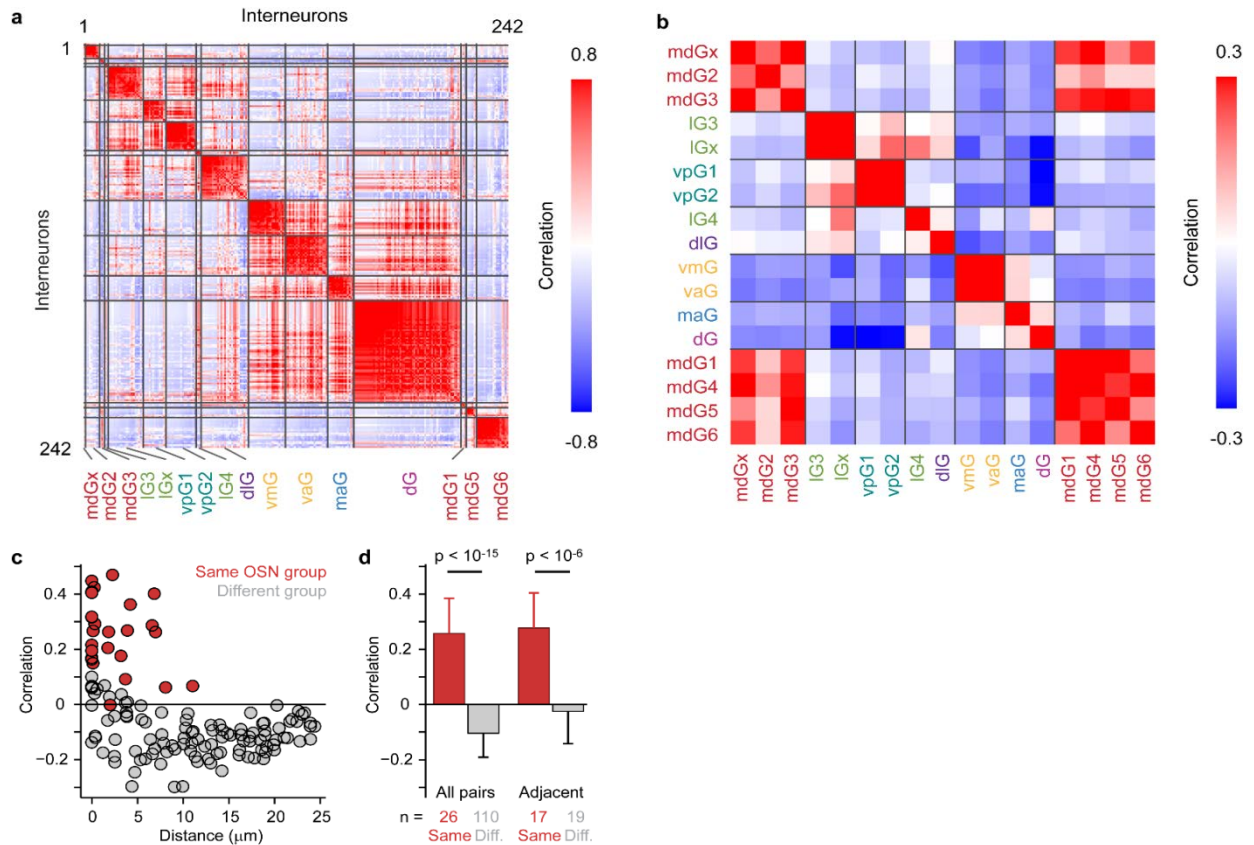


Figure 12 Organization of inter-glomerular projections of INs. (a) Correlation matrix showing similarities between glomerular innervation patterns of INs. INs were sorted as in Figure 10e: each IN was assigned to a primary glomerulus by its maximum innervation, and INs assigned to the same glomerulus were ranked by their relative innervation. Gray lines separate INs assigned to different primary glomeruli. No IN was assigned to mdG₄. (b) Correlation matrix showing similarities between IN innervation patterns of glomeruli, sorted by k-means clustering. Gray lines separate k-means clusters. Color-code of glomerulus labels represents OSN-defined groups (Braubach et al. 2012, Braubach et al. 2013) as in Figure 10a. (c) Correlation between glomerular IN innervation patterns as a function of inter-glomerular distance. Red: pairs of glomeruli from the same OSN-defined groups. Gray: pairs from different OSN-defined groups. Distance was defined as the minimum distance between the 3D-shapes in Figure 10a. (d) Mean correlation (\pm s.d.) between innervation patterns of glomerular pairs from the same and different OSN-defined groups. Left: all pairs; right: pairs of adjacent glomeruli only (distance $< 3 \mu\text{m}$). Statistical comparisons: Wilcoxon rank-sum test.

Most of the glomerular clusters established by k-means clustering based on IN innervation patterns corresponded directly to OSN-defined groups of glomeruli. For example, glomeruli of the third cluster (vpG₁, vpG₂) coincide with the ventro-posterior group (vpG) that is immunoreactive for keyhole limpet hemocyanin (KLH) but not for calretinin or the G-protein subunit G_{αs/olf} (Braubach et al. 2012, Braubach et al. 2013). An exception was the mdG group, which was split into two clusters by k-means clustering (mdG_x/mdG₂/mdG₃ and mdG₁/mdG₄/mdG₅/mdG₆). However, correlations between IN innervation patterns of these two clusters were strongly positive, unlike most other inter-cluster correlations (Figure 12b). Hence, almost all correlations between innervation patterns of glomeruli from the same OSN-defined clusters were positive while most correlations between different OSN-defined groups were negative. Inter-glomerular projections are therefore organized in a glomerulus-specific manner that reflects OSN input.

Glomeruli of the same OSN-defined group are located in common subregions of the OB, raising the possibility that similarities between glomerular innervation patterns are determined primarily by distance. However, distance alone was insufficient to predict the innervation of glomeruli by INs. Some glomeruli showed dissimilar IN innervation patterns even though they were directly adjacent (e.g., dG/mdG_x) while others showed positively correlated IN innervation even though they were more distant (e.g., mdG₆/mdG₄; Figure 12b,c). On average, correlations between glomeruli from the same OSN-defined groups were significantly different from correlations across OSN-defined glomerular groups. This difference remained almost unchanged when the analysis was restricted to directly adjacent glomeruli (Figure 12c,d). Hence, interactions between glomeruli depend primarily on glomerular identity rather than on distance. Inter-glomerular networks of INs therefore exhibit a glomerulus-specific organization, favoring projections between glomeruli that are innervated by common types of OSNs.

2.4 Discussion

The dense reconstruction of neuronal morphology and synaptic connectivity in volumetric EM data is a major goal in neuroscience because it is currently the only approach to determine complex wiring diagrams. However, only few circuits have so far been reconstructed at high density (White et al. 1986, Varshney et al. 2011, Helmstaedter et al. 2013, Takemura et al. 2013). We therefore developed methods to facilitate multiple steps in the workflow of circuit reconstruction.

Sample charging imposes strong constraints on SBEM imaging and is particularly severe when samples are at least partially surrounded by non-conductive resin. E/E-embedding resolves this problem by introducing conductive particles into the surrounding resin. Unlike in-chamber metal coating (Titze et al. 2013), E/E embedding may not eliminate charges uniformly throughout the sample surface but has the advantage that it does not require complex custom technology. The increased conductivity of E/E-embedded samples enabled SBEM imaging and thin sectioning in high vacuum using an IvSEM. Hence, E/E embedding is a simple and effective approach to achieve high resolution, contrast and speed in SBEM.

A critical bottleneck in the reconstruction of neuronal circuits is the massive need for human input. Even though computer-based approaches will become more efficient, human proofreading is expected to remain a rate-limiting operation in the foreseeable future. We used a professional reconstruction service to outsource the bulk of these tasks with minimal overhead. So far, the service has been trained mainly on skeleton tracing and synapse annotation but the potential spectrum of tasks is much broader, limited only by human abilities and available software tools. For example, it is possible to outsource proofreading tasks in semi-automated reconstruction approaches, a demand that is likely to increase steeply. In addition, we created PyKNOSSOS, a Python-based software package for neuron tracing, synapse annotation and visualization that may serve as a versatile platform for further developments (Supplementary Figure 3).

Accurate neuronal reconstructions from EM data require procedures to correct tracing errors. This problem can be addressed using redundant reconstructions and statistical models (Helmstaedter et al. 2011) but redundancy is costly. We therefore used a modified approach, CORE, that leverages expert input and thereby capitalizes on high-level knowledge. CORE makes efficient use of expert input because it directs attention to critical locations. Quantitative analysis demonstrated that CORE with an initial redundancy of 3 is an efficient approach to generate dense reconstructions with high accuracy. Expert input contributed only 3% of the total reconstruction time and may be outsourced in the future.

We reconstructed approximately 98 % of all neurons (1,022/1,047) in the OB of a zebrafish larva. The high density of this reconstruction allowed us to identify rare cell types in the OB. A basic morphological analysis uncovered an atypical type of projection neuron, the APN. APNs may correspond to a subset of short-axon cells in rodents that project out of the OB (Eyre et al. 2008) or it represent a novel cell type. In addition, we discovered an unusual cell type with extensive processes, the LOC, that has, to our knowledge, not been described before. The morphology and ultrastructure suggest that LOCs may be neurons with non-classical transmitter release mechanisms, possibly neuromodulatory neurons, or atypical glia cells.

Surprisingly, ~75% of all neurons in the larval OB were MCs while INs were a minority. Unlike MCs, many INs had extensive neurites that innervated multiple glomeruli. These and additional observations indicate that larval INs represent specific subtypes of INs including periglomerular and short axon-like cells while the large granule cell population develops later. Hence, different sub-circuits of the OB appear to develop sequentially.

The MC : IN ratio in the larval OB (~3:1) is dramatically different from the adult but similar to the projection neuron : IN ratio in the antennal lobe of insects. IN classes 2 and 3 exhibit morphological similarities to INs in the antennal lobe (Stocker et al. 1990, Chou et al. 2010). Interestingly, antennal lobe INs perform a normalization of odor-evoked activity patterns (Olsen et al. 2010) that is closely related to a similar computation (equalization) by short axon-like cells in the zebrafish OB (Zhu et al. 2013). In both cases, inter-glomerular projections of INs are critical to stabilize the mean activity of neuronal populations against variations in input intensity. Hence, INs arising early in development appear to establish a core circuitry that shares structural and functional features with the insect antennal lobe. The subsequent integration of additional INs, particularly granule cells, may extend the computational repertoire of the OB but the functional roles of granule cells are still poorly understood. One approach to address this question may be to examine changes in odor processing during the time window of granule cell development.

The annotation of synapses confirmed that neurites of many OB neurons are presynaptic and postsynaptic to other neurons. Mapping of synapses throughout entire neurons revealed that all INs examined had bidirectional neurites in all innervated glomeruli. Hence, these INs did not have specific input or output glomeruli, implying that inter-glomerular interactions have a strong non-directional component. This finding further supports the notion that INs mediate scaling operations such normalization and equalization.

The dense reconstruction of OB neurons allowed us to analyze the structural organization of inter-glomerular projections of the IN network. Although projections of INs were widespread and complex, subsets of INs preferentially innervated specific groups of glomeruli that receive input from the same types of OSNs. Hence, inter-glomerular projections are organized by glomerular identity. The array of glomeruli is therefore patterned not only presynaptically by receptor-specific projections of OSNs but also postsynaptically by specific projections of INs.

The pattern of inter-glomerular projections could have multiple functional consequences. As OSNs of the same type are likely to detect odors of the same chemical classes (Friedrich et al. 1997, Hansen et al. 2003), selective inter-glomerular connectivity may support differential processing of odor classes. For example, enhanced connectivity among glomeruli of the same group may allow for partially independent normalization of responses to different odor classes. Such an odor class-selective normalization could facilitate the simultaneous analysis of compounds with different biological relevance in a mixture. Moreover, some target areas of the OB such as the habenula or the ventral telencephalon receive input from distinct subsets of OSN-defined glomerular groups (Miyasaka et al. 2009, Miyasaka et al. 2014). Specific inter-glomerular connectivity may thus reflect differential pre-processing of odor information that is routed to distinct target areas and relevant for different behaviors. Another, not mutually exclusive possibility is that specific projections between glomeruli responding to chemically related odors favor inhibitory interactions between processing channels with specific tuning properties. This could be an efficient strategy to accomplish computations such as pattern decorrelation in a small network.

Dense neuronal reconstruction has generated new insights into the organization of the OB and provides a comprehensive anatomical foundation for future studies of circuit development and function. Further insights into the topology of neuronal circuits may now be obtained by the extensive annotation of synaptic connections. Together with measurements of neuronal activity patterns, these approaches have the potential to unravel circuit mechanisms underlying distributed neuronal computations in the OB and other brain areas.

2.5 Methods

2.5.1 Reagents for EM

Cacodylate buffer: 0.15 M cacodylate (Sigma Aldrich 20838), pH 7.4. *EM Fixative*: 2% paraformaldehyde (EMS 15700), 1% glutaraldehyde (EMS 16300), 2 mM CaCl₂ (Sigma Aldrich 53704) in cacodylate buffer, pH 7.4. *RedOs solution*: 3% KFeCN (Sigma Aldrich 31254), 0.3 M ice-cold cacodylate buffer with 4 mM CaCl₂, 4% aqueous OsO₄. *TCH solution*: 1% thiocarbohydrazide (Sigma Aldrich 88535) in bidistilled H₂O (bdH₂O). Incubate for 1h at 60 °C and swirl every 10 min, then cool down to room temperature (RT) and pass through a 0.22 µm syringe filter (VWR 514-0072). *Os solution*: 4% OsO₄ (EMS 19100) in bdH₂O. *UA solution*: 1% uranyl acetate in bdH₂O. *Walton's lead aspartate* (Walton 1979): 0.4% aspartic acid (Sigma Aldrich 1043819) in bdH₂O, add 0.66% lead nitrate (EMS 17900). Incubate at 60 °C for 30 min and adjust to pH 5.5 with 1M NaOH (Sigma Aldrich 72068; at 60 °C). *Epon resin* (Denk et al. 2004): Mix 9.25 ml glycid ether 100 (Serva 21045), 6.25 ml 2-Dodecenylsuccinic acid anhydride (DDSA, Serva 20755), 5 ml methyl nadic anhydride (MNA), 0.325 ml *N*-benzyl dimethylamine (BDMA, Serva 14835) and degas. *E/E*: Epo-Tek EE129-4 components A : B ratio 1.25 : 1.

2.5.2 En bloc sample preparation for SBEM

Samples were fixed and stained en bloc using reduced OsO₄, thiocarbohydrazide (TCH), OsO₄, uranyl acetate and lead aspartate following an established protocol (<http://ncmir.ucsd.edu/sbfsem-protocol.pdf>) (Tapia et al. 2012) with minor modifications. Zebrafish brain tissue was fixed in EM fixative for 1h at RT and 1h on ice. After five washes (always 3 min each) with ice-cold cacodylate buffer, samples were postfixed in RedOs solution for 1h on ice, washed 5 times in bdH₂O, and incubated in fresh TCH solution for 20 min at RT. In a second postfixation step, samples were incubated in Os solution for 30 min at RT and washed 5 times in bdH₂O. Samples were then incubated in UA solution overnight, washed 5 times in bdH₂O, incubated at 60 °C for 30 min in bdH₂O, incubated in Walton's lead aspartate for 20 min at 60 °C, and washed 5 times in bdH₂O at RT. Samples were then dehydrated in an ethanol series (20%, 50%, 70%, 90%, 100%, 100%; 5 min each), incubated in 50% ethanol/50% Epon resin for 30 min, and incubated in 100% Epon resin for 1h at RT. Epon resin was then changed and samples were again incubated at RT for 4-12h (overnight). For conventional sample preparation, the Epon resin was changed again and cured by incubation at 60 °C for 48h. For E/E embedding, the sample was transferred to E/E and moved gently to ensure that silver particles come in contact with the sample. The resin was then cured by incubation at 60 °C for 48h. Conductivity, as measured with an Ohm-meter across the

block, was <1 Ohm. The embedded tissue blocks were glued on aluminum stubs for SBEM (Gatan) using cyanoacrylate glue and trimmed to a block face of the desired size (300 μm \times 200 μm for larval OB; 700 μm \times 600 μm for adult OB).

To prepare samples of the olfactory bulb from zebrafish larvae, fish were anesthetized in tricaine methanesulfonate (MS-222), mounted in low-melting agarose (Sigma Aldrich A9414), and immersed in standard E3 zebrafish medium (Westerfield 2000) (5 mM NaCl, 0.17 mM KCl, 0.33 mM CaCl₂, 0.33 mM MgSO₄, pH 7.4). A small craniotomy was made above the contralateral olfactory bulb using a glass pipette to facilitate the penetration of reagents into the brain. Immediately afterwards, fish were transferred into fixative. Some fish expressed a genetically encoded calcium indicator (GCaMP2 or GCaMP5) (Tallini et al. 2006, Akerboom et al. 2012) under the control of the panneuronal *elavl3* promoter (Ahrens et al. 2012, Ahrens et al. 2013). In some of these fish, responses of olfactory bulb neurons to odor stimulation were measured by multiphoton microscopy prior to sample preparation as described (Li et al. 2005). No difference between these and other samples was observed. The OB or telencephalon of adult zebrafish were dissected from an ex-vivo brain explant (Zhu et al. 2012) and transferred immediately into fixative.

2.5.3 SBEM

Images were acquired using a vpSEM (QuantaFEG 200; FEI) or an lvSEM (Merlin with a GeminiIII column; Zeiss). The vpSEM offers options for low or high vacuum while the lvSEM can be operated only in high vacuum. The lvSEM, but not the vpSEM, contains specialized technology that maintains a highly coherent beam and provides a large range of beam currents in the regime of very low E_L (<2 keV). Both microscopes were equipped with an automated ultramicrotome inside the vacuum chamber (3View, Gatan) that was controlled by DigitalMicrograph™ software (Gatan). Backscattered electrons were detected by a silicon diode detector (Opto Diode Corp., USA) and preamplified by the preamplifier of the 3View system (Gatan). For high-speed data acquisition the main amplifier of the 3View system was replaced by an amplifier with higher bandwidth (DHPCA-100; Femto) to prevent low-pass filtering. Data were acquired using the 3View system with DigitalMicrograph™, which offers a maximum acquisition rate of 2 MHz.

In all experiments, z-series of SBEM images were acquired to test whether thin sections can be cut consistently. Typical pixel sizes were 9 x 9 nm² and the section thickness was usually 25 nm. Tiling was performed by stage movements that were controlled using DigitalMicrograph™. The overlap between

adjacent tiles was 5 – 8% and tile size was small (ca. 40 μm) to minimize image distortions. In the image stack from the adult OB (Figure 5f, Supplementary Figure 2), 70 out of the 3918 sections were replaced by neighboring sections because subsets of tiles were contaminated by debris or corrupted by software errors. In the image stack from the larval OB, one section was lost. The volume of this stack contains >99.96 % of an entire OB and parts of the adjacent telencephalon. The remaining 0.04% of the OB volume is located in glomerulus mdG₆ and accounts for <3.97% of the volume of mdG₆.

2.5.4 Image processing

Stacks of raw 16 bit images were pre-processed, registered and stitched using custom software tools written in MATLAB that allowed for parallel batch processing of large datasets. For image registration, translational offsets between neighboring image tiles were calculated using a custom optimized cross-correlation procedure in MATLAB. In short, the image columns were standardized by subtracting the mean and dividing by the standard deviation of the pixel intensities. The same standardization was subsequently applied to the rows. Translational offsets between neighboring images were calculated by determining the maximum 2D cross-correlation of the standardized images in the Fourier domain. The second inverse Fourier transform was restricted to the central region of the 2D cross-correlogram reflecting a maximal expected offset between overlapping image parts of 256 pixels. Using this procedure the offsets between two 1024 x 1024 pixel images with translational offsets of $dX = 69$ and $dY = 66$ pixels could be calculated in <0.36 s on a laptop computer (Intel® Core™ i7-3520M CPU @ 2.90GHz \times 4, 7.5GB RAM, Ubuntu 12.10). Offsets were used to optimize the tile positions in a global total least square displacement sense. Image contrast was normalized by fitting a Gaussian distribution to the pixel intensity histogram and thresholding at 1.5 – 3 standard deviations around the peak of the Gaussian distribution to convert the images to 8 bit. Stacks were then divided into cubes of 128 x 128 x 128 voxels for dynamic data loading in KNOSSOS or PyKNOSSOS.

2.5.5 Software: PyKNOSSOS

PyKNOSSOS is written in Python (version 2.7) and runs on various operating systems including Linux and Windows 7. Command-line interaction is possible through a built-in Python console. The main graphical user interface is based on the PyQT4 library. All visualizations are done using the VTK-Python bindings. Similar to KNOSSOS, PyKNOSSOS accesses a cubed version of the dataset in which the imaging data is divided into 8-bit cubes of 128 pixel edge length. A custom C++ routine dynamically loads the imaging data in a pre-defined neighborhood around the current focal point into RAM while navigating through the dataset. If multiple versions of the dataset at different zoom levels exist, PyKNOSSOS supports

instantaneous seamless browsing and multi-scale zooming. At a given zoom level l_i , a cubed neighborhood of typically 320 – 576 pixels around the current focal point is loaded into memory for all stored consecutive zoom levels l_{i-1} , l_i and l_{i+1} . This permits navigation through large datasets (>4 TB) with minimal RAM requirements (<4.5 GB). In the default configuration, PyKNOSSOS has five viewports. Image data is displayed in four viewports: the x-y viewport (imaging plane) and three mutually orthogonal viewports of arbitrary orientation. In tracing mode, one of the latter is perpendicular to the current tracing direction. The reslice views are interpolated using a tri-linear interpolation procedure to efficiently extract reslices at arbitrary orientations and zoom levels.

In tracing mode, PyKNOSSOS allows users to put single nodes and connected nodes for skeleton tracing and synapse annotation, to manipulate nodes, and to add searchable comments or tags. An extendable job manager organizes tasks for tracers and provides direct feedback, for example about current tracing speed or tracing instructions. For visualization, nodes and edges can be rendered as points or spheres and lines or 3D tubes, respectively. In addition, point clouds can be represented by their convex hull, for example to outline somata or brain regions. Hundreds of skeletons and regions can be loaded in this way on normal desktop or laptop computers and the visualizations can be interactively manipulated in real time (translation, rotation, zoom, etc.). Various built-in options for display are provided that are designed to support different tracing and visualization tasks. A manual is provided in Supplementary Methods.

2.5.6 Tracing of neurons in the larval OB

To reconstruct the neurons of the larval OB, a presumptive boundary of the OB was delineated manually based on the histological pattern of somata. All of these somata were defined as starting points for reconstructions, which resulted in 1,001 cells classified as OB neurons. Because somata of OB neurons in the caudal OB are sometimes not clearly separated from somata of neurons in the adjacent part of the telencephalon, it is difficult to delineate the boundary of the OB with precision. In order to identify additional OB neurons we reconstructed another 95 additional cells, starting from somata near the presumptive boundary, and identified another 21 OB neurons. The identification of further OB neurons by complete reconstruction appeared impractical because the number of somata near the caudal boundary of the OB is very high (Supplementary Figure 6; Supplementary Movie 6). We therefore used the projection direction of primary neurites as a morphological criterion to identify additional putative OB neurons by tracing only the proximal processes. Using this criterion, the number of remaining OB neurons was estimated to be 25 (Supplementary Figure 6). The total number of neurons in the OB is

therefore estimated to be $1,001 + 21 + 25 = 1,047$. Out of these, 1,022 (98 %) were reconstructed by CORE.

Tracings of OB cells were initiated from seed points close to somata. When cells showed obvious features of glia such as sheet-like processes, tracings were abandoned. A small number of cells was excluded because their morphology was not neuron-like (usually no or only minor processes) or because they did not extend processes into neuropil regions of the OB. All reconstructions of OB cells with neuron-like morphology were completed and included in the analysis. Tracings of orphan branches were initiated at seeds near synapses.

Starting from seed points, tracers followed neuronal processes by placing successive nodes onto cross-sections of neurites in the original image data, resulting in a skeleton representation of each neuron (Helmstaedter et al. 2011). Most skeleton reconstructions were performed by a company, ariadne-service (www.ariadne-service.ch), with input from a scientific expert. Prior to analyzing scientific data, tracers of ariadne-service needed to complete a training program. The program included a general introduction into the task, an introduction to the software, and the tracing of a complete neuron. Throughout the training program, the scientific expert provided feedback on performance and responded to questions. After completion of the training program, the expert continued to receive performance measures of each individual tracer (e.g., tracing speed, internode distances, total tracing hours) and compared skeletons of different tracers for accuracy. Based on these data, the expert delivered tailored feedback to individual tracers in order to further improve performance. Starting already during the training phase, tracers were paid by hour, rather than by neurite length.

2.5.7 Consolidation of skeletons

In order to compute the consolidated skeleton from multiple redundant reconstructions, the skeletons between branch points and end nodes were up-sampled in two steps to an average node density of approximately one node per 100 nm. In the first step, new nodes with 100 nm distance were inserted between original nodes, allowing distances to be occasionally <100 nm to maintain the positions of original nodes. In a second step, positions of nodes <50 nm apart were averaged into a single node unless one of the nodes was a branch point. As a result, most inter-node distances of the up-sampled skeleton were 100 nm, the remaining distances were close to 100 nm, and branch point locations were unchanged.

For each node, nodes of other skeletons were ranked by increasing distance up to a maximal distance of 20 μm and the first five nodes from each skeleton were designated as “potential associates”. Sets of nodes from different skeletons with distances <100 nm were defined as “primary cliques”. At least one primary clique was given by the seed point. Note that primary cliques could consist of a variable number of nodes (≥ 2), and, in rare cases, included nodes from skeletons of different (“incorrect”) tracings. When a node connected to an existing clique had potential associates that were connected to the same clique, these nodes were combined into a new clique. This process was iterated until all nodes were visited. The resulting set of cliques usually had a high degree of overlap because each node could be a member of multiple cliques. Note that the occasional inclusion of nodes from “incorrect” neurons in a clique did not result in propagating errors because these nodes are not connected to the appropriate preceding cliques. The procedure will propagate throughout all connected cliques when initiated from a single primary clique (e.g., the seed point). However, we initiated it from all primary cliques simultaneously to speed up computation.

In order to derive a consolidated skeleton from cliques, weights w_{ij} of potential edges between two cliques i and j were calculated based on the distance d_{ij} between the centroid of the two cliques and the number of connected nodes between the two cliques n_{ij} : $w_{ij} = d_{ij} / n_{ij}$. Edges between cliques were then identified by calculating a minimum weight spanning tree on the weight matrix w_{ij} . Each node can be member of multiple cliques but has a host clique for which the distance between the clique centroid and the node is minimal. To simplify and smooth the reconstruction, cliques that were not a host clique of at least two nodes or were not connected to any other clique were iteratively pruned away. The centroids of the remaining connected cliques were called “consolidated nodes” and formed the consolidated skeleton. Terminal branches with less than three consolidated nodes (approximately 300 nm or less) were removed and the consolidated skeleton between branch points and end nodes was smoothed using the *smoothbranch* procedure in the TREES toolbox (Cuntz et al. 2010) with $p = 0.05$ and $n = 5$. In addition, short terminal branches (<2 μm) running parallel in the vicinity (<0.4 μm) of a longer non-terminal branch were removed.

To quantify reconstruction accuracy, pairs of reconstructions were compared by constructing a virtual consolidated skeleton using the consolidation procedure described above. Mismatches were quantified by the length of uncertain segments. Mismatch segments that were <1 μm or within 625 nm of the virtual consolidated skeleton were discarded because they usually reflected variations between node placements in individual skeletons rather than true topological variations (Helmstaedter et al. 2011).

The overlap was measured as the length of the consolidated skeleton. This procedure slightly underestimates the true overlap, and therefore the final accuracy, because the consolidated skeleton tends to be slightly shorter than the individual skeletons due to averaging and smoothing.

2.5.8 Synapse annotation

After skeleton reconstruction by CORE, synapses were annotated manually by an expert using PyKNOSSOS (Supplementary Figure 3). An automated routine was used to efficiently visit all branches. The viewport showing a cross-section orthogonal to the local neurite was used frequently because it facilitates the simultaneous visualization of the presynaptic vesicle cluster and the synaptic density, which served as criteria for synapse identification. While proceeding automatically from node to node in the presynaptic neuron, synapses were labeled by two clicks: (1) onto the synaptic density, and (2) onto the postsynaptic neuron. If the postsynaptic neuron had been traced previously, the third click connected to the postsynaptic skeleton. Each synapse was given a confidence level and assigned to one of three classes (sensory input, non-sensory input, output). Only synapses with a confidence level >50% were included in the final analysis. Sensory inputs were distinguished from non-sensory inputs by their dark cytoplasmic staining (Pinching et al. 1971). Reciprocal synapses were defined as pairs of non-sensory input and output synapses between the same neurons within a distance <2.5 μm . If multiple combinations of synapses were possible, the pair with the smallest distance was chosen.

2.5.9 Morphological analysis

Morphological clustering of all neurons excluded the axon and was based on measurements of the following parameters for each neuron: (1) presence of an axon (binary parameter), (2) fractal dimension, (3) total process length, (4) number of branch nodes, (5) longest neurite length, (6) volume of the convex hull around all processes, (7) distribution of Euclidian distance of branches from soma (Sholl analysis; third principal component), (8) distribution of terminal node distances from soma (first principal component), (9) distribution of Euclidian distance of branches from soma as a function of branch order (third principal component), (10) number of branches per branch order (second principal component), and (11) distribution of morphological distance of branches from soma along the skeleton as a function of branch order (first principal component). Morphological clustering of interneurons included the number of branches on the longest process as an additional parameter. All measures were transformed into z-scores and clusters were computed based on their correlation. Additional parameters were also determined but not used for clustering because they did not further improve cluster separation. Sholl analysis was performed in 3D. Hierarchical clustering was performed in MATLAB

by calculating an agglomerative hierarchical cluster tree based on ones minus the average correlation between the morphological parameters of the different cells.

2.5.10 Acknowledgements

We thank Christopher Bleck, Bill Anderson and Benjamin Titze for valuable inputs and/or comments on the manuscript, and we thank Willie, Lisa and Rose Ong for help with tracer training and management. This work was supported by the Novartis Research Foundation, the Human Frontiers Science Program (HFSP) and the Swiss National Science Foundation (SNF).

2.5.11 Author contributions

A.A.W. participated in all tasks. He developed E/E embedding, CORE, PyKNOSSOS and analysis procedures. He acquired images from the larval OB, founded ariadne-service, supervised tracers, reconstructed all neurons, annotated synapses, analyzed the data, and participated in writing the manuscript. C.G. participated in sample preparation, methods development, and image acquisition. T.M. participated in sample preparation and image acquisition of the stack from the adult OB. L.S. participated in sample preparation. R.F. participated in data analysis and wrote the manuscript.

2.5.12 Competing financial interests

Part of the results disclosed herein have been included in the patent application WO201/199326. A. A. Wanner is the founder and owner of ariadne-service.

2.6 Supplementary Information

Inter-glomerular network organization of the zebrafish olfactory bulb revealed by dense EM-based reconstruction

Adrian A. Wanner^{1,2}, Christel Genoud¹, Tafheem Masudi^{1,2}, Léa Siksou¹, Rainer W. Friedrich^{1,2*}

³ Friedrich Miescher Institute for Biomedical Research
Maulbeerstrasse 66
4058 Basel
Switzerland

⁴ University of Basel
4003 Basel
Switzerland

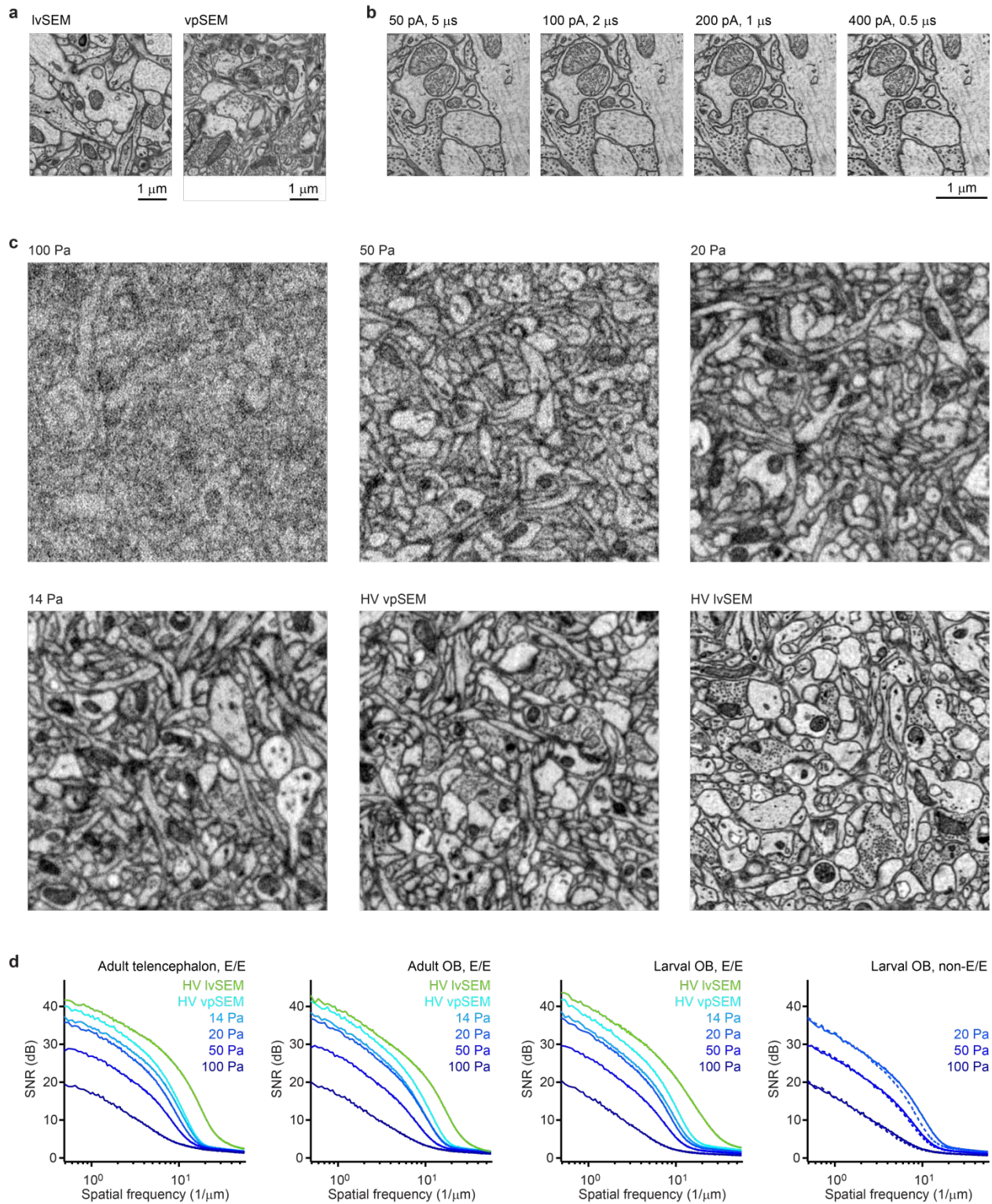
* Correspondence:
Dr. Rainer Friedrich
Phone: +41 61 697 8614
Email: Rainer.Friedrich@fmi.ch

Supplementary Information contains:

Supplementary Figures 1 – 10

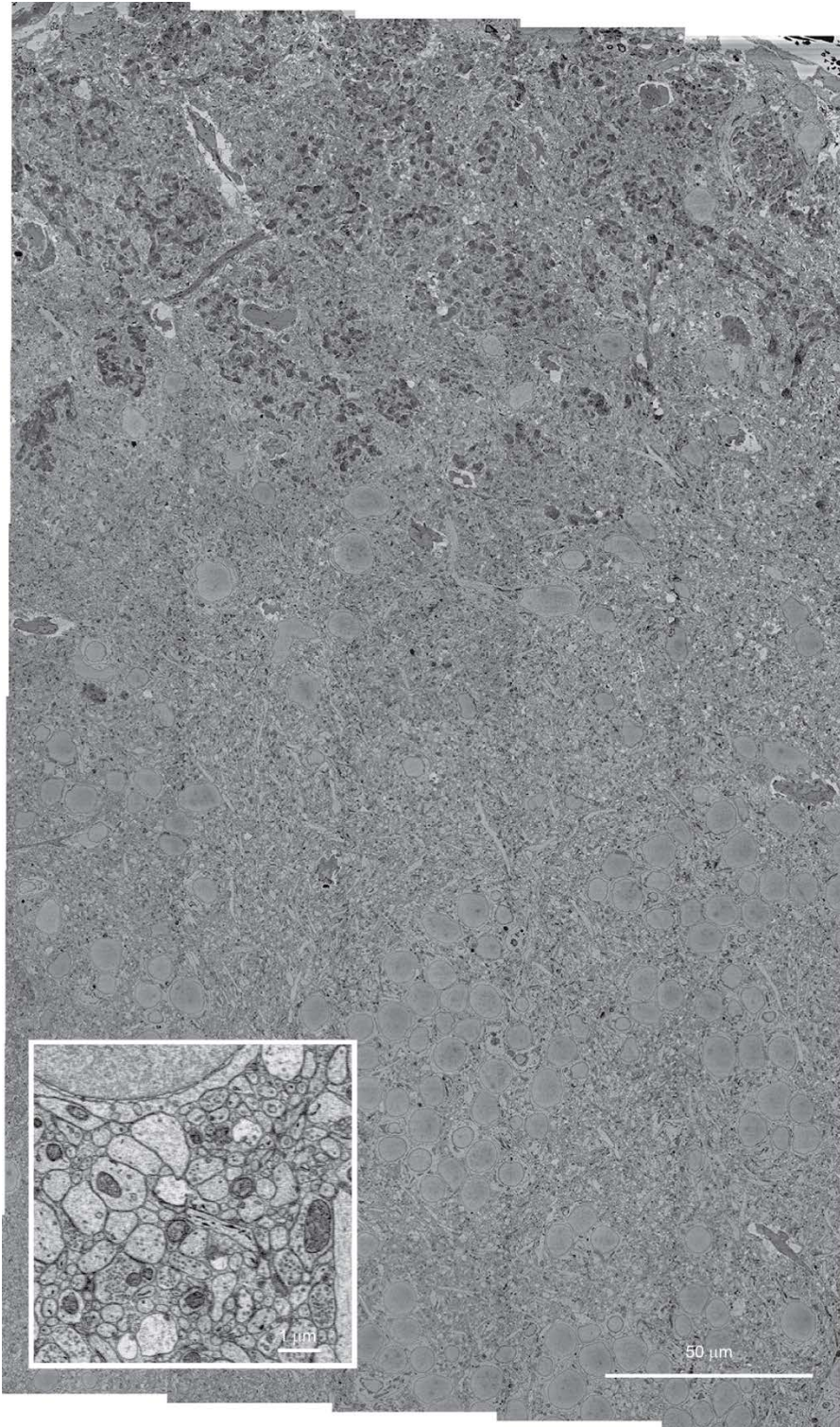
Supplementary Movies 1 – 14

Supplementary Methods: PyKNOSSOS Manual, see Appendix B

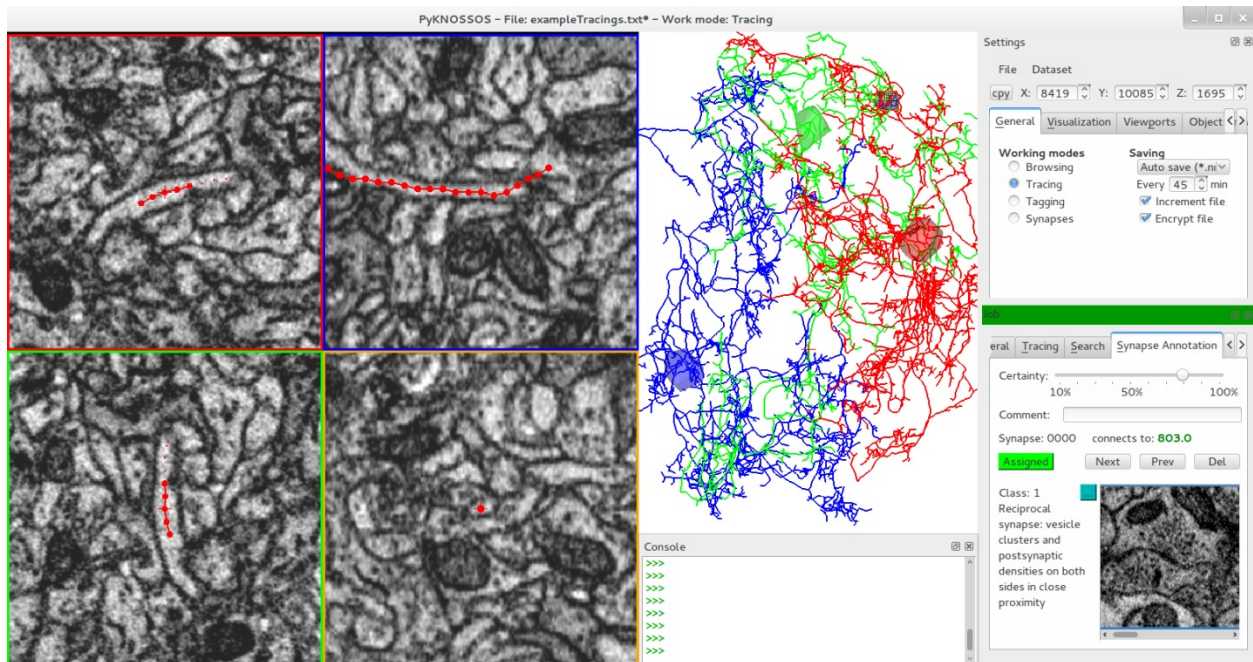


Supplementary Figure 1 SBEM imaging and E/E embedding. (a) Images of the same E/E-embedded sample acquired in high vacuum using a lvSEM (left; $E_L = 1.5$ keV, $D_e = 17$ e⁻/nm) or a vpSEM (right; $E_L = 2$ kV, $D_e = 19$ e⁻/nm). Nominal resolution was 4 nm/pixel. *(b)* Images of the same sample (zebrafish telencephalon) acquired at different rates (0.2 MHz – 2 MHz; $E_L = 1.5$ keV; 4 nm/pixel). Beam current was adjusted to maintain D_e within a narrow range (88 e⁻/nm for 50 pA; 71 e⁻/nm otherwise). *(c)* Images of the same sample (zebrafish telencephalon) acquired at different pressures in a vpSEM and in a lvSEM. HV, high

vacuum. Other imaging parameters were identical ($E_L = 2$ keV; acquisition rate 200 kHz; beam current ca. 60 pA; pixel size 9×9 nm²). Each image is a subregion of the third image in a small stack (50 images; $2,048 \times 2,048$ pixels; 30 nm section thickness) taken in the same field of view. Images were autoscaled and low-pass filtered to attenuate shot noise. (d) Signal-to-noise ratio (SNR) as a function of spatial frequency for images from four different samples acquired at different pressures in a vpSEM and in a lvSEM. Three samples (adult telencephalon, adult OB, larval OB) were embedded in E/E while one sample (larval OB) was embedded in standard EPON (non-EE). For each sample and condition, small stacks of images (usually 50 images; $2,048 \times 2,048$ pixels; 30 nm section thickness) were acquired in the same five regions of interest (ROIs) using fixed parameters ($E_L = 2$ keV; acquisition rate 200 kHz; beam current ca. 60 pA; pixel size 9×9 nm²). Each stack was inspected for regular sectioning and charging artifacts. Regular sectioning without charging artifacts could not be achieved in the non-E/E-embedded sample at pressures <20 Pa. These stacks were therefore excluded from quantitative SNR analysis. To determine the SNR, two-dimensional spatial power spectra were computed, averaged over images and ROIs, collapsed into one dimension by averaging in circular bins, and expressed in dB (10 dB correspond to a factor of 10). Power spectra of noise images (electron beam turned off) were computed using the same procedure and subtracted. The resulting spectra therefore represent the logarithm of the signal power-to-noise power ratio (SNR) as a function of spatial frequency. To compare SNR curves for samples from the same tissue (larval OB), curves for the E/E-embedded sample (Larval OB, E/E) are copied onto the corresponding curves for the non-E/E-embedded sample (Larval OB, non-E/E; right panel) as dashed lines.



Supplementary Figure 2 High-speed SBEM imaging of a large volume. Single image from a large stack acquired at high speed (adult zebrafish OB; E/E-embedding; $E_L = 1.5$ keV; $D_e = 15.9 - 17.3$ e⁻/nm²; 2 MHz; $9 \times 9 \times 25$ nm³ voxels; $173 \times 288 \times 98$ μ m³; 3918 sections; high vacuum; lvSEM). The image consists of 40 tiles, each with 4096 x 4096 pixels. Inset shows zoom-in.



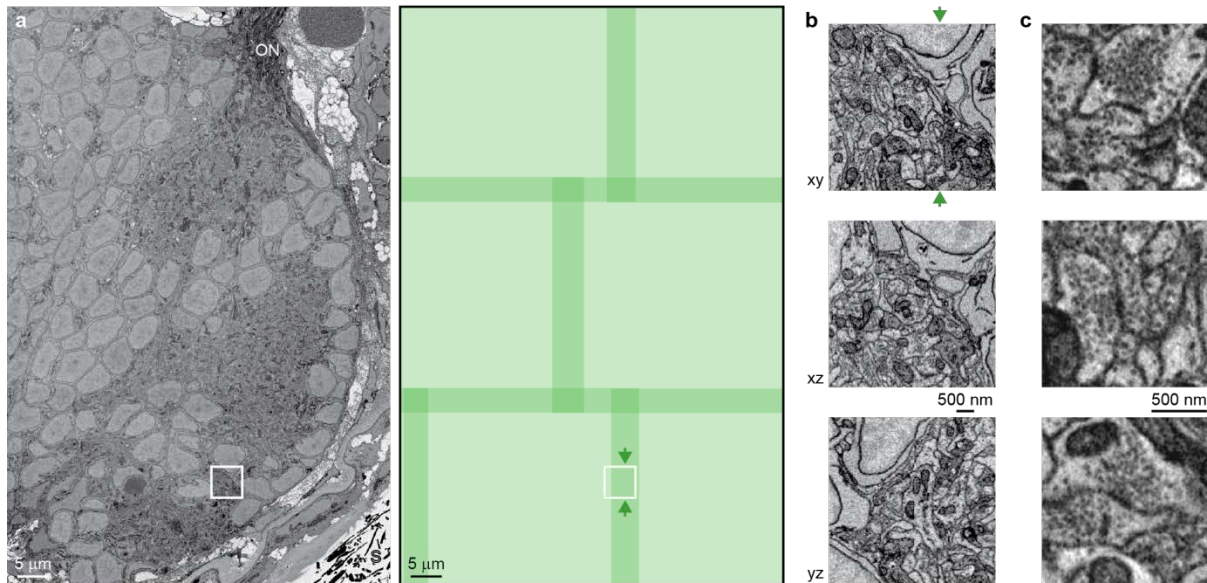
Supplementary Figure 3 PyKNOSSOS. Screenshot of PyKNOSSOS in tracing mode. The four viewports on the left show reslices through the original image stack (here, the upper left shows the x-y plane, the lower right is orthogonal to the traced process shown in red, and the remaining two viewports are orthogonal to the lower right viewport. Other viewport assignments are possible). The fifth viewport shows reconstructions. Zoom levels, translations, rotations, and superimpositions with image data can be adjusted in real time. Panels on the right provide access to different functions for tracing, annotation and visualization (see manual in Supplementary Methods). A tab for synapse annotation is shown on the lower right. Images in the viewports are from the olfactory bulb of a zebrafish larva (4.5 dpf) and were acquired with a vpSEM in high vacuum (EL = 2 keV, De = 17.5 e⁻/nm², 9.25 x 9.25 x 25 nm³ voxels).

Ergonomic software is important to minimize the amount of human labor in circuit reconstruction. We generated a software package for manual skeleton tracing, synapse annotation and visualization with two goals in mind. First, it should be written in a widely used programming language to facilitate modifications and extensions by users. Second, it should allow for the real-time visualization of large and complex reconstructions (hundreds of neurons) together with raw image data. Existing software packages used for neuron reconstruction include KNOSSOS (www.knossostool.org) (Helmstaedter et al. 2011), CATMAID (<http://catmaid.org/>) (Saalfeld et al. 2009), ilastik (www.ilastik.org) (Sommer et al. 2011) and others. KNOSSOS and CATMAID are specifically designed for large-scale reconstruction projects. Inspired by these tools, we created new software that is written in PYTHON and uses the VTK library for 3D visualization (<http://www.vtk.org/>). The software was developed by close interactions between programmer and user and is named PyKNOSSOS because the user interface is closely related to KNOSSOS. A manual with screenshots can be found in Supplementary Methods. Further information is available at www.ariadne-service.ch.

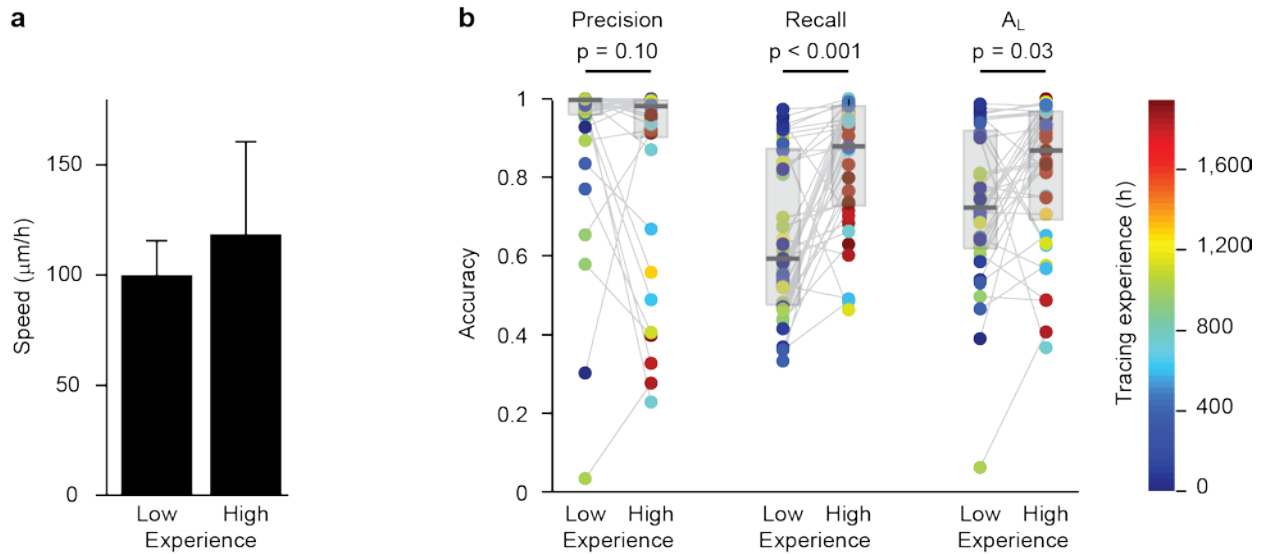
Important features of PyKNOSSOS include the following:

1. *Efficient rendering of reconstructed neurons using VTK.* Using the visualization toolkit (VTK; <http://www.vtk.org/>), PyKNOSSOS can interactively visualize hundreds of reconstructed neurons in 3D on a standard desktop computer together with the underlying image data. This functionality is important for efficient data browsing, tracing and error correction. For higher-level analyses, visualization in PyKNOSSOS can be integrated into custom workflows. Moreover, PyKNOSSOS can be used to generate 3D renderings and animated displays of raw data and reconstructions.
2. *Multi-resolution view.* Like KNOSSOS, PyKNOSSOS dynamically loads cubes of data into RAM as users navigate through a volume. This allows users to browse through large datasets (>1TB) with minimal RAM requirements. Storing multiple sets of cubes at different resolutions allows for seamless zooming through large volumes and the extraction of virtual reslices with arbitrary orientation and zoom-level.
3. *Virtual reslicing of the raw data orthogonal to local processes.* Tracing of neurites and branch point detection should be particularly efficient when users view a section through the EM data volume that is orthogonal to the process being traced. Such virtual reslices should also facilitate the identification of synapses because presynaptic vesicles, the synaptic density, and the postsynapse are contained in the same view. PyKNOSSOS automatically calculates a rotation-minimized “locally orthogonal” section (Wang et al. 2008) during tracing and presents it in a separate viewport, in addition to the cardinal cross-sections and the imaging plane. We found that the “locally orthogonal” view facilitates the detection of branch points and increases tracing speed.
4. *Synapse annotation tools.* PyKNOSSOS includes tools to define the location and direction of a synapse by three successive clicks on the presynaptic process, the synaptic density, and the postsynaptic process. In addition, synapses can be assigned to user-defined classes by a confidence level. Furthermore, pre-calculated “flight paths” can be loaded to automatically visit all branches of a reconstructed neuron. Using this mode, only two clicks on the synaptic density and postsynapse are required to define a synaptic connection. These features, together with the “locally orthogonal” view, facilitate manual synapse annotation. Optionally, each synapse can be assigned to a predefined class and annotated with a confidence level.

Note that some of these functionalities have recently been incorporated also into other software packages.

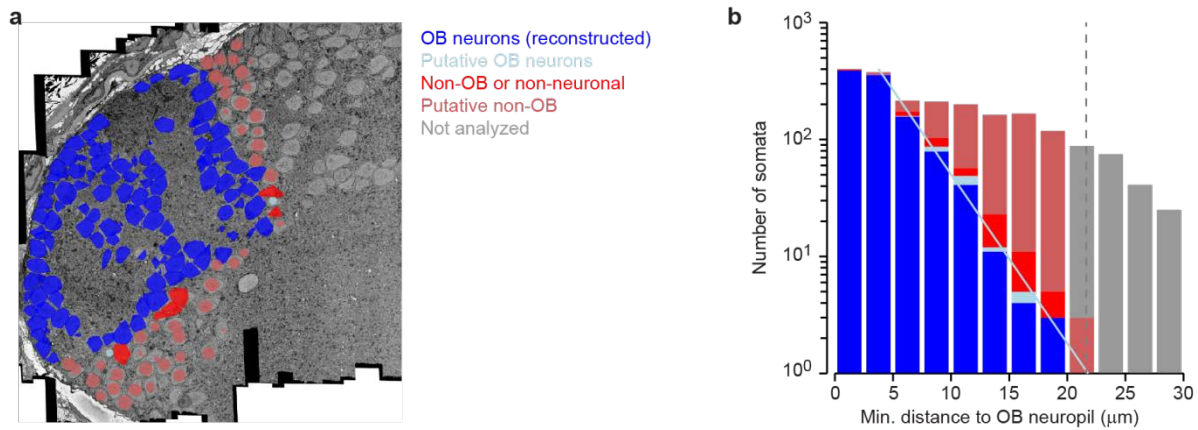


Supplementary Figure 4 EM stack of the larval OB. (a) Image showing cross-section through the entire larval OB ($E_L = 2$ keV, $D_e = 17.5$ e⁻/nm², 9.25 x 9.25 x 25 nm voxels; high vacuum; vpSEM), assembled from multiple tiles (green). Adjacent tiles were combined at the center of the overlapping areas. ON, olfactory nerve; S, silver particles. **(b)** Reslices through a volume of 512 x 512 x 512 voxels in the area outlined by the white square in **(a)**. Green arrows depict the line where two tiles were combined. **(c)** Examples of synapses, including a pair of reciprocal synapses (bottom).



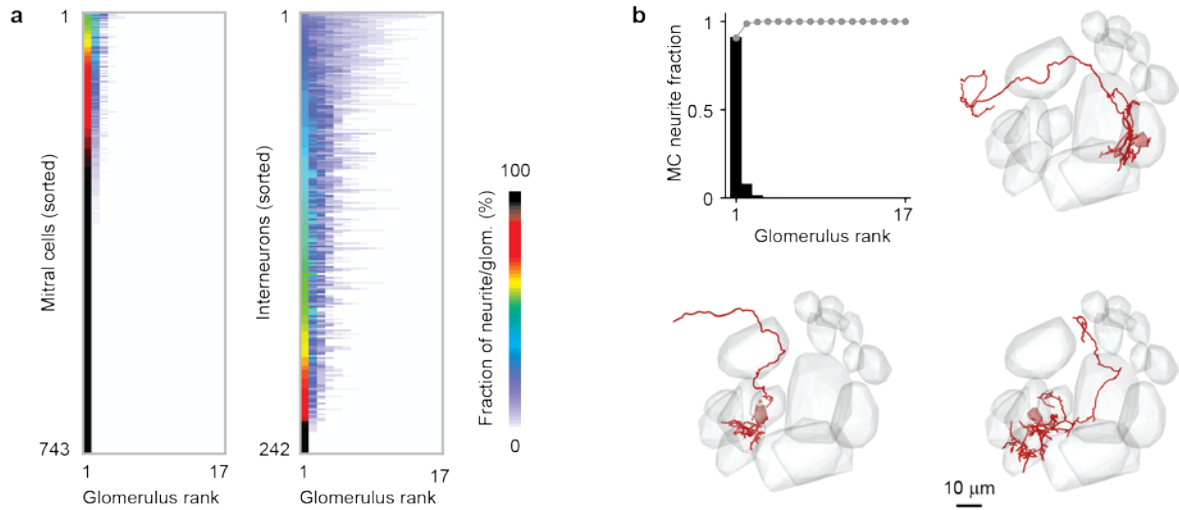
Supplementary Figure 5 Tracing performance as a function of experience. (a) Tracing speed of the same 8 tracers (mean \pm s.d.) at two levels of experience ('low' and 'high'; see below). *(b)* Accuracy of individual tracings, measured by precision, recall and A_L. Each data point quantifies the accuracy of the reconstruction of one neuron by one tracer. Gray lines connect data points representing reconstructions of the same neurons by the same tracers at different levels of experience. Experience of individual tracers is color-coded. Box-plots show median, 25th percentile, and 75th percentile. Statistical comparisons were performed using a Wilcoxon rank-sum test.

To quantify the effect of long-term experience on performance, eight tracers traced a total of 37 neurons within one month using KNOSSOS. The same tracers then traced the same neurons again using KNOSSOS approximately one year later. Between the first and the second tracings, the mean experience of the tracers increased from 412 ± 410 h (mean \pm s.d.) to $1,042 \pm 609$ h. Precision and recall (Figure 7a) of the individual tracings were measured relative to consolidated reconstructions generated by CORE. The average tracing speed increased slightly but not significantly ($p = 0.55$; Wilcoxon rank-sum test) (a). Precision did not change significantly but recall and A_L improved (b). Hence, accuracy increased with long-term experience because recall errors (missed processes) decreased. Note that any interpretation of accuracy measures should consider that tracing speed and accuracy may vary depending on neuronal morphology, sample preparation methods, image quality and tracing instructions (Helmstaedter et al. 2011, Mikula et al. 2015).

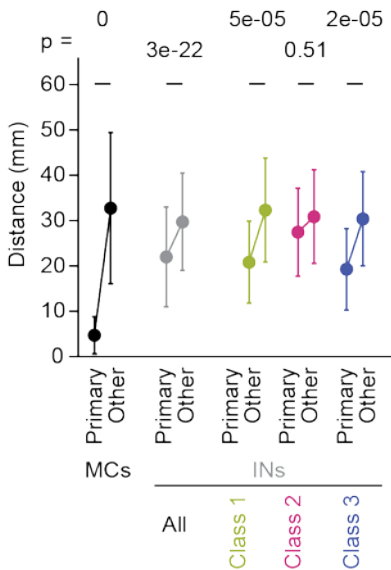


Supplementary Figure 6 Estimation of the number of non-reconstructed OB neurons. (a) Somata near the presumptive caudal boundary of the OB. Colors mark somata of fully reconstructed OB neurons (blue), somata of putative OB neurons (light blue; dendrite directed towards OB), somata of reconstructed cells that do not project into the OB or are not neurons (bright red; non-OB), and somata of putative non-OB cells (pale red; no dendrite towards OB). (b) Number of cells in each class as a function of their minimal distance to an OB neuropil region. Colors as in (a). Light blue line shows an exponential fit to the number of OB neurons as a function of distance. Vertical dashed line shows the distance beyond which no further OB neurons are expected.

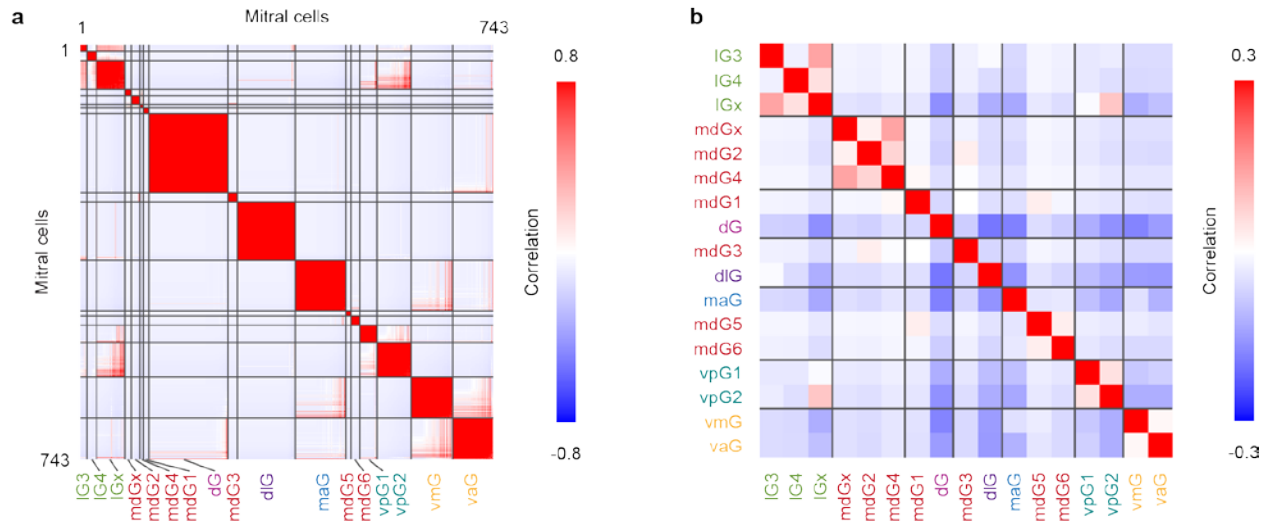
In order to estimate the number of OB neurons not included in the set of 1,096 reconstructed neurons we marked the position of approximately 1,000 additional somata near the presumptive boundary of the OB, determined their distance to the closest neuropil region in the OB, and sorted them into 2.5 μm bins. For all somata up to 20 μm that were not reconstructed before we traced the initial portion of their primary neurite, if any. 24 of these cells were classified as putative OB neurons because they had a primary neurite oriented towards the OB. The number of OB neurons (reconstructed and putative) decreased sharply with increasing distance up to 20 μm (b). An exponential fit predicted that approximately one additional putative OB neuron should be found in subsequent distance bins (≥ 20 μm). We therefore estimate the total number of putative OB neurons that were not included in our reconstructions to be 25.



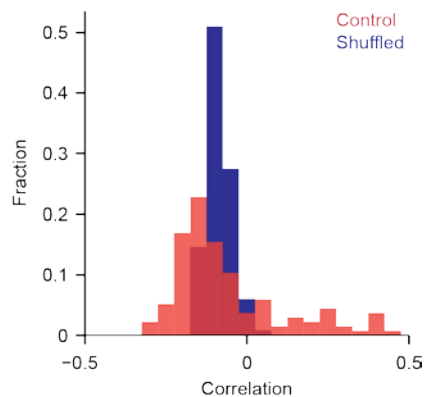
Supplementary Figure 7 Association of mitral cells and interneurons with glomeruli. (a) Left: innervation of glomeruli by mitral cells. For each mitral cell, glomeruli were ranked by decreasing intraglomerular neurite length (axon excluded). Mitral cells were sorted by increasing innervation of the glomerulus with the lowest rank (“parent glomerulus”). Most mitral cells innervate a single glomerulus, and very few mitral cells innervate more than two glomeruli. Right: same plot for interneurons. (b) Mean fraction of mitral cell neurite per glomerulus as a function of glomerulus rank. Gray curve: cumulative distribution of neurite fraction per glomerulus. Images show three examples of mitral cells with dendrites in multiple glomeruli (gray shapes). Note that innervated glomeruli are adjacent to each other.



Supplementary Figure 8 Distance of MCs and INs to glomeruli. Each cell was assigned to a primary glomerulus that contained most of the cell’s intraglomerular processes. Distances (mean \pm s.d.) of somata were measured to the primary glomerulus and to all other glomeruli. Top: p-values of statistical comparisons (Wilcoxon rank-sum test). MC somata were significantly closer to their primary glomerulus than to other glomeruli. A similar, albeit weaker, association between somata and primary glomeruli was observed for IN classes 1 and 3 but not IN class 2.



Supplementary Figure 9 Organization of inter-glomerular MC projections. (a) Correlation matrix showing similarities between glomerular innervation patterns of MCs. MCs were sorted as in Figure 10c: each MC was assigned to a primary glomerulus by its maximum innervation, and MCs assigned to the same glomerulus were ranked by their relative innervation of the glomerulus. Gray lines separate MCs assigned to different primary glomeruli. Because most MCs are associated with a single glomerulus, correlations between projections patterns of MCs assigned to the same glomerulus were very high while correlations across glomeruli were low. (b) Correlation matrix showing similarities between MC innervation patterns of glomeruli, sorted by k-means clustering. Gray lines separate k-means clusters. Color-code of glomerulus labels represents OSN-defined groups (Braubach et al. 2012, Braubach et al. 2013) as in Figure 10a. Correlations between innervation patterns of different glomeruli are low because each MC is typically associated with a single glomerulus.



Supplementary Figure 10 | Shuffling of projections abolishes the correlation structure of glomerular innervation patterns. Red: histogram of pairwise correlations between glomerular IN innervation patterns. Blue: histogram of correlation coefficients after shuffling of relative innervations across glomeruli for each IN (mean over 100 independent shufflings). Shuffling abolishes positive correlations and the distribution of correlation coefficients becomes narrower. Hence, glomerulus-specific patterns of IN innervation in the larval OB (Figure 12b) is inconsistent with random innervation.

Supplementary Movies

Supplementary Movie 1 | SBEM stack of an E/E-embedded sample (telencephalon of adult zebrafish). Pixel size $12 \times 12 \text{ nm}^2$; section thickness 25 nm; acquisition rate 1 MHz; $E_L = 1.5 \text{ keV}$; $D_e = 8.7 \text{ e}^-/\text{nm}^2$; high vacuum; Merlin).

Supplementary Movie 2 | SBEM stack from the adult zebrafish OB (Figure 5f). Each image consisted of 40 tiles, each with 4096×4096 pixels. E/E-embedding; Pixel size $9 \times 9 \text{ nm}^2$; Section thickness 25 nm; acquisition rate 2 MHz; $E_L = 1.5 \text{ keV}$; $D_e = 15.9 - 17.3 \text{ e}^-/\text{nm}^2$; high vacuum; IvSEM). Image resolution has been severely reduced and only a subset of sections is shown to minimize movie size.

Supplementary Movie 3 | Zoom into an image from large SBEM stack (Figure 5f; Supplementary Movie 2). Image consisted of 40 tiles, each with 4096×4096 pixels. Enlarged region contains overlap between adjacent tiles. E/E-embedding; Pixel size $9 \times 9 \text{ nm}^2$; Section thickness 25 nm; acquisition rate 2 MHz; $E_L = 1.5 \text{ keV}$; $D_e = 15.9 - 17.3 \text{ e}^-/\text{nm}^2$; high vacuum; IvSEM). Image quality has been slightly reduced to reduce movie size.

Supplementary Movie 4 | Zoom into an SBEM stack from the larval zebrafish OB (Supplementary Fig. 4). E/E-embedding; Pixel size $9.25 \times 9.25 \text{ nm}^2$; Section thickness 25 nm; acquisition rate 200 kHz; $E_L = 2 \text{ keV}$; $D_e = 17.5 \text{ e}^-/\text{nm}^2$; high vacuum; vpSEM).

Supplementary Movie 5 | Subvolume of SBEM stack from the larval zebrafish OB (Supplementary Fig. 4). E/E-embedding; Pixel size $9.25 \times 9.25 \text{ nm}^2$; Section thickness 25 nm; acquisition rate 200 kHz; $E_L = 2 \text{ keV}$; $D_e = 17.5 \text{ e}^-/\text{nm}^2$; high vacuum; vpSEM). The four quadrants show the four viewports of PyKNOSSOS (red: xy; blue: yz; green: xz; yellow: arbitrary). Arbitrary viewport (yellow) was set to be dorsal up and ventral down, lateral to the right and medial to the left.

Supplementary Movie 6 | Distribution of somata in the OB and adjacent areas. Somata are color-coded as in Supplementary Fig. 6 (blue: reconstructed OB neurons; pale blue spheres: putative OB neurons; red: reconstructed non-OB cells; pale red: putative non-OB cells). Gray: glomeruli. Scale bar: $10 \mu\text{m}$.

Supplementary Movie 7 | 1,022 neurons reconstructed in the OB of a zebrafish larva. Color encodes soma position along dorsoventral axis. Scale bar: $10 \mu\text{m}$.

Supplementary Movie 8 | Large olfactory bulb cells (LOC). Shaded volumes are outlines of glomeruli and color coded according to the relative innervation by the two LOCs (Figure 9g). Scale bars: $10 \mu\text{m}$.

Supplementary Movie 9 | Soma of a LOC. Scale bars (black edges): 2 μm .

Supplementary Movie 10 | Glomeruli of the larval OB. Shaded volumes show glomeruli, color coded according to OSN-defined glomerular groups (Figure 10a). Scale bars (red edges): 20 μm .

Supplementary Movie 11 | Associations between mitral cells and glomeruli. Glomeruli are represented by large shaded volumes. Superimposed are individual mitral cells with neurites innervating three glomeruli. Mitral cell somata are represented by small shaded volumes. Long processes are axons projecting out of the olfactory bulb. Dendrites individual mitral cells are closely associated with single glomeruli. Scale bars: 10 μm .

Supplementary Movie 12 | All mitral cells and their associations with glomeruli. Mitral cells are color-coded according to the OSN-defined group of their parent glomerulus (color code as in Figure 10a). The parent glomerulus is the glomerulus containing the majority of intra-glomerular neurite. Note that somata of mitral cells are superficial and spatially clustered by OSN-defined groups. Scale bar: 10 μm .

Supplementary Movie 13 | Associations between interneurons and glomeruli. Glomeruli are represented by large shaded volumes. Superimposed are individual interneurons with neurites innervating three glomeruli. Somata are represented by small shaded volumes. Neurites of individual interneurons project to multiple glomeruli but do not leave the olfactory bulb. Individual interneurons associated with the same glomerulus show different morphologies. Scale bars: 10 μm .

Supplementary Movie 14 | All INs and their associations with glomeruli. INs are color-coded according to the OSN-defined group of their parent glomerulus (color code as in Figure 10a). The parent glomerulus of is the glomerulus containing the majority of intra-glomerular neurite. Note that most somata of INs are located in deep layers and that spatial clustering is less pronounced than for mitral cells. Scale bar: 10 μm .

Chapter 3 Network topology supports pattern decorrelation in the olfactory bulb

This is a manuscript in preparation.

Adrian A. Wanner^{1,2}, Rainer W. Friedrich^{1,2*}

¹ Friedrich Miescher Institute for Biomedical Research
Maulbeerstrasse 66
4058 Basel
Switzerland

² University of Basel
4003 Basel
Switzerland

* Correspondence:
Dr. Rainer Friedrich
Phone: +41 61 697 8614
Email: Rainer.Friedrich@fmi.ch

3.1 Abstract

In the olfactory bulb (OB) of zebrafish, odors evoke distributed patterns of activity across glomeruli that are reorganized by networks of interneurons (INs). This reorganization results in multiple computations including a decorrelation of activity patterns across the output neurons, the mitral cells (MCs). To understand the mechanistic basis of these computations it is essential to analyze the relationship between function and structure of the underlying circuit. We combined *in vivo* multiphoton calcium imaging with dense circuit reconstruction from serial block-face electron microscopy (SBEM) stacks of the larval zebrafish OB (4.5 dpf). We found that decorrelation of activity patterns elicited by similar odors occurs already at this early larval stage, before the emergence of granule cells. The comparison of inter-glomerular connectivity to the functional interactions between glomeruli indicates that pattern decorrelation is mediated, at least in part, by specific inter-glomerular projections that are mediated by INs, presumably short axon cells (SACs). Modeling results indicate that non-random inter-glomerular interactions observed experimentally are important to decorrelate representations of two natural odor classes, amino acids and bile acids. These results provide strong evidence that the topology of IN networks in the OB determines circuit function, and that the network is optimized, presumably by evolution, to process representations of natural odors.

3.2 Introduction

The decorrelation of odor-encoding neuronal activity patterns is of fundamental importance for information processing in the olfactory bulb (OB) (Friedrich et al. 2014). Odor information is transmitted from the nose to the OB by patterns of activity across the olfactory glomeruli. Glomerular activity patterns representing similar odors are often highly correlated because chemically related odors usually activate overlapping sets of glomeruli. However, as related stimuli can have different meaning, valence and importance, it is important to distinguish between such overlapping input patterns. Moreover, it is assumed that higher brain areas store information in auto-associative memory networks that operate most efficiently when input patterns are distinct from each other (Kohonen 1989, French 1999). It therefore appears useful to decorrelate neuronal activity patterns representing similar odors in order to facilitate their discrimination and memory storage. Measurements of neuronal activity patterns demonstrated that neuronal circuits in the OB indeed perform such a pattern decorrelation (Friedrich et al. 2001, Yaksi et al. 2007, Niessing et al. 2010). Moreover, a recent study reported that pattern decorrelation is directly related to the ability of mice to learn fine odor discriminations (Gschwend et al. 2015). Hence, pattern decorrelation appears to be an important computation involved in odor discrimination and memory.

Because pattern discrimination and pattern classification by recurrent networks is assumed to occur in many brain areas, pattern decorrelation is assumed to be an important computation that is not restricted to the olfactory system. Indeed, pattern decorrelation has also been observed in the dentate gyrus of the hippocampus (Leutgeb et al. 2007, McHugh et al. 2007), a brain area that pre-processes complex, multisensory information for storage and classification in other hippocampal regions such as CA3 (Rolls et al. 2006, Treves et al. 2008). Piriform cortex, one of the main output targets of the OB, is structurally and functionally similar to CA3 and has been proposed to store odor-related information (Hasselmo et al. 1990, Haberly 2001, Wilson et al. 2011), suggesting that pattern decorrelation in the OB and in the dentate gyrus serve similar purposes. However, the underlying mechanisms of pattern decorrelation are still largely unknown.

The processing of odor representations has been studied extensively in zebrafish (Friedrich et al. 1997, Friedrich et al. 1998, Friedrich et al. 2001, Friedrich et al. 2004, Friedrich et al. 2004, Tabor et al. 2004, Li et al. 2005, Yaksi et al. 2006, Mack-Bucher et al. 2007, Yaksi et al. 2007, Tabor et al. 2008, Tabor et al. 2008, Niessing et al. 2010, Wiechert et al. 2010, Blumhagen et al. 2011, Bundschuh et al. 2012, Zhu et al. 2012, Friedrich 2013, Friedrich et al. 2013, Miyasaka et al. 2013, Zhu et al. 2013, Friedrich et al. 2014).

Because the OB of zebrafish is small, odor-evoked activity patterns across large fractions of OB neurons can be recorded by multiphoton calcium imaging. In addition, electrical activity can be measured by extracellular or intracellular recordings, and transgenic lines are available that express fluorescent markers in specific cell types (Friedrich et al. 2010). Natural odors for zebrafish and other aquatic species include bile acids (BAs) and amino acids (AAs), which activate glomeruli in different regions of the OB (Friedrich et al. 1998). Using amino acids as odor stimuli, it was found that the activity of mitral cells (MCs), the major output neurons of the OB, but not glomerular inputs, were decorrelated during the initial phase of an odor response (Friedrich et al. 2001, Niessing et al. 2010). Moreover, when one odor was gradually “morphed” into a similar odor by varying the ratio of components in a binary mixture, MC activity patterns underwent sudden transitions (Niessing et al. 2010). Hence, neuronal circuits in the OB reorganize odor-evoked activity patterns and generate decorrelated, discretized output patterns that are broadcast to multiple higher brain areas (Friedrich 2013). Imaging studies showed that pattern decorrelation involves the inhibition of odor-specific subsets of MCs that are physically clustered (Yaksi et al. 2007). However, the mechanisms underlying pattern decorrelation are not yet understood.

It has been proposed that neuronal circuits in the OB enhance the contrast of odor-evoked activity patterns through short-range lateral inhibition (DeVries et al. 1993, Mori et al. 1994, Yokoi et al. 1995). In the retina, this operation is thought to sharpen visual representations and thereby enhance their discriminability. It is, however, questionable whether a similar mechanism operates in the OB and contributes to pattern decorrelation because there is no simple topographic mapping of olfactory features onto the array of glomeruli (Friedrich et al. 1997, Soucy et al. 2009) and because inhibitory interactions in the OB are likely to be dominated by long-distance interactions (Laurent 1999, Laurent 2002, Wachowiak et al. 2006, Fantana et al. 2008). Other proposed mechanisms such as “non-topographic contrast enhancement” and “activity-dependent gating” use contrast enhancement in a more channel-autonomous way where the decorrelation does not depend on the detailed structure of topology or activity (Cleland et al. 2006, Arevian et al. 2008). Both these mechanisms rely on the reduction of activity of weakly responsive MCs relative to the activity of strongly responsive MCs. In the zebrafish OB, however, strongly responsive MCs often make large positive contributions to pattern correlations, indicating that contrast enhancement mechanisms cannot account for pattern decorrelation. Consistent with this prediction, global dopamine application resulted in contrast-enhancement but failed to decrease correlations between activity patterns (Bundschuh et al. 2012).

Recent theoretical work and simulations suggested a new mechanism called “recurrence-enhanced threshold-induced decorrelation” (reTIDe), in which stochastically connected networks of rectifying elements decorrelate any set of positively correlated, normally distributed input patterns. This mechanism allows for convergent and divergent interactions between neurons and can therefore produce output that takes into account multivariate features of neuronal activity patterns (Wiechert et al. 2010). The initial step is a thresholding of the input, which decreases pattern correlations (Marr 1969, de la Rocha et al. 2007, Wiechert et al. 2010). The feedback architecture injects the thresholded output back into the network, resulting in further decorrelation until a steady state is reached. Pattern decorrelation by reTIDe is particularly pronounced when connectivity is sparse and when the baseline activity of neurons is high, as found in the OB (Wiechert et al. 2010). However, the generic reTIDe mechanism cannot explain the abrupt transitions between discretized activity patterns observed in morphing experiments (Niessing et al. 2010). The generic reTIDe model assumed stochastic connectivity which is unlikely to be true in a biological neuronal circuit such as the OB (Willhite et al. 2006). Conceivably, abrupt transitions could be produced by a refined reTIDe model assuming non-random interactions among subsets of neurons. However, testing this possibility is difficult because it requires exhaustive reconstructions of multisynaptic interactions between distributed sets of neurons.

It is currently also unknown which cell types mediate the interactions between MCs that result in pattern decorrelation. One candidate cell type are granule cells (GCs) which are sparsely connected to MCs and show elevated activity after the MCs activity has reached a steady-state (Isaacson 2001, Willhite et al. 2006, Yaksi et al. 2007). In the adult OB, GCs are a large neuronal population that outnumber MCs by a factor of approximately 15 in zebrafish and >100 in rodents. The OB of larval zebrafish, however, appears to contain few or no GCs (see section 2.3.6), providing an opportunity to test whether decorrelation can occur in the absence of GCs.

Alternatively, or in addition, it is possible that pattern decorrelation involves other types of interneurons. Periglomerular cells are unlikely to mediate the inter-glomerular interactions required for pattern decorrelation because they innervate only one or a small number of neighboring glomeruli. Short axon cells (SACs), in contrast, co-innervate multiple glomeruli, often over long distances. Unlike GCs, SACs are abundant already at larval stages in the zebrafish OB. SACs are morphologically diverse and comprise different subtypes of GABAergic interneurons, including a population that co-expresses dopamine as a second neurotransmitter (see section 2.3.6) (Bundschuh et al. 2012, Zhu et al. 2013). They communicate with MCs and other INs via chemical, often reciprocal synapses (Getchell et al. 1975,

Wanner et al. 2016) and via gap-junctions. Recent findings in the mouse and zebrafish showed that SACs stabilize odor-evoked activity patterns against variations in stimulus intensity (equalization) and, on longer timescales, modulate the contrast of odor-evoked activity patterns (Bundschuh et al. 2012, Zhu et al. 2013, Banerjee et al. 2015). In addition, manipulating the activity of dopaminergic SAC changed correlations between MC activity patterns in mice, indicating that dopaminergic SACs also contribute to pattern decorrelation (Bundschuh et al. 2012, Zhu et al. 2013, Banerjee et al. 2015). While equalization and contrast enhancement do not directly decorrelate input activity patterns, they may support pattern decorrelation. Moreover, SACs could decorrelate representations of defined subsets of odors if they mediate appropriate interactions between specific, non-random subsets of glomeruli. Testing this hypothesis requires not only dense reconstructions of inter-glomerular projections but also measurements of neuronal activity patterns in the same specimen.

First odor responses can be detected in the larval zebrafish OB as early as 2.5 days post fertilization (dpf) (Li et al. 2005, Mack-Bucher et al. 2007). Shortly thereafter, first behavioral responses to odor stimuli have been observed, such as increased swimming speed (Lindsay et al. 2004) and aversive responses (Vitebsky et al. 2005). Between 3 – 5 dpf, the number of different odorant receptors expressed by olfactory receptor neurons increases from ~70 to ~90 (Barth et al. 1996, Byrd et al. 1996, Argo et al. 2003) and the OB starts to respond to a broader spectrum of odors including BAs, AAs, nucleotides and food odor. The activity patterns evoked by these odors are spatially organized in a coarse chemotopic map that already resembles the chemotopic organization of activity patterns in the adult zebrafish OB (Li et al. 2005). For example, AA responses are mainly found in the lateral OB whereas BA responses are mainly found in medial OB. The neuropil in the larval olfactory bulb is organized into spherical structures, so-called glomeruli, which are surrounded by glutamatergic MCs, the major output neurons of the OB. The glomeruli are innervated by distinct types of olfactory sensory neurons (OSNs) and are arranged in a stereotyped pattern that is conserved between individuals. The prototypic organization of the glomerular array is already present at early larval stage and further refined as the circuitry matures (Baier et al. 1994, Sato et al. 2005, Braubach et al. 2012). During this process, the number of glomeruli increases from ~14 in early larvae (4 dpf) to >140 in the adult zebrafish OB.

Using *in vivo* two-photon calcium imaging we recorded neuronal activity in the larval zebrafish OB (4.5 dpf) upon odor stimulation and found that activity patterns evoked by similar odorants are decorrelated. As this computation cannot be explained by a first-order statistical description of the circuit (Friedrich et al. 2014), we analyzed the topology of inter-glomerular projections in more detail by

dense circuit reconstruction. Using 3D serial block-face electron microscopy (SBEM), we acquired a stack of EM images covering the entire OB of a larva in which odor responses were measured previously. We developed novel methods to correlate light microscopy with EM image stacks and established a high-throughput pipeline for neuron reconstruction and synapse annotation. This allowed us to identify individual neurons in both datasets and directly assess the relation between circuit structure and circuit function. In one larval OB we measured odor responses of >60% of all neurons and reconstructed the morphology of 98% of all 1022 OB neurons (Wanner et al. 2016). The comparison of inter-glomerular projection patterns of INs to the functional interactions between glomeruli indicates that pattern decorrelation is mediated, at least in part, by specific inter-glomerular projections of SACs.

3.3 Results

In order to measure odor responses in the larval OB, we performed *in vivo* two-photon calcium imaging in awake but immobilized 4-5 days old, dual transgenic (*elavl3:GCaMP5* x *vglut:DsRed*) zebrafish larvae (Figure 13). After two-photon imaging, the same specimen was chemically fixed and processed for serial block-face scanning electron microscopy (SBEM). After the acquisition of an image stack covering the complete OB and parts of the telencephalon using SBEM, we manually reconstructed the skeletons of all neurons (>1000) in the OB (Wanner et al. 2016). Next we used a custom developed, semi-automated alignment procedure (Figure 14, for a detailed description of the procedure see section 3.5.4) in order to align the EM stack to the light microscopy data. Somata were outlined manually in the 3D EM stack and mapped onto the corresponding structures in the focal planes of the calcium imaging experiments.

3.3.1 Probing IN and MC odor responses in the larval OB

Zebrafish larvae were embedded in low-melting agarose and stimulated successively with different odors while responses of OB neurons were measured as changes in fluorescence (dF/F) by multiphoton microscopy using the fluorescent calcium indicator GCaMP5 (Figure 13d). The odor set comprised a food odor, four bile acids (glycochenodeoxycholic acid [GCDCA], taurocholic acid [TCA], taurodeoxycholic acid [TDCA] and glycocholic acid [GCA]) and four amino acids (Trp, Lys, Phe, and Val). We imaged neuronal activity in six focal planes, each separated by about 10 μm to cover most of the OB and parts of the telencephalon. In each plane, we recorded sessions of 2 min duration with two odor application separated by 1 min, resulting in two trials per recording session. The application of odors induced stereotyped, odor-specific activity patterns in the OB (Figure 13d). Outlines of somata in the EM volume were mapped onto the two-photon focal planes and used as regions of interest (ROIs) to extract dF/F activity traces. The two subsequent trials per recording session were averaged and filtered (see section 3.5.5). The peak response amplitudes of the second odor application were usually slightly lower than in the first trial (Figure 13d).

The reconstructed neurons have previously been classified into cell types according to morphological parameters extracted from the manually traced skeletons (see section 2.3.6). We used this information to analyze cell type specific response properties of MCs and INs. So far, we analyzed all neurons in two multiphoton imaging planes (plane 3 and 4; Figure 15) that could be identified in all trials ($n = 79$ MCs and $n = 37$ INs). In addition, we analyzed neurons that were identified only in a subset of trials due to slow drift. A neuron was considered as responding if the average activity during a post-response onset window was five standard deviations above the baseline activity of the pre-response onset window (see

section 3.5.5 for details). In total, this criterion was fulfilled by 155 MC-odor pairs (“MC responses”) and 245 IN-odor pairs (“IN responses”). The mean amplitude of MC responses was about 50% larger than the mean amplitude of IN responses (Figure 15b). However, individual MCs responded, on average, to fewer odors than INs (Figure 15c). The 25 INs that responded to at least one odor also responded, on average to 2.80 ± 2.58 other odors, whereas the 43 MCs that responded to at least one odor responded on average to only 0.81 ± 1.16 additional odors. The MC population was therefore sparsely active and included many silent or inhibited neurons (Figure 15d).

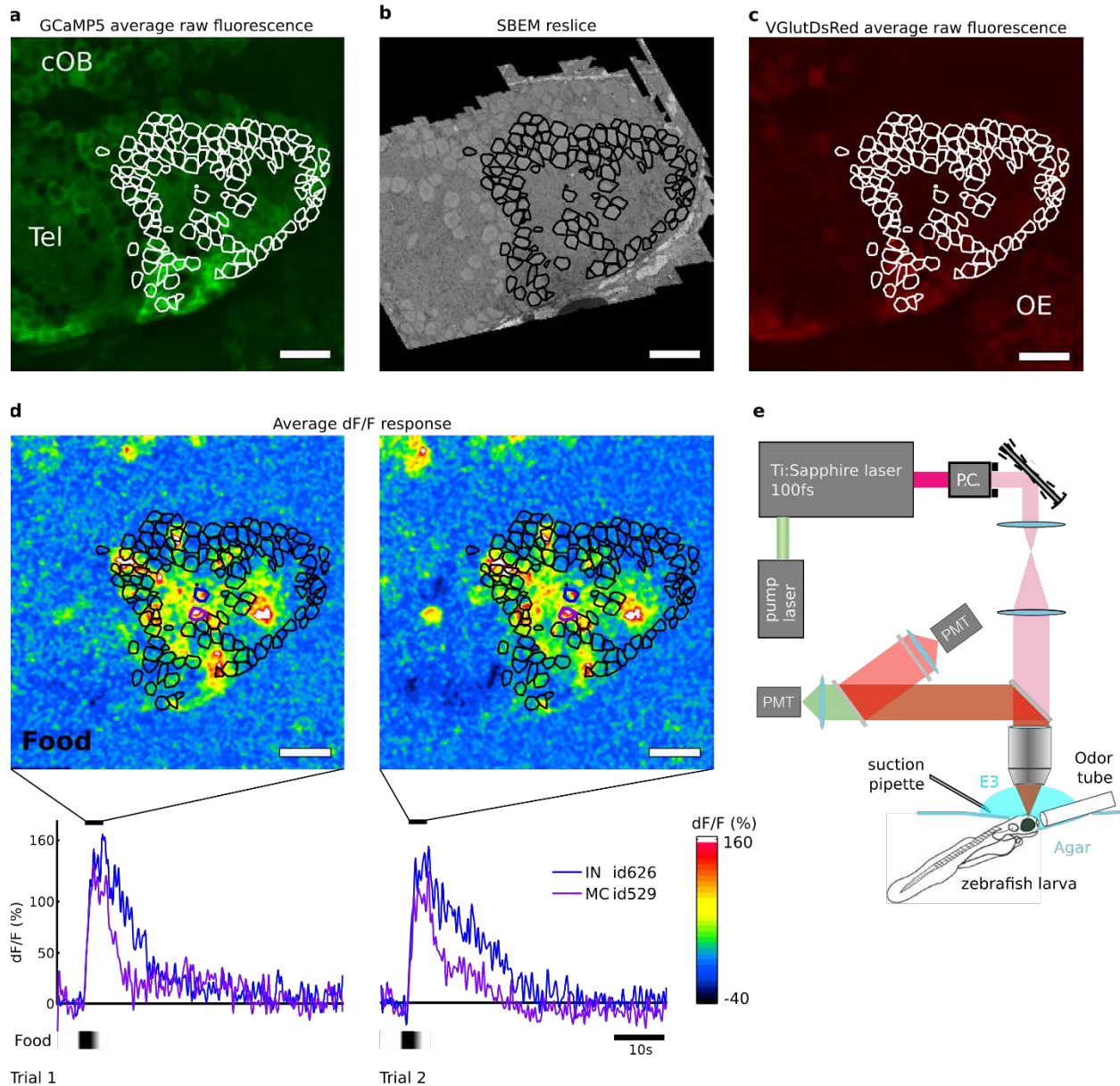


Figure 13 Two-photon calcium imaging (a) Average raw fluorescence of the GCaMP5 signal in imaging plane 4. Outlines of somata in the EM volume were mapped onto the corresponding two-photon focal plane after alignment. These regions of interest (ROIs) were adjusted manually to match soma shapes in the average raw fluorescence images (a, c) and in the average dF/F responses after food odor stimulation (d). (b) SBEM reslice extracted after manual alignment to the two-photon plane. Somata were outlined manually. (c) Average raw fluorescence of the VGlutDsRed signal in the imaging plane 4. VGlutDsRed is expressed in a subpopulation of mitral cells. (d) Change in fluorescence (dF/F) after bath application of food odor in two subsequent trials. Top: Average fluorescence signal (dF/F). Bottom: Individual dF/F traces of an interneuron (blue) and a nearby mitral cell (purple). (e) Schematic of the *in vivo* two-photon calcium imaging experiments. Paralyzed, dual transgenic zebrafish larvae expressing GCaMP5 and VGlutDsRed were embedded in agarose. An odor delivery tube was used for odor application and continuous perfusion with E3. A suction pipette continuously removed any excessive E3. cOB: Contra-lateral olfactory bulb; Tel: telencephalon; OE: olfactory epithelium; PMT: photomultiplier tube; P.C.: Pockels cell. Scale bars: 20 μm .

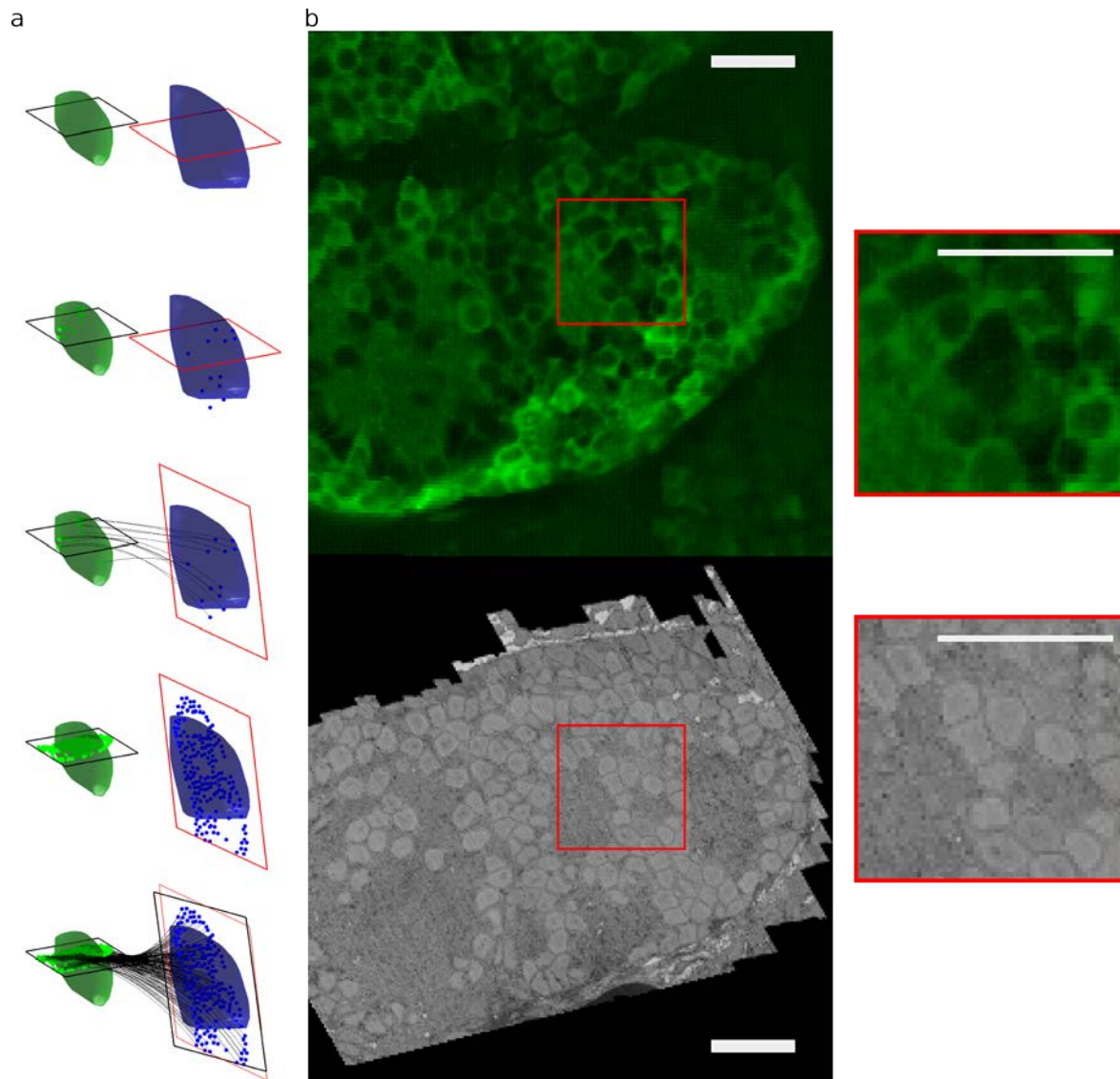


Figure 14 Two-photon to EM correlation. **(a)** Iterative alignment procedure. A focal plane of the two-photon stack (OB outlined in green) and an image plane of the EM stack (OB outlined in blue) are examined next to each other. Corresponding landmarks are marked with points. Next, an affine transform is fitted to the point set and the EM stack is re-oriented to match the new imaging plane. Additional corresponding points are selected and a new affine transform is applied. This procedure is repeated until the corresponding image plane is found. **(b)** Two-photon focal plane 3 (top) and the corresponding EM reslice (bottom) after alignment. Individual somata as well as neuropil regions correspond well across imaging modalities. The red square marks the field of view of the zoomed-in cutout on the right. Scale bar: 20 μm

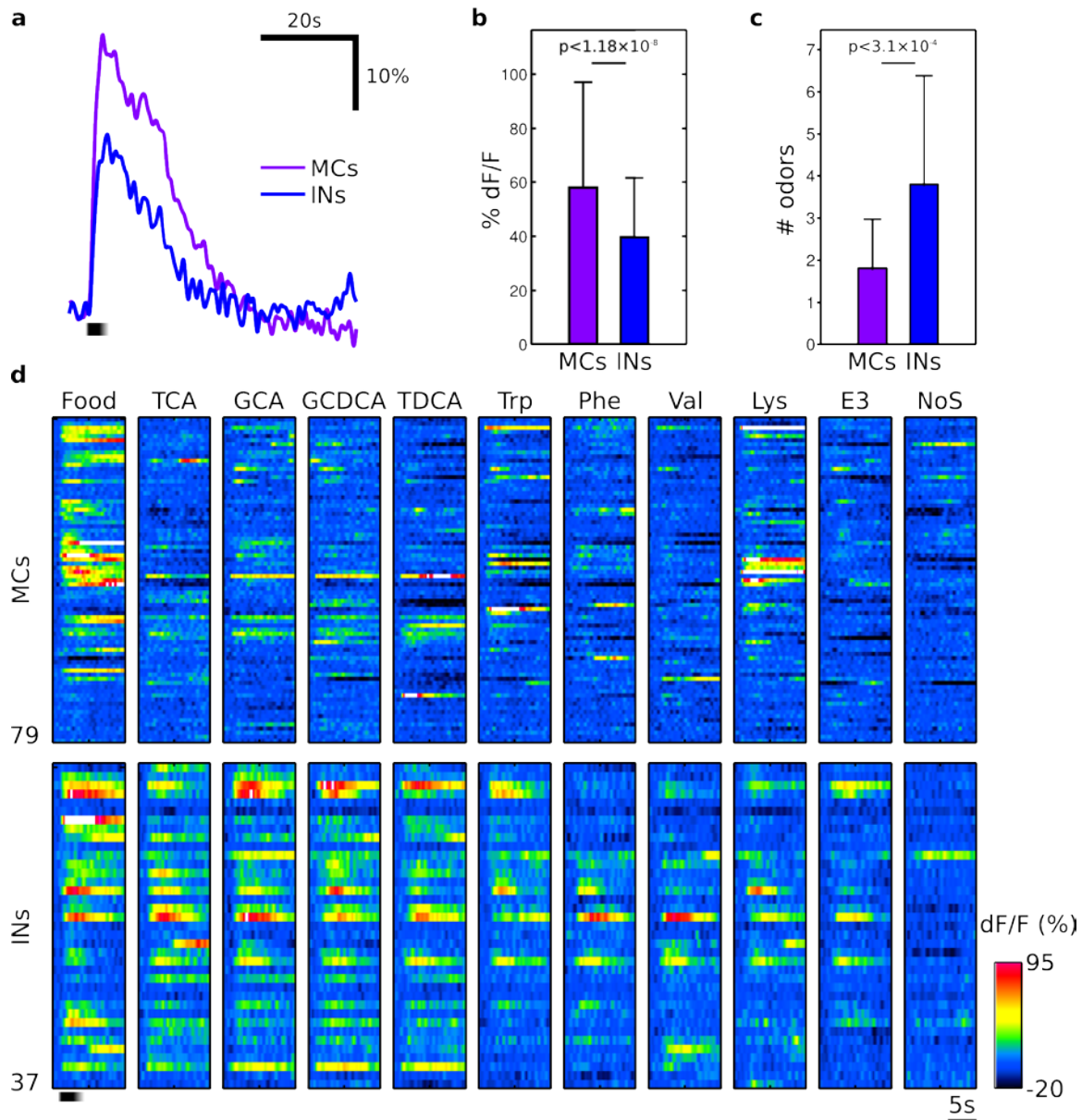


Figure 15 Band-pass filtered dF/F calcium signals pooled from plane 3 and 4. **(a)** Average of 155 MC-odor pairs from 92 MCs (purple line) and 245 IN-odor pairs from 81 INs. Each neuron could contribute a maximum of nine traces if it responded to all odors. Black bar on the bottom left: approximate stimulus time course. **(b)** Average peak amplitude (\pm s.d.) of the traces of responding MCs and responding INs. **(c)** Average number of odors that elicited a MC or IN response. Only neurons that responded to at least one odor were included. **(d)** Population activity of 79 MCs (upper panel) and 37 INs (lower panel) that were present for the complete sequence of odors and controls (E3, no stimulus (NoS)). Black bar on the left: approximate stimulus time course. Statistical comparison: Wilcoxon rank-sum test.

3.3.2 Correlation and decorrelation of activity patterns

In order to analyze the transformation of the activity patterns at higher temporal resolution, we reconstructed firing rate changes from the averaged and filtered dF/F traces by temporal deconvolution (Yaksi et al. 2006). All cells that were present in all sessions of a particular focal plane and that responded to at least one odor stimulus were pooled into a MC population activity matrix (n = 43 MCs) and an IN population activity matrix (n = 25 INs). Population responses to different odors were compared by calculating the Pearson correlation coefficient between the corresponding population activity patterns (Figure 16a). The correlation between representations of BAs and AAs by MCs remained near zero throughout the response, indicating that BAs and AAs activate disjoint sets of MCs. Within the groups of AAs and BAs, however, correlations between MC activity patterns increased shortly after response onset and decreased thereafter within <500 ms. This decorrelation cannot be attributed to an overall decrease of MC activity because the average MC population activity peaked later and remained elevated for >5s (Figure 16b). Hence, MC activity patterns were reorganized and decorrelated during an odor response.

The time course of the population activity pattern was visualized by projecting the responses onto the first three principal components of the population activity (Figure 16c). Trajectories representing MC population responses to similar odors overlapped shortly after response onset but became separated thereafter, consistent with the observed decorrelation. In summary, these results show that decorrelation of MC activity patterns occurs already at early larval stage, despite the fact that GCs arise later in development.

The correlation of IN activity patterns showed different dynamics. Correlations increased more slowly, peaked later, and thereafter decreased only slowly (Figure 16a,b). Moreover, IN population activity patterns were positively correlated across odor classes (AAs and BAs), consistent with the broader tuning of INs. Consequently, the trajectories representing IN activity patterns in principal component space were less well separated and more intermingled than trajectories representing MC activity patterns (Figure 16c).

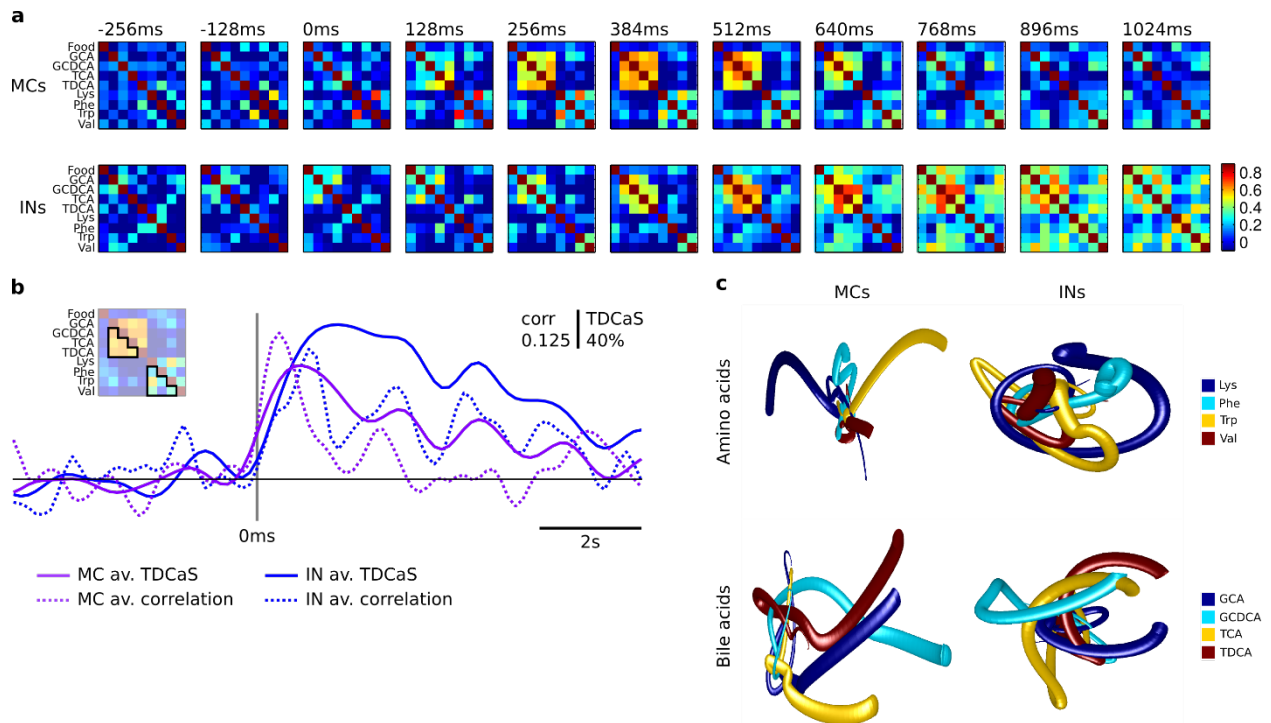


Figure 16 Time-resolved correlation analysis of activity patterns across INs and MCs. (a) Correlations between population activity across MCs (top row) and INs (bottom row) evoked by different odors as a function of time. Correlations between MC activity patterns evoked by odors of the same class (AAs or BAs) increased shortly after response onset ($t=0$) and subsequently decreased to near-baseline levels within <1 s. Correlations between IN activity patterns increased and decreased more slowly. **(b)** Average population activity (solid lines) of INs (blue) and MCs (purple) compared to the average correlation (dashed lines) within BA and AA trials (see inset). The apparent increase in correlation before onset is due to low-pass filtering. Time courses of correlations and mean activity differed between INs and MCs. For both, the mean population activity continued to increase even after the correlation peaked. **(c)** Trajectories of odor-evoked activity patterns 1 s before stimulus onset to 1 s after response onset in the space spanned by the first three principal components. Increasing radius of the trajectory tubes indicates the direction of time.

3.3.3 Transformation of odor information

We next examined whether pattern decorrelation can be observed also when calcium signals are analyzed in glomerular neuropil. The neuropil calcium signal is likely to be dominated by dendritic calcium signals of MCs for two reasons. First, anatomical reconstructions demonstrated that MC dendrites contribute substantially more neurites to glomerular neuropil than interneurons (Wanner et al. 2016). Second, the average calcium signal across the MC population is larger than the average calcium signal across the interneuron population (Figure 15a). Calcium signals from axons of olfactory sensory neurons are usually small and therefore unlikely to contribute substantially to the calcium signal measured in glomeruli (Friedrich et al. 1997). In the six focal planes, we manually outlined all glomeruli that were present throughout all sessions (15 out of 17 glomeruli) and correlated them with the corresponding glomeruli identified in the EM data (see section 2.3.7). From these outlines we extracted glomerular dF/F responses and compared the correlation between these glomerular activity patterns for

different odors within an early (t1) and late (t2) time window after response onset (Figure 17a-e). Similar to MCs, the correlations of glomerular activity patterns were high within the two odor classes (AAs and BAs) but near zero across classes. In addition, correlations between activity patterns evoked by odors of the same class were decreased at t2 although the mean calcium signal was similar (Figure 17e). Hence, pattern decorrelation can be observed at the level of glomerular neuropil responses.

How is this transformation across the glomerular array mediated? MCs are almost exclusively monoglomerular and can therefore not directly account for inter-glomerular interactions (Wanner et al. 2016). INs, in contrast, can have complex, multiglomerular projections, in particular SACs. In order to investigate if inter-glomerular projections of IN can explain the transformation of activity in the glomerular array, we described the functional interactions between glomeruli by a simple linear model (Figure 17d). We selected a subset of glomeruli that showed responses to multiple odors and calculated an interaction matrix that transformed the glomerular activity at t1 into the activity at t2 by the equation:

$$X_{t2} = X_{t1} + WX_{t1} = X_{t1} + (W_{excit} + W_{inhib})X_{t1}$$

In this equation, the matrix X_{t1} represents the set of input patterns. It is assumed that at t1, interactions across glomeruli are negligible because INs are not yet active. Under this simplifying assumption, the observed activity pattern at t1 therefore equals X_{t1} . At t2, it is assumed that the system is in a steady-state. The observed activity pattern is then described by $X_{t1} + WX_{t1}$. This equation represents a linear system with feed-forward inter-glomerular interactions where WX_{t1} describes the input to each glomerulus from all other glomeruli when the external input X_{t1} is present. W is a matrix describing the interactions between glomeruli. W can be expressed as a sum of two interaction matrices, $W_{excit} + W_{inhibit}$, that separately represent excitatory interactions (all entries ≥ 0) and inhibitory interactions (all entries ≤ 0).

As INs are assumed to be GABAergic it may be hypothesized that inhibitory inter-glomerular interactions described by the matrix $W_{inhibit}$ are mediated by inter-glomerular interactions of INs. We therefore compared the structure of $W_{inhibit}$ to the structure of the inter-glomerular projection matrix P obtained by dense circuit reconstruction (Wanner et al. 2016). The projection matrix P is symmetric (non-directional) by definition because it is based on the relative amount of neurite of each IN in each glomerulus, not on the actual synaptic connections. The annotation of synapses on a subset of 7 INs showed that all of these INs made input and output synapses in all innervated glomeruli, often with the

same synaptic partners. Furthermore, the number of synapses per glomerulus was highly correlated with intra-glomerular neurite length. Hence, inter-glomerular projections are likely to be approximated well by the symmetric projection matrix. To facilitate the analysis, we examined the inner product (correlation matrix) of the projection matrix. The symmetry of the projection matrix implies that this approach does not discard information. We focused the analysis on five glomeruli that responded to multiple odors because functional interactions cannot be inferred for non-responsive glomeruli.

We found that the inner product matrices of W_{inhibit} and P were highly correlated to each other ($r = 0.94$; $p < 10^{-4}$; Figure 17g). Hence, inhibitory inter-glomerular interactions inferred from odor-evoked activity patterns can be predicted directly from the pattern of projections between glomeruli. Furthermore, we observed that W_{inhibit} was nearly symmetric, and that elements on the first diagonal were always higher than other elements on the orthogonal diagonals. These observations, derived from functional imaging, are consistent with the anatomical finding that inter-glomerular projections are bidirectional (Wanner et al. 2016). Together, these results provide strong evidence that the reorganization of odor-evoked activity patterns in the OB depends critically on the specific pattern of inter-glomerular IN projections.

While the pattern of inter-glomerular IN projections can explain much of the inhibitory functional interactions between glomeruli described by W_{inhibit} , the anatomical correlate of the excitatory functional interactions described by W_{excit} remains unresolved. Overall, coefficients in W_{excit} were smaller and sparser than coefficients in W_{inhibit} . Unlike W_{inhibit} , W_{excit} was clearly not symmetric, suggesting that interactions via gap junctions (Zhu et al. 2013) are unlikely to account for W_{excit} . Conceivably, the functional excitatory interactions described by W_{excit} could be generated by disinhibitory effects resulting from IN-to-IN interactions or by excitatory INs that have not yet been characterized.

We next asked whether the precise structure of inter-glomerular interactions is important for the decorrelation of activity patterns evoked by AAs and BAs. To address this question, we randomly permuted the coefficients in the interaction matrix W and calculated the resulting output patterns X_{t2} . Pattern decorrelation was assessed by comparing correlations between activity patterns representing odors of the same class between X_{t1} and X_{t2} . Using the original interaction matrix W that exactly reproduces the measured activity patterns, pattern correlations decreased significantly between X_{t1} and X_{t2} . This decorrelation was abolished when W was permuted ($n = 100$ permutations; $p = 0.2$). These results indicate that the decorrelation of activity patterns representing individual AAs and BAs depends on interactions between specific subsets of glomeruli.

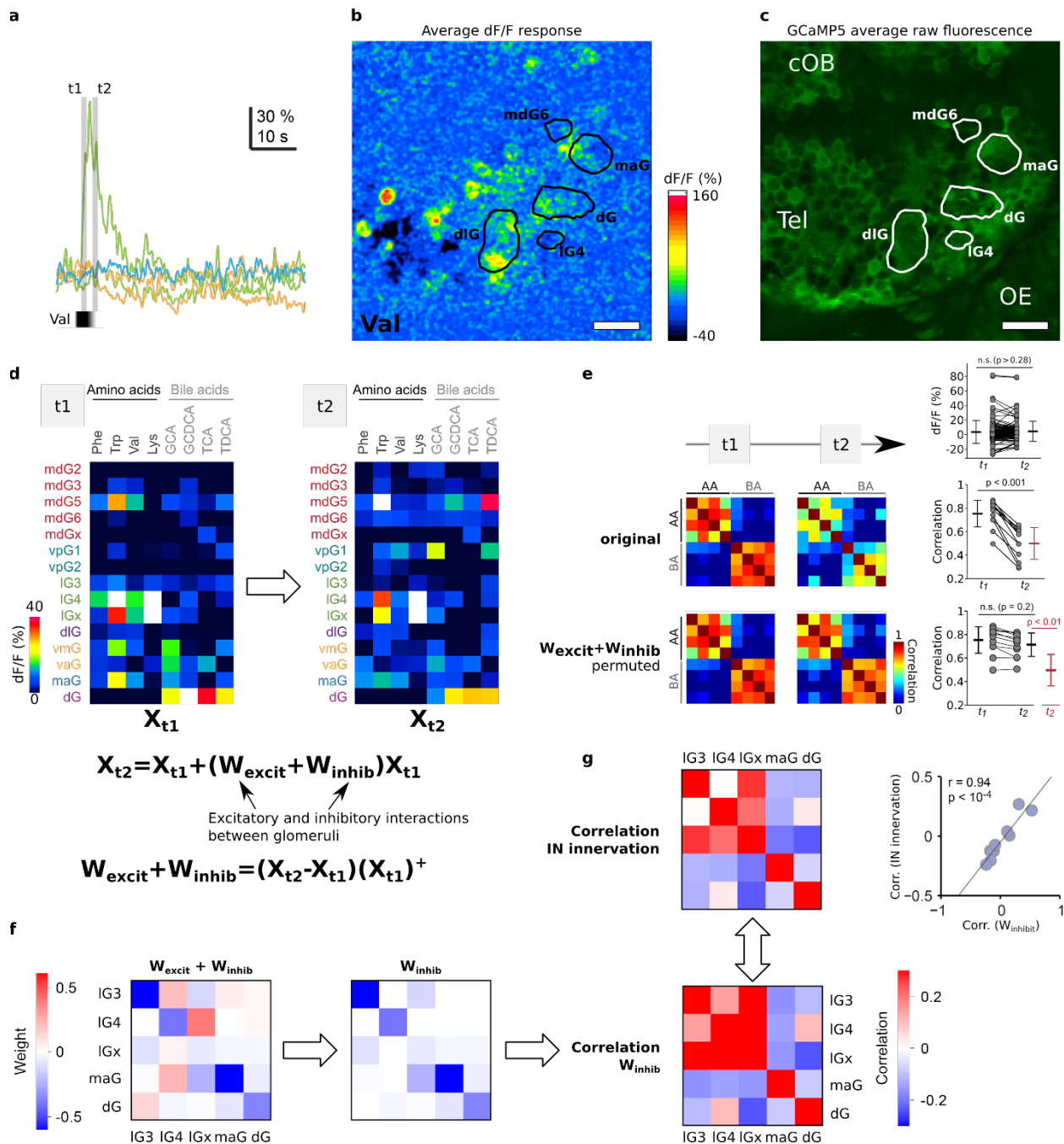


Figure 17 Functional and structural interactions in glomerular activity patterns. (a) Example of glomerular response to odor stimulation with Val (black bar: approximate stimulus time course). t1 and t2 mark the time windows used for the analysis of glomerular activity and correlation. **(b)** Average dF/F responses in two-photon imaging plane 2 upon stimulation with Val. Black outlines indicate different glomerular neuropil regions. **(c)** Average GCaMP5 raw fluorescence of plane 2 with glomerular neuropil outlined and labeled in white. cOB: contra-lateral OB; Tel: telencephalon; OE: olfactory epithelium. Scale bar in (b,c): 20 μ m. **(d)** Glomerular activity patterns X_{t1} and X_{t2} for AA and BA odors at the early time window t1 and the late time window t2, respectively. The equation describes the transformation of glomerular activity pattern X_{t1} into X_{t2} by the interaction matrix $W = (W_{excit} + W_{inhib})$. The interaction matrix is calculated using X_{t1}^+ , the Moore-Penrose pseudoinverse of X_{t1} . The interaction matrix therefore fully determines the transformation of the activity pattern at time t1 into the activity pattern at time t2. **(e)** Top right corner: Average glomerular activity at time t1 and t2. Each pair of data points corresponds to the activity for a glomerulus-odor pair at time t1 and time t2. Middle row, left: Correlation between the measured activity patterns at time t1

and time t_2 . Right: Mean correlation (\pm s.d.) between activity patterns evoked by different amino acids (upper left quadrant) and different bile acids (lower right quadrant). Elements on the diagonal were excluded. Bottom row, left: Activity patterns calculated from the interaction matrix after randomly permuting its columns and rows (mean over 100 random permutations). Right: Mean correlation (\pm s.d.) of X_{t_1} and the activity patterns at t_2 from a permuted interaction matrix, calculated as above. The red inset shows the corresponding correlation values for the original X_{t_2} pattern (shown above). **(f)** The interaction matrix W , calculated from X_{t_1} and X_{t_2} for a subset of five glomeruli that were selected because they responded to multiple odorants. The interaction matrix can be separated into an excitatory interaction matrix W_{excit} with positive weights and an inhibitory interaction matrix W_{inhib} with negative weights. **(g)** Comparison of the correlation matrices representing the functional interactions (bottom) and the IN projection pattern (top left) for the five glomeruli. Top right: Relationship between pair-wise correlation of functional interactions and pair-wise correlations of IN innervation patterns (r : Pearson correlation coefficient). Statistical comparison: Wilcoxon rank-sum test.

3.4 Discussion

One of the most fundamental questions in neuroscience is how the structure of neuronal circuits determines their function. A directly related question is to what extent knowledge about circuit structure can predict circuit function (Lichtman et al. 2008, Seung 2009, Bargmann 2012, Morgan et al. 2013). Although fundamental, these questions remain unresolved for many circuits, largely because the detailed analysis of circuit structure, or connectivity, is still a major challenge. Moreover, because neuronal circuits may vary between individuals, neuronal connectivity and neuronal activity should be examined in the same specimens, which presents additional challenges. In this study, we addressed these problem by combining *in vivo* two-photon calcium imaging and SBEM for the dense reconstruction of activity and connectivity patterns in the larval zebrafish OB. We introduced new tools for light microscopy-to-EM correlation and developed a high-throughput pipeline for neuron reconstruction and synapse annotation. This workflow was successfully used to investigate and compare the relation between structure and function with single neuron resolution in the larval zebrafish OB.

We characterized the response properties of MCs and INs upon odor stimulation and compared the activity patterns elicited by a set of natural odorants. We found that MCs and glomerular activity patterns evoked by similar odors decorrelated with dynamics similar to the adult OB, although the IN network is still premature in the early larval OB. In particular GCs, one of the candidate cell types that were thought to mediate decorrelation in the OB, are still missing in the larval OB. These observations demonstrate that GCs are not necessary for pattern decorrelation. As pattern decorrelation depends on inter-glomerular interactions, this computation most likely involves SACs. These INs are multiglomerular and often innervate complex combinations of glomeruli. Moreover, manipulating the activity of dopaminergic SACs in mice altered the correlations between odor-evoked MC activity patterns (Banerjee et al. 2015).

Although GCs are not strictly required, it is possible that GCs enhance or modulate pattern decorrelation at later developmental stages. GCs appear to emerge gradually during development and continue to be integrated into the OB even during adulthood. Studies in rodents demonstrated that the number and spatial pattern of GC integration in the adult OB is modulated substantially by odor stimulation in a stimulus-specific fashion. These observations give rise to the hypothesis that GCs refine odor processing in the OB depending on an individual's experience. Because these processes act on timescales of days or weeks, it is unlikely that they are involved in the formation of the early neuronal circuitry in the larval OB. We therefore hypothesize that the larval OB represents a "core circuit" that is assembled mainly by

innate mechanisms as a result of evolutionary processes. The subsequent development of GC circuits may then modulate the function of this core circuitry based on experience. Such a system could pre-configure the neuronal circuitry in the OB for broad classes of natural odors and subsequently optimize it in each individual.

The topology of inter-glomerular communication was analyzed by comparing IN innervation patterns obtained by dense reconstruction of neuronal skeletons to functional interactions between glomeruli that were determined by two-photon calcium imaging of odor responses. Remarkably, the IN innervation patterns predicted much of the observed inhibitory inter-glomerular interactions. The relative magnitude of the coefficients in the functional interaction matrix were highly correlated with the corresponding coefficients in the anatomical inter-glomerular projection matrix. Moreover, inhibitory interactions were largely symmetrical, suggesting a reciprocal organization of inter-glomerular interactions. Consistent with this functional observation, most multiglomerular INs do not have distinct “input” and “output” glomeruli but make input and output synapses in each glomerulus with similar ratios, indicating that they mediate non-directional interactions between glomeruli (Wanner et al. 2016). These results provide strong evidence that circuit connectivity is an important determinant of circuit function.

When inter-glomerular interactions were randomized in a simple descriptive model, decorrelation of the original input patterns was abolished. These results indicate that the precise pattern of inter-glomerular interactions is important for pattern decorrelation. These results also indicate that the projections between glomeruli may be optimized to decorrelate representations of specific odors. Stimuli used in our study represented two natural odor classes, AAs and BAs, that are likely to be important odors for a wide range of aquatic species. We therefore hypothesize that the core circuitry of the OB has been shaped by evolution to optimize the representations of common natural odors.

While correlation between inhibitory interactions could be attributed to the IN innervation pattern of glomeruli, we have not yet been able to identify the structural substrate for the excitatory interactions in the functional interaction matrix. So far, no multiglomerular excitatory neuron has been reported in the larval OB. We therefore hypothesize that these excitatory interactions are indirect, either via excitatory feedback from MC target areas in higher order brain regions, or via disinhibitory interactions mediated by INs in the OB.

Our results proof that structural connectivity is indeed capable of predicting and explaining fundamental functional properties of neuronal circuits. However, for disentangling the mechanism underlying the excitatory interactions, additional information on the detailed synaptic connectivity in the larval OB is going to be necessary. Therefore we have started to annotate all synapses between the >1000 reconstructed neurons in order to obtain a complete wiring diagram of the larval OB. Combining the functional data from calcium imaging with the detailed information on synaptic connectivity has the potential to unravel additional, fundamental principles of circuit organization and function.

3.5 Materials and Methods

3.5.1 Animals and preparation

Adult zebrafish (*Danio rerio*) were maintained and bred under standard conditions at 26.5°C. A dual transgenic zebrafish line (elavl3:GCaMP5 x vglut:DsRed) (Kinkhabwala et al. 2011, Akerboom et al. 2012) in nacre background (White et al. 2008) was bred and embryos and larvae were raised at 28.5°C in standard embryo medium E3 (Westerfield 2000). All animal procedures were performed in accordance with official animal care guidelines and approved by the Veterinary Department of the Canton of Basel-Stadt (Switzerland). Imaging experiments were performed as described previously (Li et al. 2005). In brief, 4 - 5 days old larvae were draped in a small drop of E3 and 20 µl of fresh mivacurium chloride (Mivacron, GlaxoSmithKline, Munich, Germany) (Brustein et al. 2003) was added in order to paralyze the larvae. The heart beat and swimming behavior of the larvae was monitored and when the larvae stopped moving (usually within about 30 s to 1 min), the larvae was transferred and embedded in 2% low-melting agarose (type VII; Sigma, St Louis, MO, USA) in a custom-made silicon perfusion chamber. The body axis was inclined by 30° for better optical access to the developing OBs (Figure 13e). Agarose covering the noses was carefully removed. A constant stream (2 mL/min) of E3 was delivered through a tube positioned in front of the nose and removed by continuous suction. Larvae that were not fixed for EM spontaneously recovered from paralysis after a few hours and continued to develop without obvious defects. E3 medium used in this study was always aerated and never contained any methylene blue or N-phenylthiourea.

3.5.2 Odor stimulation

Odor application was performed as described previously (Li et al. 2005). In brief, odors were delivered through a constant stream of E3 directed at the head of the larva using a computer-controlled, pneumatically actuated HPLC injection valve (Rheodyne, Rohnert Park, CA, USA). All experiments were carried out at room temperature (22°C). The odor set comprised one food odor, four bile acids (glycochenodeoxycholic acid [GCDCA], taurocholic acid [TCA], taurodeoxycholic acid [TDCA] and glycocholic acid [GCA]; Sigma Aldrich, Munich, Germany) and four individual amino acids (Trp, Lys, Phe, and Val; Fluka, Neu-Ulm, Germany). Food odor was prepared by incubating 200 mg of commercially available dried fish food (TetraMin or TetraDelica; Tetra Werke, Melle, Germany) in 50 mL of E3 medium for at least 3 h on a shaker at 4°C (Tabor et al. 2004, Li et al. 2005). The suspension was then filtered through filter paper and diluted 1 : 10 in E3. This stock solution was kept refrigerated and diluted 1 : 250

immediately before the experiment. 5×10^{-3} M stock solutions of GCDCA, TCA and TDCA in E3 were kept refrigerated and diluted 1 : 500 immediately before the experiment. 2.5×10^{-3} M stock solutions of GCA in 50% ethanol/50% E3 were kept refrigerated and diluted 1 : 250 immediately before the experiment. 5×10^{-3} M stock solutions of amino acids in E3 were kept refrigerated and diluted 1 : 50 immediately before the experiment. The E3 used for diluting the odors was aerated before the experiment. The E3 used for perfusion was aerated before and throughout the experiment. For each focal plane, each odor was applied twice with a 1 min interval. Successive trials with different odors were separated by at least 2 min to guarantee proper washout of the previous odor.

3.5.3 Multiphoton calcium imaging

Imaging was performed using a custom-built two-photon fluorescence microscope equipped with a mode-locked Ti: sapphire laser (SpectraPhysics) and a 20× objective (NA 1.0, Zeiss) as described (Zhu et al. 2012). GCaMP5 was excited at a wavelength of 910 nm and emission was detected by an external photomultiplier-based whole-field detector through an emission filter (green channel: 535 ± 25 nm; red channel: 610 ± 37.5 nm). Images (256×256 pixels) were acquired at 128 ms per frame using SCANIMAGE and EPHUS software (Pologruto et al. 2003, Suter et al. 2010). For each OB, a total of 5 - 7 focal planes covering the entire larval OB and parts of the nearby telencephalon were acquired. Focal planes were separated by approximately 10 μ m in axial direction.

In each plane we performed a total of ten imaging sessions of 2 min. During each session, an odor was applied twice at an inter-stimulus interval of 1 min. The order of odors in each plane was: Food, E3 (control), food, GCDCA, TCA, TDCA, GCA, Trp, Lys, Phe, Val. In addition, we recorded a 2 min period of spontaneous activity with no stimulus (NoS) after the 10 sessions of odor stimulation. The sessions were separated by at least 2-3 min in order to wash out any remaining odor from previous applications.

3.5.3.1 Automatic drift correction

In the first 1 - 2 hours of acquisition, slow X,Y and Z drifts of the focal plane of up to 50 μ m/hour were regularly observed, probably due capillary forces acting on the agarose matrix (Keller et al. 2011). However, efficient, manual drift correction was difficult because the low raw fluorescence intensity of GCaMP5 provided few obvious landmarks. Increasing laser power in order to increase the two-photon yield was not feasible because high laser intensities may cause photodamage. In order to facilitate drift correction in this low fluorescence and low SNR imaging regime, we developed a custom automated drift correction routine that could be called before each trial. This routine was written in MATLAB and

interacted directly with SCANIMAGE. The routine automatically acquired a small stack of $\pm 3 \mu\text{m}$ in steps of $0.5 \mu\text{m}$ around the current stage position and performed a cross correlation-based comparison of the slices in the stack to a template image of the desired focal plane. The image columns were standardized by subtracting the mean and dividing by the standard deviation of the pixel intensities. The same standardization was subsequently applied to the rows. Translational offsets between the template image and the slices of the stack were calculated by determining the maximum 2D cross-correlation of the standardized images in the Fourier domain. For each slice the normalized cross-correlation to the template plane was calculated considering the previously calculated offsets in X and Y. The target plane was finally selected based on the slice with the largest normalized cross-correlation value and the stage was automatically moved to correct for the corresponding X, Y and Z offsets. Using this procedure the average remaining offsets between subsequent trials were reduced to $-0.03 \pm 0.81 \mu\text{m}$, $0.06 \pm 0.86 \mu\text{m}$ and $0.02 \pm 1.62 \mu\text{m}$, in X, Y and Z, respectively (n = 66 trials).

After the acquisition of all focal planes was completed, a stack of multiphoton fluorescence images covering the whole olfactory bulb with a z-step interval of $0.5 \mu\text{m}$ was recorded for anatomical comparison with the EM stack.

3.5.4 Two-photon to EM correlation

Although the two-photon dataset and EM dataset have been recorded from the same specimen, they do not necessarily contain the same anatomical information. We considered four possible sources for distortions and disagreement between the two-photon stack and the EM volume:

- 1) Mechanical damage and distortions caused by the small craniotomy which was made after two-photon imaging above the contralateral olfactory bulb to facilitate the penetration of fixative and EM reagents into the brain.
- 2) Volume loss of up to 30% due to loss of extracellular space induced by chemical fixation (Korogod et al. 2015).
- 3) Different orientation of the sample in the two-photon microscope and the SBEM.
- 4) Developmental changes due to migrating and dividing cells.

Although we cannot rule out that developmental changes happen during the about 3 hours between the recording of the first two-photon trial and the final chemical fixation, we could not find any clear evidence for disagreement between the two stacks that would indicate developmental causes. While orientation differences (3) can easily be corrected by linear transformations (rotation and translation),

distortions (1, 2) can potentially be highly nonlinear and could be difficult to correct for. It is therefore crucial to avoid these types of distortions, as well as damage during sample preparation.

Maintaining the same orientation of the sample orientation in light microscopy and EM imaging is not feasible because the samples are completely opaque after E/E embedding. As a consequence, the orientation of the sample prior to the start of EM imaging is poorly predictable. Significant post-acquisition alignment was therefore required. In order to correlate the two-photon microscopy data with the corresponding EM volume we developed an iterative alignment procedure in MATLAB. Corresponding points were selected manually in both datasets (Figure 14a). Subsequently, an affine transform was fitted to the pairs of corresponding points. The fitted affine transformation matrix was used to transform the EM volume towards the orientation of the two-photon stack. Consequently, the new, transformed orientation of the EM volume was closer to the orientation of the two-photon stack. Next, additional pairs of corresponding points were selected or the position of existing pairs of corresponding points was optimized in order to further re-fine the transform. The displacement distances between the position of the projected corresponding points and the manually placed points was used to assess the quality of the alignment between the two datasets. For plane 3 and plane 4, the average displacement distances were $1.53 \pm 0.83 \mu\text{m}$ and $1.03 \pm 0.53 \mu\text{m}$, respectively. Large values for the displacement distances would indicate, that either the corresponding points were not carefully chosen or that the underlying true distortion transform is highly non-linear and therefore cannot be well approximated by a simple linear transform.

3.5.5 Reconstruction of somatic firing rate changes

After the successful two-photon to EM-correlation we mapped the manually drawn outlines of somata from the EM dataset onto the two-photon focal planes (Figure 14). These somata have been classified into INs and MCs based on morphological features of the reconstructed skeletons (see section 2.3.6). The outlines were used as regions of interest (ROIs) to extract somatic calcium signals. The exact position of each ROI was manually adapted for each trial.

In order to calculate the raw somatic fluorescence signal for each ROI, the pixels of the raw fluorescence frames were first low-pass filtered with a mild spatial 2D Gaussian kernel ($\sigma = 1.2 \text{ px}$) and then averaged over all pixels in each ROI. Subsequently, the baseline was determined for each ROI by taking the average fluorescence over a 2 sec window before response onset (frames 9 - 25 and 479 - 495 for the first and the second odor applications, respectively). Only somata that were represented by a minimum number of 15 pixels (corresponding to a ROI area of $3.75 \mu\text{m}^2$) were included in the analysis of activity

patterns (Figure 15, Figure 16). The dF/F traces from the two odor applications were averaged and band-pass filtered with a Butterworth filter with a cutoff frequency of 0.2 times the frame rate. In order to identify responding cells, the average population response onset ($t = 0$ ms) was determined manually from the raw dF/F traces and was set to frame 42. The mean μ_{pre} and standard deviation σ_{pre} of the band-pass filtered dF/F activity was determined in a pre-response onset window (frames 9 - 40). A cell was classified as responding if the mean μ_{post} of the band-pass filtered dF/F signal in the post-response onset window (frames 48 - 100) was $\mu_{\text{post}} > \mu_{\text{pre}} + 5 \times \sigma_{\text{pre}}$. The averaged and band-pass filtered dF/F traces were used to reconstruct firing rate changes for each ROI by temporal deconvolution as described ($\tau_{\text{decay}} = 3$ s, $\text{thr}_{\text{noise}} = 0$) (Yaksi et al. 2006).

3.5.6 Population activity and correlation

The temporally deconvolved calcium signals (TDCaS) of all cells from all aligned planes were pooled into population activity vectors for each odor stimulus. To avoid any spurious effects of responses to E3, the carrier medium of the odor, the analysis was restricted to the response space orthogonal to the E3 responses. The correlation analysis was restricted to cells that were present in all trials and responded to at least one odor stimulus. In total, 33 MCs and 18 INs of plane 3 and 10 MCs and 7 INs of plane 4 were included in the correlation analysis (Figure 16). Population responses to different odors were compared by calculating the Pearson correlation coefficient between the population activity vectors of MCs and INs for the different stimuli at a given time point after response onset (Figure 16a). The mean population activity of INs and MCs across all trials was compared to the average correlation within BA and AA trials (Figure 16b).

Trajectories of band-passed dF/F population activity of INs and MCs were visualized in principal component space for both, BA and AA trials, separately (Figure 16c). The principal components were extracted from a concatenated activity matrix with cells in rows and trials and time bins in columns. Principal components form an orthogonal basis in the parameter space of the underlying data in which the basis vectors are sorted according to decreasing variance of the original data. To visualize the trajectories for different odors, the activity matrix was projected onto the first three principal components.

3.5.7 Glomerular activity and structure to function relationship

After two-photon to EM correlation (see section 3.5.4), the shapes of glomeruli outlined in the EM stack were mapped onto the aligned two-photon stack. These coarse outlines were used as a reference for

manually drawing glomerular contours in the GCaMP5 raw fluorescence images using custom software written in IgorPro (Wavemetrics) (Figure 17b,c). For these glomerular ROIs we calculated dF/F traces as described before. The activity of glomeruli that were present in more than one focal plane was averaged. The correlation between glomerular dF/F activity patterns for different odors was compared between an early (t_1 = frames 51-54) and a late (t_2 = frames 77-86) time window after response onset (Figure 17b). A simple linear model with an interaction matrix W can be used to describe the transformation of the input activity pattern X_{t_1} at time t_1 to glomerular activity pattern X_{t_2} at time t_2 :

$$X_{t_2} = X_{t_1} + WX_{t_1}$$

The model assumes that

1. Interactions across glomeruli are negligible at t_1 because INs are not yet active. In this case, the glomerular activity pattern at t_1 is equal to X_{t_1} .
2. The system reached a steady-state at t_2 .

Under these conditions, the model describes a linear system with feed-forward inter-glomerular interactions. These interactions are captured by the interaction matrix W that can be calculated from $X_{t_1}^+$, the Moore-Penrose pseudoinverse of X_{t_1} :

$$W = (X_{t_2} - X_{t_1})X_{t_1}^+$$

The interaction matrix can be separated into an excitatory interaction matrix W_{excit} with positive weights and an inhibitory interaction matrix W_{inhib} with negative weights:

$$W = W_{excit} + W_{inhibit}$$

The interaction matrix describes the transformation of the activity patterns of different odors from time t_1 to time t_2 , which resulted in a decorrelation of the glomerular activity patterns (Figure 17e). A randomized interaction matrix W_p was obtained by random permutations of rows and columns of the interaction matrix. If W_p is used to predict the glomerular activity at t_2 we get:

$$X_2^p = X_{t_1} + W_p X_{t_1}$$

In contrast to the original interaction matrix, where we found a significant difference in correlations between X_{t_1} and X_{t_2} ($p < 10^{-3}$, Wilcoxon rank-sum test), no significant correlation difference can be observed between X_{t_1} and $X_{t_2}^p$ ($n=100$ permutations; $p=0.2$, Wilcoxon rank-sum test). This indicates that

the decorrelation of activity patterns representing individual AAs and BAs depends on the specific structure of W , i.e. on interactions between specific subsets of glomeruli.

A subset of glomeruli (IG3, IG4, IGx, maG, dG) that responded to multiple odors was selected to investigate the structure of the inhibitory interaction matrix (Figure 17f). To compare the inhibitory interactions between glomeruli, the columns and rows of the inhibitory interaction matrix were correlated with each other (Figure 17g). The resulting functional interaction correlation matrix shows remarkable similarity and is highly correlated (Pearson correlation coefficient for matrix elements: $r = 0.94$, $p < 10^{-4}$) to the structural interaction correlation matrix calculated from the correlation between IN innervation patterns of different glomeruli (see section 2.3.7).

Chapter 4 Discussion and outlook

Higher order brain functions emerge from the interaction of few hundreds to hundreds of thousands of neurons. These neurons form interconnected neuronal circuits in which information is transmitted and transformed via chemical and electrical signaling pathways. The process, in which an individual neuron transforms input into output activity is determined by the biophysical properties of the neuron. On larger scale however, where hundreds of neurons interact with each other, it is mainly the structural, synaptic connectivity that determines circuit function. Detailed information on circuit structure is therefore of fundamental importance for a mechanistic description of circuit function.

In this thesis I developed a complete, generic workflow for measuring the activity of hundreds of neurons simultaneously and obtaining detailed information on the underlying circuit structure thereafter. This workflow comprises *in vivo* multiphoton calcium imaging of neuronal activity, the acquisition of large 3D electron microscopy stacks at ultra-resolution using the emerging technology of serial block-face electron microscopy (SBEM) and subsequent high-throughput reconstruction of neuronal morphology and synaptic connectivity. I developed novel embedding and staining procedures that effectively reduced surface charging in SBEM and enabled the acquisition with at least a ten-fold increase in both, signal-to-noise as well as acquisition speed. A professional high-throughput image annotation service, ariadne-service gmbh, was established for high quality reconstruction of neuronal circuits that is now available to the scientific community. I developed novel heuristic algorithms, procedures and software for efficient redundant skeleton tracing, synapse annotation and alignment and correlation of light microscopy and EM image stacks.

This workflow was used for measuring the activity of hundreds of neurons upon odor stimulation in the olfactory bulb (OB) of larval zebrafish and subsequent reconstruction of all neurons (>1000) in a complete SBEM stack of the OB. The morphological analysis of the complete library of the neuronal repertoire of the larval OB revealed new, rare cell types such as atypical projection neurons and large olfactory bulb cells. We found that ~75% of all neurons in the larval OB were mitral cells (MCs), whereas interneurons (INs) were a minority. In contrast to MCs, that were almost exclusively monoglomerular, many INs had extensive neurites innervating multiple glomeruli. These INs represent specific subtypes of INs including periglomerular and short axon-like cells while the large granule cell population develops later. From this we concluded that the IN network of the OB develops sequentially in zebrafish. The MC : IN ratio and the morphology of the two largest IN classes of the larval zebrafish OB are reminiscent of the antennal lobe of insects (Stocker et al. 1990, Chou et al. 2010). On a subset of MCs and INs I

annotated all synapses and found that INs did not have any specific input or output glomeruli, implying that inter-glomerular interactions have a strong non-directional component. These findings suggest that INs mediate scaling operations similar to normalization in the antenna lobe (Olsen et al. 2010, Zhu et al. 2013) and equalization in the adult zebrafish OB (Olsen et al. 2010, Zhu et al. 2013). Although projections of INs were widespread and complex, subsets of INs preferentially innervated specific groups of glomeruli that receive input from the same types of olfactory sensory neurons. This indicates that inter-glomerular projections are organized by glomerular identity.

The analysis of neuronal calcium signals revealed that activity patterns of MCs and glomeruli evoked by similar odors decorrelate with dynamics similar to the adult OB. We analyzed the topology of the functional glomerular interactions and found by the help of a simple linear model that the specific structure of these interactions is non-random and necessary for mediating decorrelation. The comparison of these functional interaction patterns to the IN innervation pattern of glomeruli revealed remarkable similarities. The correlation between IN innervation patterns of glomeruli could predict >94% of the correlation between the inhibitory part of the interactions patterns of glomeruli.

The introduced workflow for studying network activity and connectivity at single neuron resolution has unraveled elementary organizational and functional principles in the larval OB of zebrafish, which could not have been discovered with sparse sampling of network activity or connectivity. It is, to our knowledge, the first completely skeletonized brain area of that size. The analysis of the glomerular network revealed a fundamental relationship between circuit structure and function. The detailed synaptic connectivity of this network is likely to unravel further major principles of how circuit architecture determines circuit function. Therefore we recently started to annotate all synapses between the >1020 reconstructed neurons and will soon obtain the complete connectome of the larval zebrafish OB. The comparison of the detailed synaptic connectivity and the odor specificity of the OB neurons is likely to provide further, fundamental insight into how the circuit structure sculpts neuronal dynamics and define circuit function in the OB.

However, this workflow is not specific to the OB of zebrafish larva but could also, in principle, be applied to any other neuronal circuit of similar size and accessibility. I am confident that this and similar workflows for circuit reconstruction will have a tremendous impact on the understanding of computations in neuronal circuits. At the moment, these techniques are still very resource and time intensive. Therefore further optimization and automatization of both acquisition and analysis is necessary. For example, in order to move similar data acquisition and reconstruction efforts in to the

realm of the feasible in mammalian cortex, the acquisition speed in 3D EM has to be increased by about two orders of magnitudes and the performance of semi-automated reconstruction pipelines has to improve by about three orders of magnitudes. However, there is light on the horizon of circuit neuroscience. New imaging techniques such as volumetric multiphoton imaging and light-sheet imaging can now be used to measure the activity of large populations of thousands of neurons, such as brain-wide activity at single neuron resolution in zebrafish larva (Keller et al. 2008, Botcherby et al. 2012, Ahrens et al. 2013, Yang et al. 2016). New, improved staining procedures can produce homogeneously stained, high contrasted samples with $>1 \text{ mm}^3$ volume (Mikula et al. 2012, Hua et al. 2015, Mikula et al. 2015). ZEISS launched recently the multiSEM 505/506 that scan the surface or sections of large EM samples with 61 - 91 parallel electron beams simultaneously which increase the field of view and the acquisition speed tremendously (Eberle et al. 2015). Last but not least, recent progress in the design of deep-learning networks promise a quantum leap in the automated segmentation and reconstruction of neurons (LeCun et al. 2015, Schmidhuber 2015).

While all these techniques still have their caveats, they will certainly leverage the throughput in the reconstruction of neuronal circuits. This will allow neuroscientists not only to investigate the topology of larger circuits, but also to analyze circuit structure and function more quantitatively in multiple samples in order to study inter-individual variability in circuit architecture, the development of circuit structure as well as disease related abnormalities in circuit connectivity.

References

- Ahrens, M. B., J. M. Li, M. B. Orger, D. N. Robson, A. F. Schier, F. Engert and R. Portugues (2012). "Brain-wide neuronal dynamics during motor adaptation in zebrafish." *Nature* **485**(7399): 471-477.
- Ahrens, M. B., M. B. Orger, D. N. Robson, J. M. Li and P. J. Keller (2013). "Whole-brain functional imaging at cellular resolution using light-sheet microscopy." *Nat Methods* **10**(5): 413-420.
- Akerboom, J., T. W. Chen, T. J. Wardill, L. Tian, J. S. Marvin, S. Mutlu, N. C. Calderon, F. Esposti, B. G. Borghuis, X. R. Sun, A. Gordus, M. B. Orger, R. Portugues, F. Engert, J. J. Macklin, A. Filosa, A. Aggarwal, R. A. Kerr, R. Takagi, S. Kracun, E. Shigetomi, B. S. Khakh, H. Baier, L. Lagnado, S. S. Wang, C. I. Bargmann, B. E. Kimmel, V. Jayaraman, K. Svoboda, D. S. Kim, E. R. Schreiter and L. L. Looger (2012). "Optimization of a GCaMP calcium indicator for neural activity imaging." *J Neurosci* **32**(40): 13819-13840.
- Arevian, A. C., V. Kapoor and N. N. Urban (2008). "Activity-dependent gating of lateral inhibition in the mouse olfactory bulb." *Nat Neurosci* **11**(1): 80-87.
- Argo, S., F. Weth and S. I. Korsching (2003). "Analysis of penetrance and expressivity during ontogenesis supports a stochastic choice of zebrafish odorant receptors from predetermined groups of receptor genes." *Eur J Neurosci* **17**(4): 833-843.
- Axel, R. (1995). "The molecular logic of smell." *Sci. Am.* **273**: 130-137.
- Baier, H. and S. Korsching (1994). "Olfactory glomeruli in the zebrafish olfactory system form an invariant pattern and are identifiable across animals." *J. Neurosci.* **14**: 219-230.
- Bakkum, D. J., U. Frey, M. Radivojevic, T. L. Russell, J. Muller, M. Fiscella, H. Takahashi and A. Hierlemann (2013). "Tracking axonal action potential propagation on a high-density microelectrode array across hundreds of sites." *Nat Commun* **4**: 2181.
- Bancroft, J. D. and M. Gamble (2008). *Theory and practice of histological techniques*, Elsevier Health Sciences.
- Banerjee, A., F. Marbach, F. Anselmi, M. S. Koh, M. B. Davis, P. Garcia da Silva, K. Delevich, H. K. Oyibo, P. Gupta, B. Li and D. F. Albeanu (2015). "An Interglomerular Circuit Gates Glomerular Output and Implements Gain Control in the Mouse Olfactory Bulb." *Neuron* **87**(1): 193-207.
- Bargmann, C. I. (2012). "Beyond the connectome: how neuromodulators shape neural circuits." *Bioessays* **34**(6): 458-465.
- Barth, A. L., N. J. Justice and J. Ngai (1996). "Asynchronous onset of odorant receptor expression in the developing zebrafish olfactory system." *Neuron* **16**(1): 23-34.
- Bazaes, A. and O. Schmachtenberg (2012). "Odorant tuning of olfactory crypt cells from juvenile and adult rainbow trout." *J Exp Biol* **215**(Pt 10): 1740-1748.

Berning, M., K. M. Boergens and M. Helmstaedter (2015). "SegEM: Efficient Image Analysis for High-Resolution Connectomics." Neuron **87**(6): 1193-1206.

Blumhagen, F., P. Zhu, J. Shum, Y. P. Scharer, E. Yaksi, K. Deisseroth and R. W. Friedrich (2011). "Neuronal filtering of multiplexed odour representations." Nature **479**(7374): 493-498.

Bock, D. D., W. C. Lee, A. M. Kerlin, M. L. Andermann, G. Hood, A. W. Wetzel, S. Yurgenson, E. R. Soucy, H. S. Kim and R. C. Reid (2011). "Network anatomy and in vivo physiology of visual cortical neurons." Nature **471**(7337): 177-182.

Boergens, K. M. and W. Denk (2013). "Controlling FIB-SBEM slice thickness by monitoring the transmitted ion beam." J Microsc **252**(3): 258-262.

Botcherby, E. J., C. W. Smith, M. M. Kohl, D. Debarre, M. J. Booth, R. Juskaitis, O. Paulsen and T. Wilson (2012). "Aberration-free three-dimensional multiphoton imaging of neuronal activity at kHz rates." Proc Natl Acad Sci U S A **109**(8): 2919-2924.

Braitenberg, V. and A. Schüz (1998). Cortex: statistics and geometry of neuronal connectivity. Berlin, Springer.

Braubach, O. R., A. Fine and R. P. Croll (2012). "Distribution and functional organization of glomeruli in the olfactory bulbs of zebrafish (*Danio rerio*)." J Comp Neuro **520**(11): 2317-2339.

Braubach, O. R., N. Miyasaka, T. Koide, Y. Yoshihara, R. P. Croll and A. Fine (2013). "Experience-dependent versus experience-independent postembryonic development of distinct groups of zebrafish olfactory glomeruli." J Neurosci **33**(16): 6905-6916.

Briggman, K. L. and D. D. Bock (2012). "Volume electron microscopy for neuronal circuit reconstruction." Curr Opin Neurobiol **22**(1): 154-161.

Briggman, K. L., M. Helmstaedter and W. Denk (2011). "Wiring specificity in the direction-selectivity circuit of the retina." Nature **471**(7337): 183-188.

Brustein, E., N. Marandi, Y. Kovalchuk, P. Drapeau and A. Konnerth (2003). ""In vivo" monitoring of neuronal network activity in zebrafish by two-photon Ca(2+) imaging." Pflugers Arch **446**(6): 766-773.

Buck, L. B. (2000). "The molecular architecture of odor and pheromone sensing in mammals." Cell **100**(6): 611-618.

Bundschuh, S. T., P. Zhu, Y. P. Scharer and R. W. Friedrich (2012). "Dopaminergic modulation of mitral cells and odor responses in the zebrafish olfactory bulb." J Neurosci **32**(20): 6830-6840.

Byrd, C. A., J. T. Jones, J. M. Quattro, M. E. Rogers, P. C. Brunjes and R. G. Vogt (1996). "Ontogeny of odorant receptor gene expression in zebrafish, *Danio rerio*." J Neurobiol **29**(4): 445-458.

Carandini, M. and D. J. Heeger (2012). "Normalization as a canonical neural computation." Nat Rev Neurosci **13**(1): 51-62.

Cardona, A., S. Saalfeld, J. Schindelin, I. Arganda-Carreras, S. Preibisch, M. Longair, P. Tomancak, V. Hartenstein and R. J. Douglas (2012). "TrakEM2 software for neural circuit reconstruction." PLoS One **7**(6): e38011.

Chklovskii, D. B., S. Vitaladevuni and L. K. Scheffer (2010). "Semi-automated reconstruction of neural circuits using electron microscopy." Curr Opin Neurobiol **20**(5): 667-675.

Chou, Y. H., M. L. Spletter, E. Yaksi, J. C. Leong, R. I. Wilson and L. Luo (2010). "Diversity and wiring variability of olfactory local interneurons in the Drosophila antennal lobe." Nat Neurosci **13**(4): 439-449.

Cleland, T. A. and P. Sethupathy (2006). "Non-topographical contrast enhancement in the olfactory bulb." BMC Neurosci **7**: 7.

Cuntz, H., F. Forstner, A. Borst and M. Hausser (2010). "One rule to grow them all: a general theory of neuronal branching and its practical application." PLoS Comput Biol **6**(8).

de la Rocha, J., B. Doiron, E. Shea-Brown, K. Josic and A. Reyes (2007). "Correlation between neural spike trains increases with firing rate." Nature **448**(7155): 802-806.

Deerinck, T. J., E. A. Bushong, V. Lev-Ram, X. Shu, R. Y. Tsien and M. H. Ellisman (2010). "Enhancing serial block-face scanning electron microscopy to enable high resolution 3D nanohistology of cells and tissues." Microsc. Microanal. **16**: 1138-1139.

Deisseroth, K. and M. J. Schnitzer (2013). "Engineering approaches to illuminating brain structure and dynamics." Neuron **80**(3): 568-577.

Del Bene, F. and C. Wyart (2012). "Optogenetics: a new enlightenment age for zebrafish neurobiology." Dev Neurobiol **72**(3): 404-414.

Denk, W., K. L. Briggman and M. Helmstaedter (2012). "Structural neurobiology: missing link to a mechanistic understanding of neural computation." Nat Rev Neurosci **13**(5): 351-358.

Denk, W. and H. Horstmann (2004). "Serial block-face scanning electron microscopy to reconstruct three-dimensional tissue nanostructure." PLoS Biol **2**(11): e329.

Denk, W., J. H. Strickler and W. W. Webb (1990). "Two-photon laser scanning fluorescence microscopy." Science **248**(4951): 73-76.

Denk, W. and K. Svoboda (1997). "Photon upmanship: why multiphoton imaging is more than a gimmick." Neuron **18**(3): 351-357.

DeVries, S. H. and D. A. Baylor (1993). "Synaptic circuitry of the retina and olfactory bulb." Cell **72** **Suppl**: 139-149.

Doving, K. B., K. A. Hansson, T. Backstrom and H. Hamdani el (2011). "Visualizing a set of olfactory sensory neurons responding to a bile salt." J Exp Biol **214**(Pt 1): 80-87.

- Doving, K. B. and S. Lastein (2009). "The alarm reaction in fishes--odorants, modulations of responses, neural pathways." Ann N Y Acad Sci **1170**: 413-423.
- Dynes, J. L. and J. Ngai (1998). "Pathfinding of olfactory neuron axons to stereotyped glomerular targets revealed by dynamic imaging in living zebrafish embryos." Neuron **20**(6): 1081-1091.
- Eberle, A. L., S. Mikula, R. Schalek, J. Lichtman, M. L. Tate and D. Zeidler (2015). "High-resolution, high-throughput imaging with a multibeam scanning electron microscope." J Microsc **259**(2): 114-120.
- Edwards, J. G. and W. C. Michel (2002). "Odor-stimulated glutamatergic neurotransmission in the zebrafish olfactory bulb." J Comp Neurol **454**(3): 294-309.
- Egerton, R. F., P. Li and M. Malac (2004). "Radiation damage in the TEM and SEM." Micron **35**(6): 399-409.
- Eyre, M. D., M. Antal and Z. Nusser (2008). "Distinct deep short-axon cell subtypes of the main olfactory bulb provide novel intrabulbar and extrabulbar GABAergic connections." J Neurosci **28**(33): 8217-8229.
- Fantana, A. L., E. R. Soucy and M. Meister (2008). "Rat olfactory bulb mitral cells receive sparse glomerular inputs." Neuron **59**(5): 802-814.
- Firestein, S. (2001). "How the olfactory system makes sense of scents." Nature **413**(6852): 211-218.
- French, R. M. (1999). "Catastrophic forgetting in connectionist networks." Trends Cogn Sci **3**(4): 128-135.
- Friedrich, R. W. (2013). "Information processing in the olfactory system of zebrafish." Annu. Rev. Neurosci. **36**: 383-402.
- Friedrich, R. W., C. Genoud and A. A. Wanner (2013). "Analyzing the structure and function of neuronal circuits in zebrafish." Front Neural Circuits **7**: 71.
- Friedrich, R. W., C. J. Habermann and G. Laurent (2004). "Multiplexing using synchrony in the zebrafish olfactory bulb." Nat Neurosci **7**(8): 862-871.
- Friedrich, R. W., G. A. Jacobson and P. Zhu (2010). "Circuit neuroscience in zebrafish." Curr Biol **20**(8): R371-381.
- Friedrich, R. W. and S. I. Korsching (1997). "Combinatorial and chemotopic odorant coding in the zebrafish olfactory bulb visualized by optical imaging." Neuron **18**: 737-752.
- Friedrich, R. W. and S. I. Korsching (1998). "Chemotopic, combinatorial, and noncombinatorial odorant representations in the olfactory bulb revealed using a voltage-sensitive axon tracer." J Neurosci **18**(23): 9977-9988.
- Friedrich, R. W. and G. Laurent (2001). "Dynamic optimization of odor representations by slow temporal patterning of mitral cell activity." Science **291**(5505): 889-894.

Friedrich, R. W. and G. Laurent (2004). "Dynamics of olfactory bulb input and output activity during odor stimulation in zebrafish." J Neurophysiol **91**(6): 2658-2669.

Friedrich, R. W. and M. T. Wiechert (2014). "Neuronal circuits and computations: pattern decorrelation in the olfactory bulb." FEBS Lett **588**(15): 2504-2513.

Fuller, C. L. and C. A. Byrd (2005). "Ruffed cells identified in the adult zebrafish olfactory bulb." Neurosci Lett **379**(3): 190-194.

Fuller, C. L., H. K. Yettaw and C. A. Byrd (2006). "Mitral cells in the olfactory bulb of adult zebrafish (*Danio rerio*): Morphology and distribution." J. Comp. Neurol. **499**(2): 218-230.

Fuss, S. H. and S. I. Korsching (2001). "Odorant feature detection: activity mapping of structure response relationships in the zebrafish olfactory bulb." J Neurosci **21**(21): 8396-8407.

Getchell, T. V. and G. M. Shepherd (1975). "Short-axon cells in the olfactory bulb: dendrodendritic synaptic interactions." J Physiol **251**(2): 523-548.

Gschwend, O., N. M. Abraham, S. Lagier, F. Begnaud, I. Rodriguez and A. Carleton (2015). "Neuronal pattern separation in the olfactory bulb improves odor discrimination learning." Nat Neurosci **18**(10): 1474-1482.

Haberly, L. B. (2001). "Parallel-distributed processing in olfactory cortex: new insights from morphological and physiological analysis of neuronal circuitry." Chem Senses **26**(5): 551-576.

Hamdani el, H. and K. B. Doving (2007). "The functional organization of the fish olfactory system." Prog Neurobiol **82**(2): 80-86.

Hamdani el, H., S. Lastein, F. Gregersen and K. B. Doving (2008). "Seasonal variations in olfactory sensory neurons--fish sensitivity to sex pheromones explained?" Chem Senses **33**(2): 119-123.

Hansen, A. and T. E. Finger (2000). "Phyletic distribution of crypt-type olfactory receptor neurons in fishes." Brain Behav Evol **55**(2): 100-110.

Hansen, A., S. H. Rolen, K. Anderson, Y. Morita, J. Caprio and T. E. Finger (2003). "Correlation between olfactory receptor cell type and function in the channel catfish." J Neurosci **23**(28): 9328-9339.

Hansen, A. and B. S. Zielinski (2005). "Diversity in the olfactory epithelium of bony fishes: development, lamellar arrangement, sensory neuron cell types and transduction components." J Neurocytol **34**(3-5): 183-208.

Harris, K. M., E. Perry, J. Bourne, M. Feinberg, L. Ostroff and J. Hurlburt (2006). "Uniform serial sectioning for transmission electron microscopy." J Neurosci **26**(47): 12101-12103.

Hasselmo, M. E., M. A. Wilson, B. P. Anderson and J. M. Bower (1990). "Associative memory function in piriform (olfactory) cortex: computational modeling and neuropharmacology." Cold Spring Harb Symp Quant Biol **55**: 599-610.

- Hayworth, K. J., N. Kasthuri, R. Schalek and J. W. Lichtman (2006). "Automating the collection of ultrathin serial sections for large volume TEM reconstructions." Microsc Microanal **12**: 86-87.
- Hayworth, K. J., J. L. Morgan, R. Schalek, D. R. Berger, D. G. Hildebrand and J. W. Lichtman (2014). "Imaging ATUM ultrathin section libraries with WaferMapper: a multi-scale approach to EM reconstruction of neural circuits." Front Neural Circuits **8**: 68.
- Helmchen, F. and A. Konnerth (2011). Imaging in Neuroscience: A Laboratory Manual, Cold Spring Harbor Laboratory Press.
- Helmstaedter, M. (2013). "Cellular-resolution connectomics: challenges of dense neural circuit reconstruction." Nat Methods **10**(6): 501-507.
- Helmstaedter, M., K. L. Briggman and W. Denk (2011). "High-accuracy neurite reconstruction for high-throughput neuroanatomy." Nat Neurosci **14**(8): 1081-1088.
- Helmstaedter, M., K. L. Briggman, S. C. Turaga, V. Jain, H. S. Seung and W. Denk (2013). "Connectomic reconstruction of the inner plexiform layer in the mouse retina." Nature **500**(7461): 168-174.
- Hill, A., C. V. Howard, U. Strahle and A. Cossins (2003). "Neurodevelopmental defects in zebrafish (*Danio rerio*) at environmentally relevant dioxin (TCDD) concentrations." Toxicol Sci **76**(2): 392-399.
- Hinsch, K. and G. K. Zupanc (2007). "Generation and long-term persistence of new neurons in the adult zebrafish brain: a quantitative analysis." Neuroscience **146**(2): 679-696.
- Hodgkin, A. L., A. F. Huxley and B. Katz (1952). "Measurement of current-voltage relations in the membrane of the giant axon of *Loligo*." J Physiol **116**(4): 424-448.
- Hua, Y., P. Laserstein and M. Helmstaedter (2015). "Large-volume en-bloc staining for electron microscopy-based connectomics." Nat Commun **6**: 7923.
- Hubel, D. H. and T. N. Wiesel (1962). "Receptive fields, binocular interaction and functional architecture in the cat's visual cortex." J Physiol **160**: 106-154.
- Hussain, A., L. R. Saraiva and S. I. Korsching (2009). "Positive Darwinian selection and the birth of an olfactory receptor clade in teleosts." Proc Natl Acad Sci U S A **106**(11): 4313-4318.
- Isaacson, J. S. (2001). "Mechanisms governing dendritic gamma-aminobutyric acid (GABA) release in the rat olfactory bulb." Proc Natl Acad Sci U S A **98**(1): 337-342.
- Jain, V., Murray, J.F., Roth, F., Turaga, S., Zhigulin, V., Briggman, K.L., Helmstaedter, M.N., Denk, W., Seung, H.S. (2007). "Supervised learning of image restoration with convolutional networks." IEEE 11th International Conference on Computer Vision: 1-8.
- Kaynig, V., B. Fischer, E. Muller and J. M. Buhmann (2010). "Fully automatic stitching and distortion correction of transmission electron microscope images." J Struct Biol **171**(2): 163-173.

- Keller, P. J., A. D. Schmidt, J. Wittbrodt and E. H. Stelzer (2008). "Reconstruction of zebrafish early embryonic development by scanned light sheet microscopy." Science **322**(5904): 1065-1069.
- Keller, P. J., A. D. Schmidt, J. Wittbrodt and E. H. Stelzer (2011). "Digital scanned laser light-sheet fluorescence microscopy (DSLM) of zebrafish and Drosophila embryonic development." Cold Spring Harb Protoc **2011**(10): 1235-1243.
- Kermen, F., L. M. Franco, C. Wyatt and E. Yaksi (2013). "Neural circuits mediating olfactory-driven behavior in fish." Front Neural Circuits **7**: 62.
- Kerr, J. N. and W. Denk (2008). "Imaging in vivo: watching the brain in action." Nat Rev Neurosci **9**(3): 195-205.
- Kim, J. S., M. J. Greene, A. Zlateski, K. Lee, M. Richardson, S. C. Turaga, M. Purcaro, M. Balkam, A. Robinson, B. F. Behabadi, M. Campos, W. Denk, H. S. Seung and EyeWirers (2014). "Space-time wiring specificity supports direction selectivity in the retina." Nature **509**(7500): 331-336.
- Kinkhabwala, A., M. Riley, M. Koyama, J. Monen, C. Satou, Y. Kimura, S. Higashijima and J. Fetcho (2011). "A structural and functional ground plan for neurons in the hindbrain of zebrafish." Proc Natl Acad Sci U S A **108**(3): 1164-1169.
- Kiyokage, E., Y. Z. Pan, Z. Shao, K. Kobayashi, G. Szabo, Y. Yanagawa, K. Obata, H. Okano, K. Toida, A. C. Puche and M. T. Shipley (2010). "Molecular identity of periglomerular and short axon cells." J. Neurosci. **30**(3): 1185-1196.
- Knopfel, T. (2012). "Genetically encoded optical indicators for the analysis of neuronal circuits." Nat Rev Neurosci **13**(10): 687-700.
- Knott, G., H. Marchman, D. Wall and B. Lich (2008). "Serial section scanning electron microscopy of adult brain tissue using focused ion beam milling." J Neurosci **28**(12): 2959-2964.
- Koch, K., J. McLean, R. Segev, M. A. Freed, M. J. Berry, 2nd, V. Balasubramanian and P. Sterling (2006). "How much the eye tells the brain." Curr Biol **16**(14): 1428-1434.
- Kohonen, T. (1989). Self-organization and associative memory: 3rd edition, Springer-Verlag New York, Inc.
- Korogod, N., C. C. Petersen and G. W. Knott (2015). "Ultrastructural analysis of adult mouse neocortex comparing aldehyde perfusion with cryo fixation." Elife **4**.
- Korsching, S. I., S. Argo, H. Campenhausen, R. W. Friedrich, A. Rummrich and F. Weth (1997). "Olfaction in zebrafish: what does a tiny teleost tell us?" Semin Cell Dev Biol **8**(2): 181-187.
- Laurent, G. (1999). "A systems perspective on early olfactory coding." Science **286**(5440): 723-728.
- Laurent, G. (2002). "Olfactory network dynamics and the coding of multidimensional signals." Nat Rev Neurosci **3**(11): 884-895.

- LeCun, Y., Y. Bengio and G. Hinton (2015). "Deep learning." Nature **521**(7553): 436-444.
- Leutgeb, J. K., S. Leutgeb, M. B. Moser and E. I. Moser (2007). "Pattern separation in the dentate gyrus and CA3 of the hippocampus." Science **315**(5814): 961-966.
- Lewicki, M. S. (2002). "Efficient coding of natural sounds." Nat Neurosci **5**(4): 356-363.
- Li, J., J. A. Mack, M. Souren, E. Yaksi, S. Higashijima, M. Mione, J. R. Fetcho and R. W. Friedrich (2005). "Early development of functional spatial maps in the zebrafish olfactory bulb." J. Neurosci. **25**: 5784-5795.
- Lichtman, J. W. and W. Denk (2011). "The big and the small: challenges of imaging the brain's circuits." Science **334**(6056): 618-623.
- Lichtman, J. W. and J. R. Sanes (2008). "Ome sweet ome: what can the genome tell us about the connectome?" Curr Opin Neurobiol **18**(3): 346-353.
- Lindsay, S. M. and R. G. Vogt (2004). "Behavioral responses of newly hatched zebrafish (*Danio rerio*) to amino acid chemostimulants." Chem Senses **29**(2): 93-100.
- Lipschitz, D. L. and W. C. Michel (2002). "Amino acid odorants stimulate microvillar sensory neurons." Chem Senses **27**(3): 277-286.
- Lowe, D. G. (2004). "Distinctive image features from scale-invariant keypoints." International Journal of Computer Vision **60**(2): 91-110.
- Luo, L., E. M. Callaway and K. Svoboda (2008). "Genetic dissection of neural circuits." Neuron **57**(5): 634-660.
- Mack-Bucher, J. A., J. Li and R. W. Friedrich (2007). "Early functional development of interneurons in the zebrafish olfactory bulb." Eur. J. Neurosci. **25**: 460-470.
- Marr, D. (1969). "A theory of cerebellar cortex." J Physiol **202**(2): 437-470.
- Mathieu, C. (1999). "Beam-gas and signal-gas interactions in the variable pressure scanning electron microscope." Scan Microsc **13**(1): 23-41.
- McHugh, T. J., M. W. Jones, J. J. Quinn, N. Balthasar, R. Coppari, J. K. Elmquist, B. B. Lowell, M. S. Fanselow, M. A. Wilson and S. Tonegawa (2007). "Dentate gyrus NMDA receptors mediate rapid pattern separation in the hippocampal network." Science **317**(5834): 94-99.
- Mikula, S., J. Binding and W. Denk (2012). "Staining and embedding the whole mouse brain for electron microscopy." Nat Methods **9**(12): 1198-1201.
- Mikula, S. and W. Denk (2015). "High-resolution whole-brain staining for electron microscopic circuit reconstruction." Nat Methods **12**(6): 541-546.

- Miyasaka, N., I. Arganda-Carreras, N. Wakisaka, M. Masuda, U. Sumbul, H. S. Seung and Y. Yoshihara (2014). "Olfactory projectome in the zebrafish forebrain revealed by genetic single-neuron labelling." Nat Commun **5**: 3639.
- Miyasaka, N., K. Morimoto, T. Tsubokawa, S. Higashijima, H. Okamoto and Y. Yoshihara (2009). "From the olfactory bulb to higher brain centers: genetic visualization of secondary olfactory pathways in zebrafish." J. Neurosci. **29**(15): 4756-4767.
- Miyasaka, N., A. A. Wanner, J. Li, J. Mack-Bucher, C. Genoud, Y. Yoshihara and R. W. Friedrich (2013). "Functional development of the olfactory system in zebrafish." Mech Dev **130**(6-8): 336-346.
- Morgan, J. L. and J. W. Lichtman (2013). "Why not connectomics?" Nat Methods **10**(6): 494-500.
- Mori, K. and G. M. Shepherd (1994). "Emerging principles of molecular signal processing by mitral/tufted cells in the olfactory bulb." Semin Cell Biol **5**(1): 65-74.
- Niessing, J. and R. W. Friedrich (2010). "Olfactory pattern classification by discrete neuronal network states." Nature **465**(7294): 47-52.
- Niimura, Y. (2009). "Evolutionary dynamics of olfactory receptor genes in chordates: interaction between environments and genomic contents." Hum Genomics **4**(2): 107-118.
- O'Malley, D. M., Y. H. Kao and J. R. Fetcho (1996). "Imaging the functional organization of zebrafish hindbrain segments during escape behaviors." Neuron **17**(6): 1145-1155.
- Oka, Y., L. R. Saraiva and S. I. Korsching (2012). "Crypt neurons express a single V1R-related ora gene." Chem Senses **37**(3): 219-227.
- Olsen, S. R., V. Bhandawat and R. I. Wilson (2010). "Divisive normalization in olfactory population codes." Neuron **66**(2): 287-299.
- Palotto, M., P. V. Watkins, B. Fubara, J. H. Singer and K. L. Briggman (2015). "Extracellular space preservation aids the connectomic analysis of neural circuits." Elife **4**.
- Perin, R., T. K. Berger and H. Markram (2011). "A synaptic organizing principle for cortical neuronal groups." Proc Natl Acad Sci U S A **108**(13): 5419-5424.
- Perkel, J. M. (2014). "Mapping neural connections." Biotechniques **57**(5): 230-236.
- Pinching, A. J. and T. P. Powell (1971). "The neuron types of the glomerular layer of the olfactory bulb." J Cell Sci **9**(2): 305-345.
- Pinching, A. J. and T. P. Powell (1971). "The neuropil of the glomeruli of the olfactory bulb." J. Cell. Sci. **9**(2): 347-377.
- Pologruto, T. A., B. L. Sabatini and K. Svoboda (2003). "ScanImage: flexible software for operating laser scanning microscopes." Biomed Eng Online **2**: 13.

Pomeroy, S. L., A. S. LaMantia and D. Purves (1990). "Postnatal construction of neural circuitry in the mouse olfactory bulb." J Neurosci **10**(6): 1952-1966.

Portugues, R., K. E. Severi, C. Wyart and M. B. Ahrens (2013). "Optogenetics in a transparent animal: circuit function in the larval zebrafish." Curr Opin Neurobiol **23**(1): 119-126.

Robinson, V. N. E. (1975). "The elimination of charging artefacts in the scanning electron microscope." J. Phys. E: Sci. Instrum. **8**: 638-640.

Rolls, E. T. and R. P. Kesner (2006). "A computational theory of hippocampal function, and empirical tests of the theory." Prog Neurobiol **79**(1): 1-48.

Rosselli-Austin, L. and J. Altman (1979). "The postnatal development of the main olfactory bulb of the rat." J. Dev. Physiol. **1**(4): 295-313.

Rupp, B., M. F. Wullimann and H. Reichert (1996). "The zebrafish brain: a neuroanatomical comparison with the goldfish." Anat Embryol (Berl) **194**(2): 187-203.

Saalfeld, S., A. Cardona, V. Hartenstein and P. Tomancak (2009). "CATMAID: collaborative annotation toolkit for massive amounts of image data." Bioinformatics **25**(15): 1984-1986.

Saalfeld, S., A. Cardona, V. Hartenstein and P. Tomancak (2010). "As-rigid-as-possible mosaicking and serial section registration of large ssTEM datasets." Bioinformatics **26**(12): i57-63.

Sato, K. and N. Suzuki (2001). "Whole-cell response characteristics of ciliated and microvillous olfactory receptor neurons to amino acids, pheromone candidates and urine in rainbow trout." Chem Senses **26**(9): 1145-1156.

Sato, Y., N. Miyasaka and Y. Yoshihara (2005). "Mutually exclusive glomerular innervation by two distinct types of olfactory sensory neurons revealed in transgenic zebrafish." J Neurosci **25**(20): 4889-4897.

Sato, Y., N. Miyasaka and Y. Yoshihara (2007). "Hierarchical regulation of odorant receptor gene choice and subsequent axonal projection of olfactory sensory neurons in zebrafish." J Neurosci **27**(7): 1606-1615.

Satou, M. (1990). "Synaptic organization, local neuronal circuitry, and functional segregation of the teleost olfactory bulb." Prog Neurobiol **34**(2): 115-142.

Schmidhuber, J. (2015). "Deep learning in neural networks: an overview." Neural Netw **61**: 85-117.

Scott, E. K. and H. Baier (2009). "The cellular architecture of the larval zebrafish tectum, as revealed by gal4 enhancer trap lines." Front Neural Circuits **3**: 13.

Seung, H. S. (2009). "Reading the book of memory: sparse sampling versus dense mapping of connectomes." Neuron **62**(1): 17-29.

- Sharpee, T., N. C. Rust and W. Bialek (2004). "Analyzing neural responses to natural signals: maximally informative dimensions." Neural Comput **16**(2): 223-250.
- Sharpee, T. O. (2013). "Computational identification of receptive fields." Annu Rev Neurosci **36**: 103-120.
- Shi, P. and J. Zhang (2009). "Extraordinary diversity of chemosensory receptor gene repertoires among vertebrates." Results Probl Cell Differ **47**: 1-23.
- Sommer, C., C. Straehle, K. U and F. A. Hamprecht (2011). Ilastik: Interactive learning and segmentation toolkit. 2011 IEEE International Symposium on Biomedical Imaging: From Nano to Macro.
- Soucy, E. R., D. F. Albeanu, A. L. Fantana, V. N. Murthy and M. Meister (2009). "Precision and diversity in an odor map on the olfactory bulb." Nat Neurosci **12**(2): 210-220.
- Stocker, R. F., M. C. Lienhard, A. Borst and K. F. Fischbach (1990). "Neuronal architecture of the antennal lobe in *Drosophila melanogaster*." Cell Tissue Res **262**(1): 9-34.
- Streisinger, G., C. Walker, N. Dower, D. Knauber and F. Singer (1981). "Production of clones of homozygous diploid zebra fish (*Brachydanio rerio*)." Nature **291**(5813): 293-296.
- Suter, B. A., T. O'Connor, V. Iyer, L. T. Petreanu, B. M. Hooks, T. Kiritani, K. Svoboda and G. M. Shepherd (2010). "Ephys: multipurpose data acquisition software for neuroscience experiments." Front Neural Circuits **4**: 100.
- Tabor, R. and R. W. Friedrich (2008). "Pharmacological analysis of ionotropic glutamate receptor function in neuronal circuits of the zebrafish olfactory bulb." PLoS One **3**(1): e1416.
- Tabor, R., E. Yaksi and R. W. Friedrich (2008). "Multiple functions of GABA A and GABA B receptors during pattern processing in the zebrafish olfactory bulb." Eur J Neurosci **28**(1): 117-127.
- Tabor, R., E. Yaksi, J. M. Weislogel and R. W. Friedrich (2004). "Processing of odor mixtures in the zebrafish olfactory bulb." J Neurosci **24**(29): 6611-6620.
- Takemura, S. Y., A. Bharioke, Z. Lu, A. Nern, S. Vitaladevuni, P. K. Rivlin, W. T. Katz, D. J. Olbris, S. M. Plaza, P. Winston, T. Zhao, J. A. Horne, R. D. Fetter, S. Takemura, K. Blazek, L. A. Chang, O. Ogundeyi, M. A. Saunders, V. Shapiro, C. Sigmund, G. M. Rubin, L. K. Scheffer, I. A. Meinertzhagen and D. B. Chklovskii (2013). "A visual motion detection circuit suggested by *Drosophila* connectomics." Nature **500**(7461): 175-181.
- Tallini, Y. N., M. Ohkura, B. R. Choi, G. Ji, K. Imoto, R. Doran, J. Lee, P. Plan, J. Wilson, H. B. Xin, A. Sanbe, J. Gulick, J. Mathai, J. Robbins, G. Salama, J. Nakai and M. I. Kotlikoff (2006). "Imaging cellular signals in the heart in vivo: Cardiac expression of the high-signal Ca²⁺ indicator GCaMP2." Proc. Natl. Acad. Sci. U. S. A. **103**(12): 4753-4758.
- Taniguchi, K. and K. Taniguchi (2014). "Phylogenetic studies on the olfactory system in vertebrates." J Vet Med Sci **76**(6): 781-788.

- Tapia, J. C., N. Kasthuri, K. J. Hayworth, R. Schalek, J. W. Lichtman, S. J. Smith and J. Buchanan (2012). "High-contrast en bloc staining of neuronal tissue for field emission scanning electron microscopy." Nat Protoc **7**(2): 193-206.
- Titze, B. and W. Denk (2013). "Automated in-chamber specimen coating for serial block-face electron microscopy." J Microsc.
- Treves, A., A. Tashiro, M. P. Witter and E. I. Moser (2008). "What is the mammalian dentate gyrus good for?" Neuroscience **154**(4): 1155-1172.
- Varshney, L. R., B. L. Chen, E. Paniagua, D. H. Hall and D. B. Chklovskii (2011). "Structural properties of the *Caenorhabditis elegans* neuronal network." PLoS Comput Biol **7**(2): e1001066.
- Vitebsky, A., R. Reyes, M. J. Sanderson, W. C. Michel and K. E. Whitlock (2005). "Isolation and characterization of the laque olfactory behavioral mutant in the zebrafish, *Danio rerio*." Dev Dyn **234**(1): 229-242.
- Wachowiak, M. and M. T. Shipley (2006). "Coding and synaptic processing of sensory information in the glomerular layer of the olfactory bulb." Semin Cell Dev Biol **17**(4): 411-423.
- Walton, J. (1979). "Lead aspartate, an en bloc contrast stain particularly useful for ultrastructural enzymology." J Histochem Cytochem **27**(10): 1337-1342.
- Wang, W. P., B. Juttler, D. Y. Zheng and Y. Liu (2008). "Computation of rotation minimizing frames." Acm Transactions on Graphics **27**(1).
- Wanner, A. A., C. Genoud, T. Masudi, L. Siksou and R. W. Friedrich (2016). "Dense EM-based reconstruction of the interglomerular projectome in the zebrafish olfactory bulb." Nat Neurosci **19**(6): 816-825.
- Wanner, A. A., M. A. Kirschmann and C. Genoud (2015). "Challenges of microtome-based serial block-face scanning electron microscopy in neuroscience." J Microsc **259**(2): 137-142.
- Westerfield, M. (2000). The zebrafish book. A guide for the laboratory use of zebrafish (*Danio rerio*). Eugene, OR, University of Oregon Press.
- White, J. G., E. Southgate, J. N. Thomson and S. Brenner (1986). "The structure of the nervous system of the nematode *Caenorhabditis elegans*." Philos. Trans. R. Soc. Lond. B Biol. Sci. **314**: 1-340.
- White, R. M., A. Sessa, C. Burke, T. Bowman, J. LeBlanc, C. Ceol, C. Bourque, M. Dovey, W. Goessling, C. E. Burns and L. I. Zon (2008). "Transparent adult zebrafish as a tool for in vivo transplantation analysis." Cell Stem Cell **2**(2): 183-189.
- Wiechert, M. T., B. Judkewitz, H. Riecke and R. W. Friedrich (2010). "Mechanisms of pattern decorrelation by recurrent neuronal circuits." Nature Neurosci. **13**(8): 1003-1010.

Willhite, D. C., K. T. Nguyen, A. V. Masurkar, C. A. Greer, G. M. Shepherd and W. R. Chen (2006). "Viral tracing identifies distributed columnar organization in the olfactory bulb." Proc Natl Acad Sci U S A **103**(33): 12592-12597.

Wilson, D. A. and R. M. Sullivan (2011). "Cortical processing of odor objects." Neuron **72**(4): 506-519.

Wilson, R. I. and Z. F. Mainen (2006). "Early events in olfactory processing." Annu Rev Neurosci **29**: 163-201.

Yaksi, E. and R. W. Friedrich (2006). "Reconstruction of firing rate changes across neuronal populations by temporally deconvolved Ca²⁺ imaging." Nat Methods **3**(5): 377-383.

Yaksi, E., B. Judkewitz and R. W. Friedrich (2007). "Topological reorganization of odor representations in the olfactory bulb." PLoS Biol. **5**(7): e178.

Yang, W., J. E. Miller, L. Carrillo-Reid, E. Pnevmatikakis, L. Paninski, R. Yuste and D. S. Peterka (2016). "Simultaneous Multi-plane Imaging of Neural Circuits." Neuron **89**(2): 269-284.

Yokoi, M., K. Mori and S. Nakanishi (1995). "Refinement of odor molecule tuning by dendrodendritic synaptic inhibition in the olfactory bulb." Proc Natl Acad Sci U S A **92**(8): 3371-3375.

Yoshihara, Y. (2009). "Molecular genetic dissection of the zebrafish olfactory system." Results Probl Cell Differ **47**: 97-120.

Zhu, P., O. Fajardo, J. Shum, Y.-P. Zhang Schärer and R. W. Friedrich (2012). "High-resolution optical control of spatiotemporal neuronal activity patterns in zebrafish using a digital micromirror device." Nat. Protoc. **7**(7): 1410-1425.

Zhu, P., T. Frank and R. W. Friedrich (2013). "Equalization of odor representations by a network of electrically coupled inhibitory interneurons." Nature Neurosci. **16**(11): 1678-1686.

Appendix A Nature Neuroscience article on *Dense EM-based reconstruction of the interglomerular projectome in the zebrafish olfactory bulb*

Contribution:

Adrian A. Wanner developed EE embedding, CORE, PyKNOSSOS and analysis procedures. He acquired images from the larval OB, founded ariadne-service gmbh, supervised tracers, reconstructed all neurons, annotated synapses, analyzed the data, and participated in the acquisition of the stack of the adult olfactory bulb and in writing the manuscript.

Please contact Adrian A. Wanner (adrian.wanner@ariadne-service.com) for a pdf-Version of this paper.

Appendix B PyKNOSSOS manual

Appendix C Review article on *Challenges of microtome-based serial
block-face scanning electron microscopy in neuroscience*

Contribution:

Adrian A. Wanner contributed Figure 2 and wrote the review with participation of Moritz Kirschmann and Christel Genoud.

Please contact Adrian A. Wanner (adrian.wanner@ariadne-service.com) for a pdf-Version of this paper.

Appendix D Review article on *Analyzing the structure and function of neuronal circuits in zebrafish*

Contribution:

Adrian A. Wanner participated in writing the review and contributed Figure 1.

Please contact Adrian A. Wanner (adrian.wanner@ariadne-service.com) for a pdf-Version of this paper.

Appendix E Review article on *Functional development of the olfactory system in zebrafish*

Contribution:

Adrian A. Wanner participated in writing the review and contributed Figure 4.

Please contact Adrian A. Wanner (adrian.wanner@ariadne-service.com) for a pdf-Version of this paper.

Appendix F Curriculum vitae

Adrian A. Wanner
Birchstrasse 72
CH-8057 Zürich
(+41) 79 795 50 32
adrian.wanner@ariadne-service.com

EDUCATION

Nov 2009 – March 2016, international PhD program in the group of Prof. Rainer Friedrich at the Friedrich Miescher Institute for Biomedical Research and University of Basel, Switzerland. GPA: 6/6, summa cum laude

Apr. 2009 – Nov 2009, visiting scientist in the group of Prof. Richard Hahnloser at the Institute of Neuroinformatics, ETH and University of Zurich, Switzerland

Sept 2008 – Feb 2009, master thesis in the group of Prof. Tatyana Sharpee at the Salk Institute for Biological Studies in La Jolla, USA. GPA: 6/6, summa cum laude

June 2008 – Aug 2008, research project in the group of Prof. Kurt Wüthrich at the Institute of Molecular Biology and Biophysics, ETH Zurich, Switzerland

Sept 2003 – Feb 2009, Master in Interdisciplinary Sciences (Dipl. Natw. ETHZ), ETH Zurich, Switzerland. GPA 5.45/6

1997 – 2003, High School, focus in Natural Sciences, Lucerne, Switzerland

PUBLICATIONS

Wanner, A. A., C. Genoud, T. Masudi, L. Siksou and R. W. Friedrich (2016). Dense EM-based reconstruction of the interglomerular projectome in the zebrafish olfactory bulb. *Nat Neurosci* 19(6): 816-825

Wanner A. A., Kirschmann M.A., Genoud C. (2015). Challenges of microtome-based serial block-face scanning electron microscopy in neuroscience. *Journal of Microscopy*, 259: 137–142

Friedrich R.W., Genoud C., Wanner A.A. (2013). Analyzing the structure and function of neuronal circuits in zebrafish. *Front Neural Circuits*. 2013 Apr 23; 7:71

Miyasaka N., Wanner A.A., Li J., Mack-Bucher J., Genoud C., Yoshihara Y., Friedrich R.W. (2012). Functional development of the olfactory system in zebrafish. *Mech Dev*. 2013 Jun-Aug; 130(6-8):336-46

PATENTS

Wanner A.A., Genoud C., Friedrich R.W. (2014). Electrically conductive sample blocks for scanning electron microscopy. Application no PCT/IB2014/062157, filed June 2014. European patent application EP14736451 and US patent application US14897514

NON-ACADEMIC POSITIONS

Nov 2014 – current: CEO and founder of ariadne-service gmbh, a high-throughput image annotation service for biomedical data with >30 professional annotators. Webpage: www.ariadne-service.com

AWARDS/ GRANTS/ SCHOLARSHIPS

Jan 2015, Volker Henn Best Poster Award 2015, Annual meeting Swiss Society for Neuroscience

Oct 2012, Travel grant for prospective young researchers from the University of Basel for the SfN 2012 conference in New Orleans, USA

Nov 2009 – March 2016, FMI international PhD program, Friedrich Miescher Institute for Biomedical Research, Basel, Switzerland

Sept 2008 – Feb 2009, Albert Barth-Fund ETH Zurich, Switzerland. Travel grant supporting the master thesis at the Salk Institute for Biological Studies, USA

TEACHING/ COMMITTEES

2014, organizer of the CNIB lecture series Introduction to Computational Neuroscience II

2013, organizer of the CNIB lecture series Introduction to Computational Neuroscience I

Aug 2013, organizer of the 1st Swiss Computational Neuroscience Summer School

June – July 2013, lecturer for Introduction to Linear Algebra for Neuroscience, FMI Basel

May 2013, founder of the Computational Neuroscience Initiative Basel (CNIB)

CONFERENCE CONTRIBUTIONS:

Jan 2015, poster at the Swiss Neuroscience Meeting, Bern, Switzerland

Sept 2014, talk at the Annual Meeting of the Friedrich Miescher Institute, Arosa, Switzerland

Sept 2014, talk and poster at the Max Planck/ HHMI Connectomics Conference in Berlin, Germany

July 2014, poster at the 9th Federation of European Neuroscience Societies Meeting in Milan, Italy

April 2014, talk at the Joint Retreat FMI (Basel) and CNC (Trondheim) in Rungstedgaard, Denmark

Mar 2014, talk at the Neural Skircuit Reconstruction Meeting, Andermatt, Switzerland

Jan 2014, poster at the Swiss Neuroscience Meeting, Bern, Switzerland

Sept 2013, poster at the Ascona Meeting on Neuronal Circuits, Ascona, Switzerland

May 2013, talk at the Giessbach Neuroscience Meeting on Cellular and Molecular Neurobiology of Mental Diseases, Giessbach, Switzerland

Feb 2013, poster at the Swiss Neuroscience Meeting, Geneva, Switzerland

Oct 2012, poster at the Society for Neuroscience (SfN) conference, New Orleans, USA

Mar 2012, talk at the Interdisciplinary Symposium on 3D microscopy 2012, Les Diablerets, Switzerland

Nov 2011, poster at the Society for Neuroscience (SfN) conference, Washington DC, USA

Sept 2011, poster at the Janelia Farm Conference on High Resolution Circuit Reconstruction, Virginia, USA

Mar 2011, poster at the Swiss Neuroscience Meeting, Basel, Switzerland

Dec 2010, poster at the European Symposium on Imaging Structure and Function in the Zebrafish Brain, Lisbon, Portugal

PERSONAL

Born December 14th 1983 in Buchrain, Switzerland

Languages: German (native), English and French

Programming skills: MATLAB, Python, C++, C

Hobbies: Hiking, swimming, snowboarding, skiing & ski touring, playing classical music (oboe, clarinet), literature, reading & writing

REFERENCES

Dr. Rainer Friedrich, Friedrich Miescher Institute for Biomedical Research, Basel, Switzerland

Email: rainer.friedrich@fmi.ch

Dr. Richard Hahnloser, Institute of Neuroinformatics, ETH and University of Zurich, Switzerland

Email: rich@ini.phys.ethz.ch

Dr. Tatyana Sharpee, Salk Institute for Biological Studies, La Jolla, USA

Email: sharpee@salk.edu